

**Editor-in-Chief B.E.Paton**

**Editorial board:**

Yu. S. Borisov	V. F. Grabin
A. Ya. Ishchenko	V. F. Khorunov
B. V. Khitrovskaya	I. V. Krivtsun
S. I. Kuchuk-Yatsenko	
Yu. N. Lankin	V. K. Lebedev
V. N. Lipodaev	L. M. Lobanov
V. I. Makhnenko	A. A. Mazur
O. K. Nazarenko	I. K. Pokhodnya
I. A. Ryabtsev	Yu. A. Sterenbogen
N. M. Voropai	K. A. Yushchenko
A. T. Zelnichenko	

**International editorial council:**

N. P. Alyoshin	(Russia)
U. Diltey	(Germany)
Guan Qiao	(China)
D. von Hofe	(Germany)
V. I. Lysak	(Russia)
N. I. Nikiforov	(Russia)
B. E. Paton	(Ukraine)
Ya. Pilarczyk	(Poland)
P. Seyffarth	(Germany)
G. A. Turichin	(Russia)
Zhang Yanmin	(China)
A. S. Zubchenko	(Russia)

**Promotion group:**

V. N. Lipodaev, V. I. Lokteva  
A. T. Zelnichenko (exec. director)

**Translators:**

I. N. Kutianova, V. F. Orets,  
T. K. Vasilenko, N. V. Yalanskaya

**Editor**

N. A. Dmitrieva

**Electron galley:**

I. S. Dmitruk, T. Yu. Snegiryova

**Address:**

E.O. Paton Electric Welding Institute,  
International Association «Welding»,  
11, Bozhenko str., 03680, Kyiv, Ukraine  
Tel.: (38044) 287 67 57  
Fax: (38044) 528 04 86  
E-mail: journal@paton.kiev.ua  
http://www.nas.gov.ua/pwj

State Registration Certificate  
KV 4790 of 09.01.2001

**Subscriptions:**

**\$324**, 12 issues per year,  
postage and packaging included.  
Back issues available.

All rights reserved.

This publication and each of the articles  
contained herein are protected by copyright.  
Permission to reproduce material contained in  
this journal must be obtained in writing from  
the Publisher.

Copies of individual articles may be obtained  
from the Publisher.

**CONTENTS**

SCIENTIFIC AND TECHNICAL

*Knysh V.V., Valteris I.I., Kuzmenko A.Z. and Solovej S.A.*  
Corrosion fatigue resistance of welded joints strengthened  
by high-frequency mechanical peening ..... 2

*Pekarska V.* Numerical simulation of metal structure in  
HAZ in welding of increased strength steel ..... 5

*Borisov Yu.S., Borisova A.L., Tunik A.Yu., Karpets M.V.,  
Vojnarovich S.G., Kisliitsa A.N. and Kuzmich-Yanchuk E.K.*  
Effect of microplasma spraying parameters on structure,  
phase composition and texture of hydroxyapatite coatings ..... 10

*Milenin A.S.* Physical and technological aspects of  
braze-welding of titanium-aluminium joints (Review) ..... 16

*Silchenko T.Sh., Kuzmin S.V., Lysak V.I., Gorobtsov A.S.  
and Dolgy Yu.G.* Estimation of vertical displacement of  
flyer metal plates before contact point in explosion  
welding ..... 20

INDUSTRIAL

*Makhnenko V.I., Zhudra A.P., Velikoivanenko E.A., Bely A.I.  
and Dzykovich V.I.* Prediction of the size of granules and  
efficiency of their production in centrifugal spraying of  
alloys ..... 24

*Yavorsky Yu.D., Kuchuk-Yatsenko S.I. and Losev L.N.*  
Experimental estimation of carrying capacity of butt  
welded joints of structural shapes in elements of  
structures subjected to low-cycle load ..... 32

*Kononenko V.Ya.* Hyperbaric dry underwater welding  
(Review) ..... 36

BRIEF INFORMATION

*Kolyada V.A. and Shapovalov E.V.* Calibration of an optical  
system for evaluation of temperature field distribution in  
the welding zone ..... 41

News ..... 44

Developed at PWI ..... 15, 23, 46, 47



# CORROSION FATIGUE RESISTANCE OF WELDED JOINTS STRENGTHENED BY HIGH-FREQUENCY MECHANICAL PEENING

V.V. KNYSH, I.I. VALTERIS, A.Z. KUZMENKO and S.A. SOLOVEJ

E.O. Paton Electric Welding Institute, NASU, Kiev, Ukraine

The paper gives the results of investigation of the influence of corrosive environment on lowering of fatigue resistance of tee welded joints on 10KhSND steel unstrengthened and strengthened by high-frequency mechanical peening (HFMP). The high effectiveness of application of HFMP technology as a method of surface plastic deformation of metal near the areas of fatigue damage localization to improve corrosion fatigue was established experimentally. Application of HFMP technology improves the cyclic fatigue life of tee welded joints in a corrosive environment 3.5 times and endurance limit by 80 %.

*Keywords:* arc welding, metal structures, welded joints, corrosive environment, cyclic load, high-frequency mechanical peening, fatigue life improvement

Corrosion is the most widely spread type of welded joint damage in such metal structures as bridges, off-shore platforms, ship hulls, etc. [1, 2]. On the other hand, these structures are operating under the conditions of the impact of alternating loads, so that corrosion fatigue is the main mechanism of their damage in service. Simultaneous influence under the alternating loading conditions of such damaging factors as corrosive environment, high levels of stress concentration and tensile residual welding stresses in the joint local zones [1] leads to the corrosion-fatigue damage mechanism being the most hazardous and essentially increasing the fracture rate of welded structure elements.

To ensure the required fatigue life of the joints operating under the corrosion fatigue conditions, additional postweld heat treatments [3–5] are usually applied, which are aimed at redistribution of the tensile residual stresses, lowering of the stress concentration factor, inducing favourable residual compressive stresses, elimination of surface microcracks in the weld zones.

However, the experimental data given in [3, 4] do not provide an unambiguous answer about the effectiveness of the proposed treatments. In [3] it is experimentally established that metal strengthening by explosion in the geometrical stress raiser locations has only a minor influence on the cyclic fatigue life of welded samples in sea water. On the other hand, the authors of [3] using fatigue testing in air, which confirms the high effectiveness of explosion treatment and coefficient of lowering of cyclic fatigue life in sea water 1.6–1.8 times, present this treatment as a quite promising technology of improvement of the operating reliability of hydraulic engineering facilities. In [4] low-frequency vibration treatment is used to lower the residual stresses in order to improve the corrosion fatigue resistance of welded structures. The major drawback of this technology is also indicated as a

simultaneous lowering of cyclic fatigue life of the structure, having internal defects, which were overlooked during inspection. In [5] at fatigue testing of tee welded joints in sea water it is shown that at shot blasting surface strengthening the corrosion-fatigue life of the joint is increased 2–3 times in the stress raiser zones. Fatigue cracks in the samples both in the initial condition, and after strengthening initiated in the zone of the deposited metal transition to the base metal. Values of improvements of corrosion-fatigue life of the joints established in [5], point to the high effectiveness of application of the methods of surface plastic deformation of the joint metal near the sites of fatigue damage localization for improvement of the metal structure service life.

During the recent years, the technology of high-frequency mechanical peening (HFMP) of the welded joint metal in the stress raiser zones, using the energy of ultrasound, has become widely applied for improvement of cyclic fatigue life of welded elements [6–8]. It is anticipated that the ultrasonic HFMP technology will turn out to be the most effective for improvement of welded joint corrosion fatigue resistance, compared to other known methods of surface plastic deformation of the metal (explosion treatment, pneumatic peening, roller treatment, shot peening, etc.). This assumption is based on the fact that application of ultrasonic HFMP technology for strengthening the zone of fillet weld transition to base metal in tee joints on St.3sp (killed) steel to the depth down to 10–20  $\mu\text{m}$  results in formation of grains elongated in one direction in the treatment zone, their lateral dimension being 100 nm and less. Electron diffraction accentuates the crystalline nature of the structure [9]. Therefore, a metal nanostructure forms at down to 20  $\mu\text{m}$  depth in the zone of peening by ultrasonic HFMP technology, which may have an essential influence on improvement of the corrosion fatigue resistance of strengthened joints.

In this work the influence of the corrosive environment on lowering of fatigue resistance of welded joints with fillet welds strengthened and unstrengthened by HFMP technology was studied.

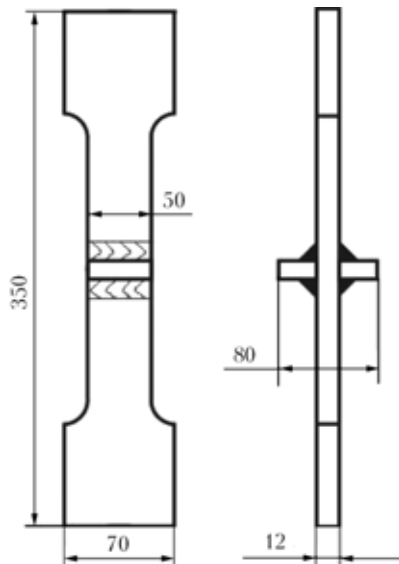


**Figure 1.** Schematic of a sample of tee joint on 10KhSND steel

The influence of the corrosive environment was evaluated on samples of tee joints of 10KhSND steel ( $\sigma_y = 390$  MPa,  $\sigma_t = 530$  MPa) (Figure 1). Prismatic samples from this steel of  $370 \times 70 \times 12$  mm size were cut out of rolled sheets so that the long side was oriented along the rolling direction. Transverse stiffeners were welded by fillet welds from two sides by manual arc welding. At strengthening of the joints by HFMP technology a narrow zone of weld metal transition to the base metal was subjected to surface plastic deformation. Fatigue testing of four sample series was conducted in URS 20 testing machine at uniaxial alternating loading with cycle asymmetry  $R_\sigma = 0$ . Samples of the first and second series were tested in as-welded condition in air and in the corrosive environment, respectively, samples of the third and fourth series were treated by HFMP and were also tested in air and in the corrosive environment. All samples were tested to complete fracture.

A 3 % NaCl solution was used as the corrosive environment, which was poured into a tank specially provided on the head for sample clamping. The tank was a plastic bath of 4 l volume. The appearance of the bath tank fastened to the sample during testing



**Figure 2.** Sample of a tee welded joint on 10KhSND steel during testing in the corrosive environment

is shown in Figure 2. This set-up provided a constant immersion of all four joints with fillet welds and HAZ in the corrosive environment during load application. Length of the middle part of the sample immersed into NaCl solution was 120 mm. This structure was mounted on the sample in an unloaded state through a special hole in the device bottom. Further on the gap between the sample surface and bath was sealed by a composite fluoroplastic gasket of a special design and was filled with glue, thus preventing mechanical damage in the samples or leakage of the corrosive solution. After testing of each sample the corrosive solution was replenished.

Nature of fatigue fracture of joints untreated and strengthened by HFMT technology turned out to be different. In untreated joints the crack initiated in the points of transition of the weld to the base metal in the zone of maximum tensile stresses (in the sample center) (Figure 3, a). In the corrosive environment in the joints strengthened by HFMP technology the cracks initiated at a distance from the fusion zone at the edges of the sample test part (Figure 3, b and

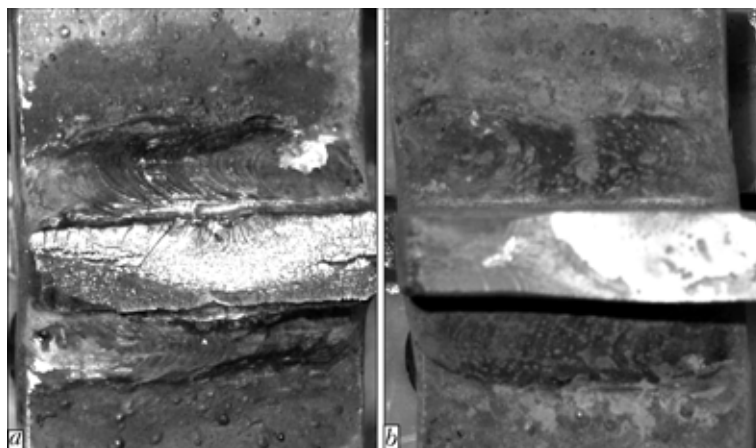


**Figure 3.** Fatigue fractures of unstrengthened (a) and strengthened (b) samples of a tee welded joint on 10KhSND steel tested in the corrosive environment

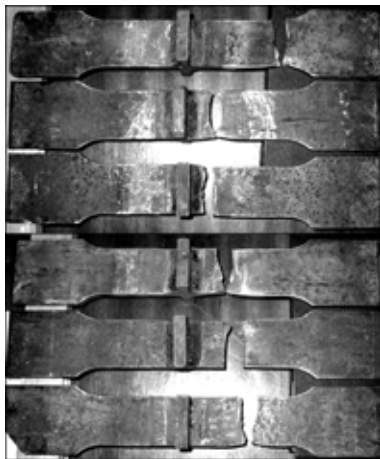


**Figure 4.** General view of strengthened samples of a tee welded joint on 10KhSND steel fractured after fatigue testing in corrosive environment

Figure 4). Similar nature of fracture was observed also in the strengthened samples tested in air.

Results of fatigue testing of all the four sample series are given in Figure 5. It follows from fatigue curves 1 and 3 that application of ultrasonic HFMP technology as a method of surface plastic deformation of the joint metal near the sites of fatigue damage localization improves the corrosion fatigue life 3.5 times. The corrosion fatigue life of the strengthened joints increases 2.5 times compared to unstrengthened joints, tested in air (curves 2 and 4). Endurance limit of strengthened joints corresponding to the base of  $2 \cdot 10^6$  cycles in a corrosive environment, rises by 80 % compared to unstrengthened joints. This may be caused by the fact that the compressive stresses induced in the surface layer at strengthening not only extend the stage of fatigue crack initiation, but also promote closing of the initiating microscopic cracks and pressing of the corrosive solution out of them. The latter lowers the cyclic fatigue life of the strengthened joints 2–4 times depending on the level of the applied stress, and the endurance limit on the base of  $2 \cdot 10^6$  cycles — by 30 % (curves 3 and 4). Cyclic fatigue life of the samples in as-welded condition, tested in a corrosive environment, decreases 1.4 times, and the endurance limit by 15 % (curves 1 and 2). Such a difference between the unstrengthened and strengthened joints, tested in air and in the corrosive environment, is attributable to the fact that all the strengthened samples failed at a distance from the fusion zone across the base metal. In this case, the experimental data (curves 3, 4 in Figure 5) actually are the fatigue curves of the base metal (10KhSND steel) in air and in the corrosive environment.

Thus, the experimentally established fatigue curves of the joints confirm the high effectiveness of application of surface strengthening by ultrasonic HFMP technology of the stress concentrator zones to improve the corrosion fatigue of tee welded joints.

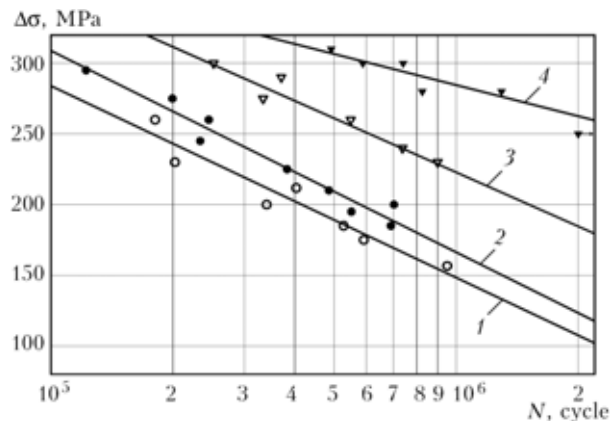


**Figure 5.** Fatigue curves of tee welded joints on low-alloyed 10KhSND steel: 1, 2 — in the initial as-welded condition in the corrosive environment and in air, respectively; 3, 4 — after strengthening by HFMP technology in the corrosive environment and in air, respectively

## CONCLUSIONS

1. Ultrasonic HFMP technology improves the fatigue resistance of tee welded joints on 10KhSND steel to the level of base metal both in air, and in the corrosive environment.

2. Cyclic fatigue life of samples of tee joints on 10KhSND steel in the as-welded condition, tested in the corrosive environment, decreases 1.4 times, and the endurance limit on the base of  $2 \cdot 10^6$  cycles — by 15 %, irrespective of the level of applied stresses.

3. Application of ultrasonic HFMP technologies as a method of surface plastic deformation of the metal near the sites of fatigue damage localizing improves the cyclic fatigue life of tee welded joints on 10KhSND steel in the corrosive environment 3.5 times.

4. Corrosive environment lowers the endurance limit of tee joints on 10KhSND steel strengthened by ultrasonic HFMP technology on the base of  $2 \cdot 10^6$  cycles from 260 to 185 MPa. This, however, is by 80 % higher than the fatigue limit of the joints in as-welded condition tested in the corrosive environment ( $10^5$  MPa).

- (1979) *Welding in machine-building*. Refer. Book. Ed. by V.A. Vinokurov. Vol. 3. Moscow: Mashinostroenie.
- Kovtunenkov, V.A., Sineok, A.G., Gerasimenko, A.M. et al. (2005) Typical damages of welded metal structures of bridges. *The Paton Welding J.*, **10**, 27–32.
- Titov, V.A., Petushkov, V.G. (2001) Influence of explosion treatment on corrosion-mechanical strength of welded joints. *Ibid.*, **2**, 50–52.
- Zimnitsky, Yu.A., Khvalynsky, V.N. (2004) Experimental validation of effect of low-frequency vibrotreatment on service life of hull structures. *Sudostroenie*, **1**, 50–52.
- Gorbach, V.D., Mikhajlov, V.S. (2000) Surface hardening of welded joints for increase in the corrosion-fatigue life of ship structures. *Ibid.*, **4**, 45–48.
- Lobanov, L.M., Mikheev, P.P., Knysh, V.V. et al. *Method of treatment of metal structure welded joints by high-frequency peening*. Pat. 60390 Ukraine. Publ. 15.10.2003.
- Lobanov, L.M., Kirian, V.I., Knysh, V.V. et al. (2006) Improvement of fatigue resistance of welded joints in metal structures by high-frequency mechanical peening (Review). *The Paton Welding J.*, **9**, 2–8.
- Lobanov, L.M., Kirian, V.I., Knysh, V.V. (2006) Increase in service life of welded metal structures by high-frequency mechanical peening. *Fiz.-Khim. Mekhanika Materialiv*, **1**, 56–61.
- Prokopenko, G.I., Knysh, V.V., Kuzmenko, A.Z. et al. (2005) Structure of welded joint transition zone of ordinary carbon steel after high-frequency mechanical peening. In: *Abstr. of Int. Sci.-Techn. Conf. on Dynamics, Strength and Service Life of Machines and Structures (Kiev)*, Vol. 2, 288–289.



# NUMERICAL SIMULATION OF METAL STRUCTURE IN HAZ IN WELDING OF INCREASED STRENGTH STEEL

V. PEKARSKA

Politechnika Czestochowska, Poland

A mathematical model is proposed, which describes the temperature field and phase transformations in laser welding. The temperature field is determined by the equation of an unsteady heat flow with a convection term using Green's function. Model of the phase transformations in solid state for the steel being welded is based on assumption of continuous cooling and Avrami, Koistinen and Marburger equations. Volume fractions of phases during cooling are defined as functions of the cooling temperature and rate, and deformation increment depends upon the temperature and phase transformations. Metal structure in the welded joint HAZ was evaluated.

*Keywords: laser welding, temperature field, heat-affected zone, thermal cycle, dilatograms, phase transformations, structure, mathematical model*

High working load and fatigue strength requirements are established for welded structures. Mechanical characteristics of the HAZ metal are especially affected by temperature fields and phase transformations in welding, which cause significant isotropic heat and structural strains that generate significant temporary and residual stresses [1–7]. So, when simulating a welding process it is necessary to take into account not just temperature changes, but also phase transformations and kinetics thereof [1, 3–11]. Numeric investigations of phase transformations allow reducing volume of labor-consuming experiments and obtaining data for calculation of residual stresses.

Kinetics of the microstructural changes in a weld and a near-weld zone in welding of steels represents a complex process, which is adequately difficult for mathematical description. For estimating influence of phase transformations on strains and stresses, which occur during heating and cooling of the metal, the data are necessary on kinetics and types of phase transformations.

Scientists have been investigating phase transformations since long. The literature, devoted to this topic, contains descriptions of the models, which take into account role of the processes occurring in heat treatment [4, 5, 12–17], whereby attention of the researchers is attracted to the kinetics of phase transformations and possibility of quantitative prediction of a welded joint structure depending upon parameters of the welding [1, 9–11]. It is determined that it is rather realistic to build mathematical models on basis of diagrams of anisothermal decomposition of austenite (ADA). For predicting content of structural components and mechanical properties of the HAZ metal depending upon chemical composition of steel and rate of cooling  $w_{8/5}$  within temperature range 800–500 °C the models are in particular used developed for low alloyed steels of increased strength [18].

In recent decade great attention is paid to laser welding, and requirements to quality of welded joints get permanently more stringent. However, still few models of development of the processes, which accompany welding, exist. For example, in a number of works optimal parameters of welding are experimentally determined, a temperature field is simulated, results of metallographic investigations of the metal structure in the welding zone, etc. are presented [4, 10, 16, 19, 20].

In laser welding the phenomena occur, which are not characteristic of traditional methods of welding [3, 4, 10, 11, 16, 19, 20]. Power of the beam and speed of its movement exert great influence on shape of the bead and, therefore, dimensions of HAZ of the elements being welded [10, 11, 16, 19]. A concentrated source of heat in laser welding heats the metal being joined up to high temperature with significant gradient of the latter. Because of high rate of the metal cooling in laser welding hardened structures form in HAZ, which occur even in steels with good weldability.

In order to increase knowledge in the field of simulation of phase transformations, which occur in the HAZ metal, the suggested mathematical model of phase transformations of the S355J2G3 steel of increased strength is considered in this work, and with its assistance numeric simulation of the HAZ metal structure is made in laser welding of a sheet. Model of phase transformations in solid state of steel is built on basis of ADA and Avrami, Koistinen and Marburger equations. Values of elongation, strain and volume share of phases, depending upon phase transformations of the investigated steel, are assumed proceeding from the experimental data. Temperature field of a welded joint is determined from the equation of unsteady heat flow with a convective term, which is solved by the method of Green's function [20]. When assessing structural components in HAZ, volume shares of phases during heating and cooling were determined as functions of temperature and rate of cooling.

## **Mathematical model of phase transformations.**

The phase transformation model is developed for a welded steel of increased strength with application of



the ADA diagram, and volume share of phases during cooling is determined as function of temperature and rate of cooling.

Volume share of austenite, formed during heating, is determined by Avrami formula:

$$\eta_A(T, t) = 1 - \exp(-bt^n), \quad (1)$$

where  $t$  is the time;  $b(t_s, t_f)$  and  $n(t_s, t_f)$  are the coefficients, determined from conditions of beginning ( $\eta_s = 0.01$ ) and finishing ( $\eta_f = 0.99$ ) of the phase transformations;  $t_s$  and  $t_f$  are the time of respectively beginning and finishing of the phase transformations;

$$n(t_s, t_f) = \frac{\ln(\ln(\eta_s)/\ln(\eta_f))}{\ln(t_s/t_f)}, \quad b(t_s, t_f) = -\frac{\ln(\eta_f)}{(t_s)^n}. \quad (2)$$

Volume share of the phase, formed during cooling of austenite, is determined by temperature and rate of cooling  $w_{8/5}$ . Volume share of a new phase (ferrite, pearlite, or bainite) is found taking into account cooling rate also by Avrami equation (diffusion transformations), taking into account already existing structural components:

$$\eta_{(c)}(T, t) = \eta_{(c)}\eta_A(1 - \exp(-b(t(T))^n)); \quad \sum_k \eta_k = 1, \quad (3)$$

where  $\eta_{(c)}$  is the maximal volume share of the phase at a certain cooling rate, %;  $\eta_k$  is the volume share of a respective phase of initial structure (without transition into austenite), %.

Coefficients  $n$  and  $b$  are determined by formulas (2), where  $t_s$  and  $t_f$  depend upon rate of cooling  $w_{8/5}$ , i.e.  $b = b(t_s(w_{8/5}))$ ,  $t_f(t_s(w_{8/5}))$ , and  $n = n(t_s(w_{8/5}))$ ,  $t_f(w_{8/5})$ .

Volume share of martensite is found by the modified Koistinen–Marburger formula:

$$\eta_M(T) = \eta_{(c)}\eta_A \left( 1 - \exp \left( - \left( \frac{M_s - T}{M_s - M_f} \right)^m \right) \right), \quad (4)$$

$$T \in [M_s, M_f(w_{8/5})],$$

where  $m = 2.5$  is the coefficient, experimentally determined for the steel being investigated;  $M_s$ ,  $M_f$  are the temperatures of respectively beginning and finishing of the martensite transformation.

Phase transformations cause isotropic deformation of metal, whereby increment of strain depending upon temperature and phase transformations during heating and cooling, is determined by formulas

$$d\epsilon^{TPh} = \sum_{i=1}^{i=5} \alpha_i \eta_i dT - \epsilon_A^{Ph} dV_A, \quad (5)$$

$$d\epsilon^{TPh} = \sum_{i=1}^{i=5} \alpha_i \eta_i dT + \sum_{i=2}^{i=5} \epsilon_j^{Ph} d\eta_j,$$

where  $\alpha_i = \alpha_i(T)$  are the coefficients of linear dilatation;  $i = A, B, F, M, P$  are respectively austenite, bainite, ferrite, martensite and pearlite;  $\epsilon_A^{Ph}$  is the isotropic deformation of phase transformation of the initial structure into austenite;  $\epsilon_j^{Ph} = \epsilon_j^{Ph}(T)$  are the isotropic deformations of phase transformation of austenite respectively into  $j = B, F, M, P$ .

**Check of the model.** For kinetics description of the phase transformations and stipulated by them values of deformations, dilatometric investigations on the LVDT dilatometer of the Thermoanalyse GmbH were carried out. The experiments were carried out on the S355J2G3 welded steel of the following composition, wt. %: 0.19 C; 1.05 Mn; 0.2 Si; 0.028 P; 0.02 S; 0.08 Cr; 0.11 Ni; 0.006 Al; 0.003 V.

Heating of tubular specimens of 10 mm length up to 1100 °C was performed at a rate 100 °C/s, cooling was carried out at different rates (630, 300, 200, 150, 100, 50, 10, 2 and 0.5 °C/s), and time of soaking was 2 s. Critical points of transformation  $A_{c1}$  and  $A_{c3}$ , experimentally determined at heating rate 100 °C/s, equaled respectively 758 and  $(911 \pm 4)$  °C ( $A_{c1} \approx 740$  and  $A_{c3} \approx 860$  °C).

For determining structural composition of the material at different rates of cooling dilatometric curves (Figure 1) and results of measurement of microhardness and investigations of microstructure of the dilatometric specimens were used. Metallographic analysis of the specimens after cooling allowed specifying percent ratio of the structural components. Results of dilatometric analysis of the phase transformations at different rates of cooling of the S355J2G3 steel are presented in the Table.

Dilatograms of the S355J2G3 steel, obtained experimentally at different values of the cooling rate, are presented in Figure 1, and the ADA diagram --- in Figure 2.

Numerical investigations of deformation and kinetics of phase transformations in the S355J2G3 steel in similar thermal cycles for cooling rate  $w_{8/5} = 0.5$ ,

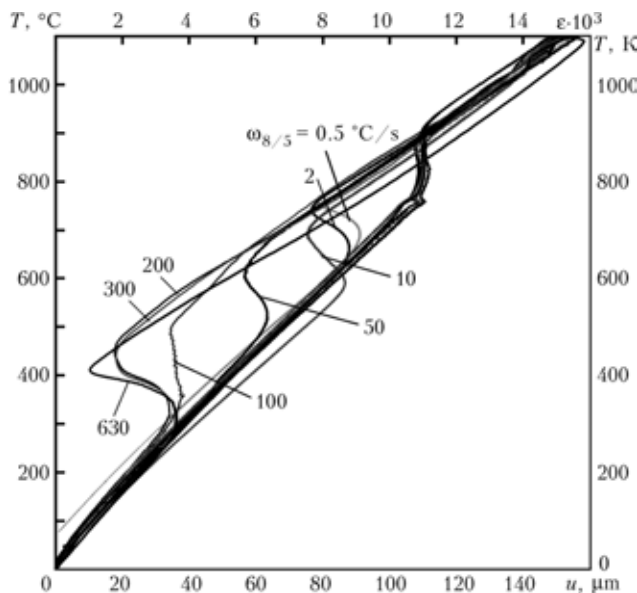


**Figure 1.** Experimental dilatograms of S355J2G3 steel obtained at different rates of cooling:  $\sigma$  --- stress;  $u$  --- shift



Influence of cooling rate on phase transformations in S355J2G3 steel

$w_{8/5}, \text{ }^{\circ}\text{N/s}$	HV 0.05	Critical points of phase transformation, $^{\circ}\text{C}$								Final composition of structure
		$M_s$	$M_f$	$B_s$	$B_f$	$F_s$	$F_f$	$P_s$	$P_f$	
0.5	130					778	715	715	617	~ 0.65 F, 0.35 P
2	160					769	695	695	592	~0.64 F, 0.36 P
10	179			520	405	748	632	632	520	~0.59 F, 0.41 P
50	172	412	315	520	412	686	606	606	520	~0.31 F, 0.45 P, 0.24 B
100	199	409	265	530	409	621	530			~0.15 F, 0.40 P, 0.35 B, 0.10 $\dot{\text{I}}$
200	N/D	411	235	522	410					~0.15 F, 0.45 P, 0.40 $\dot{\text{I}}$

2, 10, 50, 100, 300, and 630  $^{\circ}\text{C/s}$  were carried out using presented model of phase transformations.

We assume values of coefficients of linear dilatation  $\alpha_{FP} \cdot 10^6$  (23.0; 12.7; 14.7; 13.0; 14.7 1/K) and changes of volume share of A, B, F, M and P,  $V \cdot 10^{-3}$  = 2.3; 5.5; 3.5; 6.5, 3.5 (isotropic deformations of phase transformation) according to the experimental data. Coefficient of linear dilatation of the initial structure is, depending upon the temperature, precisely determined by function of the type

$$\alpha_{FP}(T) = -1.3787 \cdot 10^{-11} T^2 + 2.1866 \cdot 10^{-8} T + 6.7769 \cdot 10^{-6} \quad (6)$$

Coefficients of equation (6) are found provided values of the linear dilatation coefficient  $\alpha_{FP} \cdot 10^6$  = 12, 15 and 15 1/K respectively at temperature 20, 340 and 700  $^{\circ}\text{C}$ .

**Numeric simulation of HAZ structure in laser welding.** Temperature field is determined by equation of unsteady heat flow with a convective term of the kind

$$a \nabla^2 T(\mathbf{x}, t) - \frac{\partial T(\mathbf{x}, t)}{\partial t} + \nabla T(\mathbf{x}, t) \mathbf{v} + \frac{Q}{C} = 0, \quad (7)$$

where  $a = \lambda / c$  is the temperature equalizing coefficient;  $c$  is the specific heat capacity;  $Q$  is the volumetric heat source power;  $\mathbf{x} = \mathbf{x}(x, y, z)$  is the vector of the considered point position;  $\mathbf{v} = \mathbf{v}(\mathbf{x}, t)$  is the vector of the laser beam movement speed.

Equation (7), solved by the method of Green's function superposition, suggested in [7], consists in integration of Green's function in volume in the form of a prism ( $-\infty < x, y < \infty, 0 \leq z < \infty$ ) with initial and boundary conditions

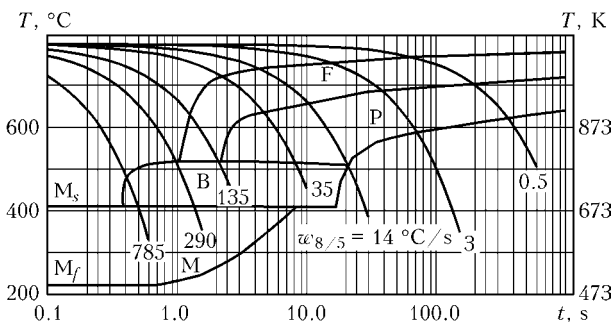


Figure 2. ADA diagram for S355J2G3 steel

$$T(\mathbf{x}, t) = 0, \quad \begin{cases} \mathbf{x}, y \rightarrow \pm \infty, \\ z \rightarrow \infty, \end{cases} \quad q = -\lambda \frac{\partial T(\mathbf{x}, t)}{\partial z} = 0, \quad z = 0. \quad (8)$$

The model of a semi-infinite body with origin of the coordinate system  $\{x', y', z'\}$  in the point of the welding heat source is accepted (Figure 3).

In the algorithm of solution the technique of fictitious sources was used. It was assumed that a stationary solution exists for time  $t$ , and mobile coordinate system  $\{x', y', z'\}$  moves relative the base coordinate system at the speed  $\mathbf{v} = \mathbf{v}(u, 0, 0)$  parallel to axis  $x$ .

Temperature field in the considered point determines source of heat with distribution of power in the form

$$Q(\mathbf{x}') = \begin{cases} Q(1 - R)/(\pi r^2 h_z), & x' = 0, y' = 0, -h_z \leq z' \leq h_z, \\ 0, & |z'| > h_z, \end{cases} \quad (9)$$

where  $h_z$  is the depth of laser penetration;  $R$  is the coefficient of reflection;  $r$  is the laser beam radius.

Temperature in the considered area is expressed due to the heat load in the form

$$T_1(\mathbf{x}, t) = \frac{1}{C} \int_0^t \int_V Q(\mathbf{x}', t') G(|\mathbf{x} - \mathbf{x}'|, t - t') dV dt'. \quad (10)$$

Integrating (10) on space coordinates and taking into account (9) we obtain

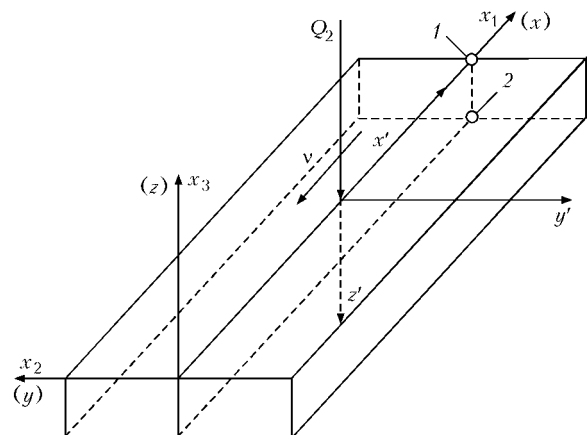
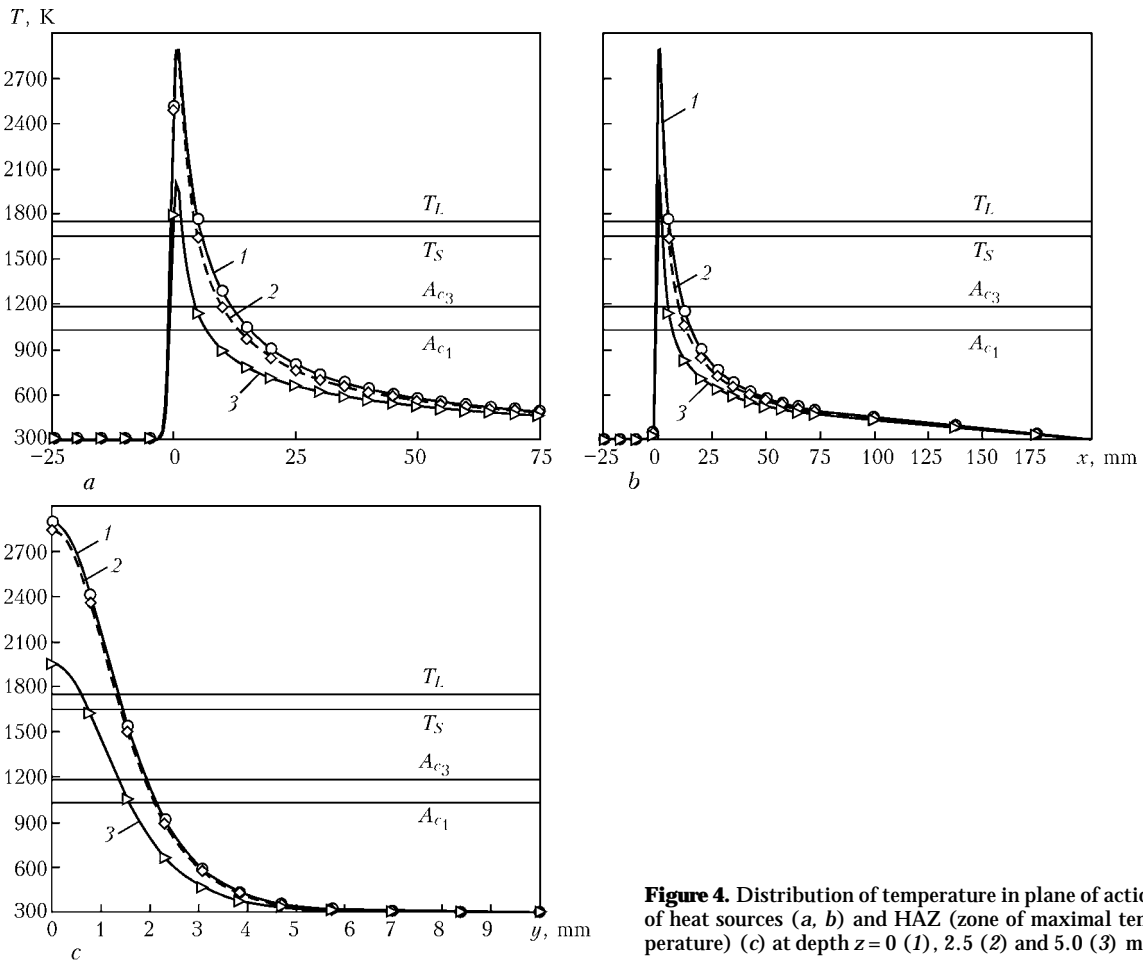


Figure 3. Model of semi-infinite body: 1, 2 --- investigated points respectively on upper and lower surfaces of specimen



**Figure 4.** Distribution of temperature in plane of action of heat sources (a, b) and HAZ (zone of maximal temperature) (c) at depth  $z=0$  (1), 2.5 (2) and 5.0 (3) mm

$$T(\mathbf{x}, t) = \int_0^t \frac{Q(1-R)}{4\pi h_z C(2a(t-t') + r^2)} \times \exp\left(\frac{[x - u(t-t')]^2 + y^2}{4a(t-t') + 2r^2}\right) \times \left[ \operatorname{erfc}\left(\frac{z - h_z}{2\sqrt{a(t-t')}}\right) - \operatorname{erfc}\left(\frac{z - h_z}{2\sqrt{a(t-t')}}\right) \right] dt' + T_0. \quad (11)$$

Numeric simulation of the laser welding process is made for a specimen of  $100 \times 20 \times 5$  mm size. Accepted in the calculations power of the heat source  $Q = 3.8$  kW at diameter of the beam 2 mm. We consider that the heat source moves at the speed 42 m/h. Let us assume that coefficient of reflection  $R = 0.25$ . Phase transformations are determined according to presented in the work model. In the calculations ADA diagram of the S355J2G3 steel was used (see Figure 2).

Temperature, volume share of phases in HAZ and deformations, formed at preset loads in the process of welding, are shown in Figures 4–9.

So, suggested numeric model of phase transformations makes it possible to estimate state of the metal structure in HAZ using experimentally established values of coefficients, which characterize volume changes that occur during phase transformations at a

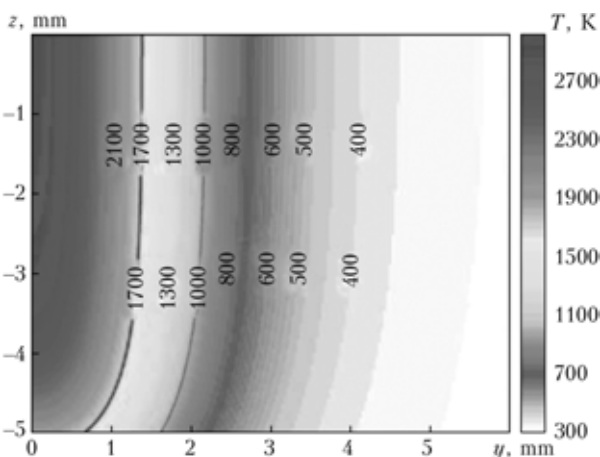


**Figure 5.** Isotherms of temperature in HAZ metal (zone of maximal temperature)

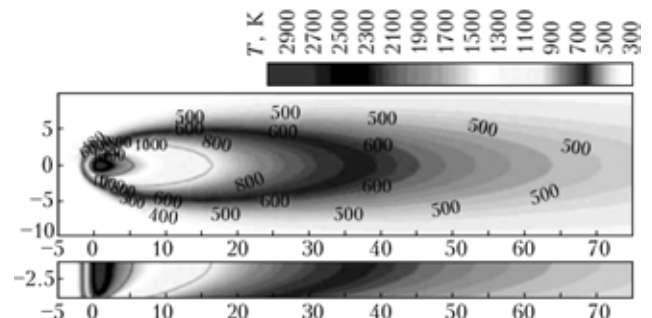


**Figure 6.** Distribution of temperature in plane of action of heat sources

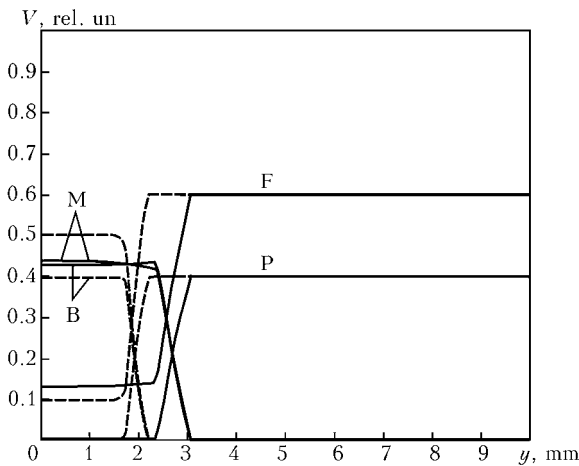


**Figure 7.** Volume share of phases  $V$  in metal of upper (solid curves) and lower (dash curves) surfaces of specimen

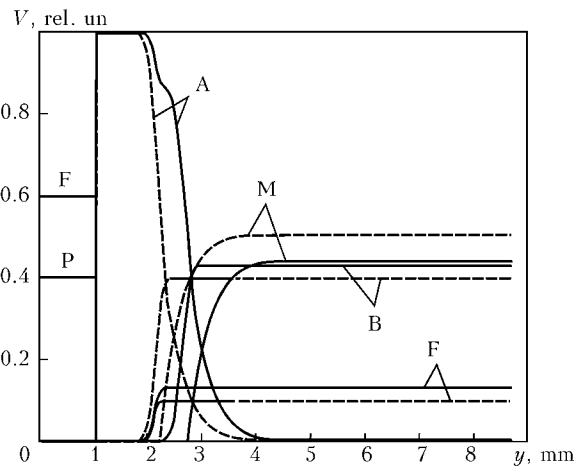


**Figure 8.** Kinetics of phase transformations in points 1 and 2 (see Figure 3) on upper (solid curves) and lower (dash curves) surfaces of specimen

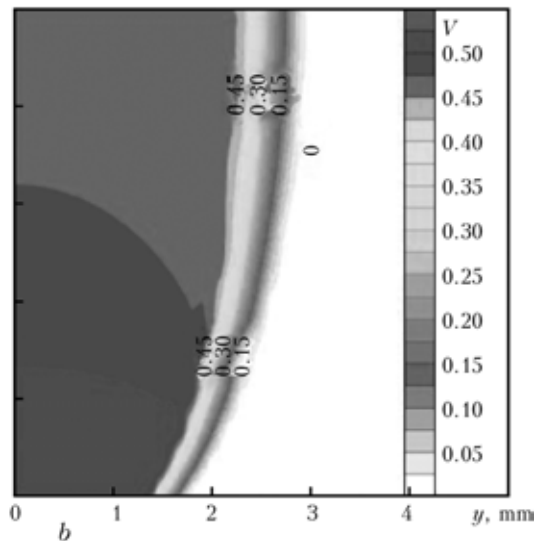
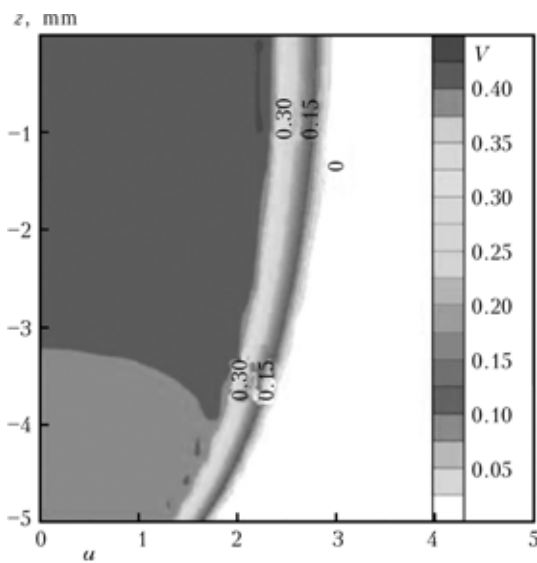


**Figure 9.** Isograms of bainite (a) and martensite (b) in HAZ after welding

certain temperature. As a result one may find real level of strains and use these data in calculations of temporary and residual stresses.

In case of laser welding at  $w_{8/5} \approx 300$  K/s, HAZ is narrow (see Figures 5 and 9). In laser welding of sheets from the S355J2G3 steel of 5 mm thickness a martensite component is formed in HAZ (see Figures 7–9), while in welding using other methods it is practically absent.

1. Makhnenko, V.I., Velikoivanenko, E.A., Makhnenko, O.V. et al. (2000) Investigation of effect of phase transformations on residual stresses in circumferential welding of pipes. *The Paton Welding J.*, **5**, 2–7.
2. Coret, M., Combescure, A. (2002) A mesomodel for the numerical simulation of the multiphasic behavior of materials under anisothermal loading (application to two low-carbon steels). *Int. J. Mech. Sci.*, **44**, 1947–1963.
3. Bokota, A., Pekarska, V. (2004) Stress state of welded joints made by laser welding with heating. In: *Proc. of Int. Conf. on Mathematical Modeling and Information Technologies in Welding and Related Technologies* (Katsiveli, Crimea, Sept. 13–17, 2004). Ed. by V.I. Makhnenko. Kiev: PWI, 32–37.
4. Maiti, A. De S.K., Walsh, C.A., Bhadeshia, H.K.D.N. et al. (2003) Finite element simulation of laser spot welding. *Sci. and Techn. Welding and Joining*, **8**, 377–384.

5. Kempen, A.T.W., Sommer, F., Mittemeijer, E.J. (2002) The kinetics of the austenite-ferrite phase transformation of Fe–Nb: differential thermal analysis during cooling. *Acta Materialia*, **50**, 3545–3555.
6. Makhnenko, V.I., Saprykina, G.Yu. (2002) Role of mathematical modeling in solving problems of welding dissimilar steels. (Review). *The Paton Welding J.*, **3**, 14–25.
7. Kulik, V.M., Vasiliev, V.G. (2006) Variations in structure and properties of HAZ metal in welded joints on steel 30KhGSA in arc treatment. *Ibid.*, **7**, 16–21.
8. Elmer, J.W., Palmer, T.A., Zhang, W. et al. (2003) Kinetic modeling of phase transformations occurring in the HAZ of C–Mn steel welds based on direct observations. *Acta Materialia*, **51**, 3333–3349.
9. Makhnenko, V.I., Velikoivanenko, E.A., Kravtsov, T.G. et al. (2001) Numerical studies of thermomechanical processes in surfacing of shafts of ship mechanisms. *The Paton Welding J.*, **1**, 2–10.
10. Kyrsanidi, An., Kermanidis, Th.B., Pantelakis, Sp.G. (1999) Numerical and experimental investigation of the laser forming process. *J. Mater. Proc. Techn.*, **87**, 281–290.
11. Pekarska, V. (2004) Phase transformations in HAZ metal of welded joints made by laser welding with heating. In: *Proc. of Int. Conf. on Mathematical Modeling and Information Technologies in Welding and Related Technologies* (Katsiveli, Crimea, Sept. 13–17, 2004). Ed. by V.I. Makhnenko. Kiev: PWI, 220–224.
12. Cheng-Ji, Notis, M.R. (1995) Continuous cooling transformation kinetics of steels: a phenomenological rationalization of experimental observations. *Materials Sci. & Eng. R*, **15**, 135–208.



13. Chun-Ming, L., Sommer, F., Mittemeijer, E.J. (2002) Characteristics of the  $\gamma \rightarrow \alpha$  transformation in Fe-Mn alloys. *Ibid.*, **325**, 307–319.
14. Melander, M. (1985) *Computational and experimental investigation of induction and laser hardening*: Linköping Studies in Sci. and Techn. Dissertation 124. Linköping.
15. Serajzadeh, S., Karimi Taheri, A. (2004) A study on austenite decomposition during continuous cooling of a low carbon steel. *Materials and Design*, **25**, 673–679.
16. Shen, H., Shi, Y., Yao, Z. (2006) Numerical simulation of the laser forming of plates using two simultaneous scans. *Computational Materials Sci.*, **37**, 239–245.
17. Silva, E.P., Pacheco, P.M., Savi, M.A. (2004) On the thermomechanical coupling in austenite-martensite phase transformation related to the quenching process. *Int. J. Solid and Structures*, **41**, 1139–1155.
18. Seyffarth, P., Kasatkin, O.G. (2004) Calculation models for evaluation of mechanical properties of HAZ metal in welding of low-alloy steels. In: *Proc. of Int. Conf. on Mathematical Modeling and Information Technologies in Welding and Related Technologies* (Katsiveli, Crimea, Sept. 13–17, 2004). Ed. by V.I. Makhnenko. Kiev: PWI, 103–106.
19. Lankalapalli, K.N. (1997) Model-based weld penetration depth estimation. *Welding in the World*, **39**, 304–313.
20. Liu, Y.-N., Kannatey-Asibu, E., Jr. (1993) Laser beam welding with simultaneous Gaussian laser preheating. *J. Heat Transfer. Transact. of ASME*, **115**, 34–41.

## EFFECT OF MICROPLASMA SPRAYING PARAMETERS ON STRUCTURE, PHASE COMPOSITION AND TEXTURE OF HYDROXYAPATITE COATINGS

Yu.S. BORISOV, A.L. BORISOVA, A.Yu. TUNIK, M.V. KARPETS, S.G. VOJNAROVICH,  
A.N. KISLITSA and E.K. KUZMICH-YANCHUK  
E.O. Paton Electric Welding Institute, NASU, Kiev, Ukraine

Hydroxyapatite (HA) coatings were deposited on a titanium alloy substrate by the microplasma spraying (MPS) method. The method of factorial experiment with fractional replicas was used to study relationship between the MPS parameters (current, plasma gas flow rate, spraying distance, and powder consumption) and characteristics of the HA coatings (microstructure, morphology, content of crystalline and amorphous phases, and texture). The effect of coating thickness and subsequent heat treatment of the deposited layer on phase composition and texture of the coatings was calculated. The results demonstrate that the coating formation process has some special features under the MPS conditions.

*Keywords:* microplasma spraying, hydroxyapatite, process parameters, properties of coatings, texture, investigations, regression analysis

Hydroxyapatite (HA) coatings on metal implants provide the triple positive effect: accelerated formation of bone tissue, capability of forming bonds with a bone (osteointegration), and decrease in contamination with metal corrosion products. Plasma coatings, taking an important place among the solutions offered, have a number of drawbacks, which are associated with a high temperature of the plasma jet and mismatch between the thermal expansion coefficients of metal and HA ceramics.

Moreover, intensive heating of the HA particles in the plasma jet and their instantaneous cooling on the substrate allow, on the one hand, formation of the amorphous phase (AP) in structure of a coating, whereas, on the other hand, the presence of HA in the plasma jet creates the possibility for its decomposition to form oxy-hydroxyapatite and oxyapatite (OA), formation of calcium-deficient hydroxyapatite, and phase transformation of HA into tricalcium phosphate (TCP), tetracalcium phosphate, or even toxic CaO [1–3]. These phases are less resistant to resorption than stoichiometric HA, which leads to changes in the osteointegration process.

At the same time, it is a known fact that the AP-containing HA coatings have higher mechanical properties than fully crystalline coatings. In this connec-

tion, the subjects of the discussions are the optimal phase composition and structure of the HA coatings providing the combination of biological compatibility and good mechanical properties.

On the one hand, it is required that HA be maximum possible crystalline, whereas, on the other hand, it is necessary to leave some (up to 15 %) amount of AP, the dissolution of which leads to acceleration of fixation of an implant and growth of a bone. However, in both cases it is necessary to provide the possibility of controlling the structure and composition of HA by regulating parameters of the deposition process.

Some studies in this field are dedicated to calculation of the effect of different parameters of plasma spraying on characteristics of the HA coatings, and phase composition in particular. The effect of such parameters as plasmatron power and spraying distance [4–6], plasma gas composition, transporting gas composition, and position of the point of introduction of a powder [7] was also analysed. It seems correct that this analysis be conducted by using an approach, with which the object of the analysis is a HA particle, during the process of melting of which three zones can be distinguished in its cross section: non-molten nucleus, melt of stoichiometric HA, and external layer with the highest heating level, containing dehydroxylated HA and its decomposition products [2, 4, 8]. Structure and properties of the formed coatings depend upon the proportion of these zones, which, in turn, depends upon the conditions of heating of a



moving particle and conditions of its cooling in deposition on the substrate.

Heating of the particles in plasma spraying occurs under conditions of non-stationary thermal conductivity. Dynamics of heating and distribution of temperature fields inside a particle depend upon the Biot and Fourier criteria. In this case, an important role is played by the coefficient of heat transfer from gas to the surface of a particle, related to the thermal conductivity of gas. Increase of the latter leads to increase of the temperature gradient inside the particle and rapid overheating of its surface. This phenomenon may occur in the case of using argon, hydrogen or helium mixtures, which are widely employed in deposition of the HA coatings, as a plasma gas. The negative effect showing up with increase in the amount of hydrogen in the mixture was experimentally proven in study [7].

Calculation-theoretical analysis of the formation of amorphous structure under conditions of thermal spraying made it possible to establish the main factors affecting this process [9]. First of all, these are thickness, temperature and thermal-physical characteristics of both cooled splat and substrate, on which it was deposited, as well as properties of the gas jet expressed in the thermal effect on the «splat–substrate» system.

Another characteristic of HA, which determines its biological activity and mechanical properties, is texture of a structure. It is a known fact that ions  $Ca^{2+}$  move along axis  $c$  much more easily than normal to it. This is associated with a of high probability of the formation of defects in columns of  $Ca^{2+}$  [10]. The probability of the formation of texture in a HA coating along axis  $c$  was fixed under the conditions of spraying with a high-frequency plasma [11, 12].

The purpose of this study was to investigate the effect of different parameters of microplasma spraying (MPS) on characteristics of the HA coatings, as well as determine the efficiency of impact on the coating properties by such a method of controlling the phase composition as heat treatment of the deposited coatings.

Experimental data were generated by using the experimental design method. The effect of different parameters both on phase composition of a coating and on probability of the formation of texture in it was considered.

**Experimental procedure.** The HA powder with 50–80  $\mu m$  particles, having a fragmented shape with a high difference in sizes along the particle axes, was used as a spraying material. This fraction of the powder is characterised by a flow rate of 120–124 s/50 g, apparent density of 1.07 g/cm<sup>3</sup> and density of the particles equal to 2.995 g/cm<sup>3</sup>. Phase composition of the powder consisted of fully crystalline  $Ca_{10}(PO_4)_6(OH)_2$ , Ca/P --- 1.67.

Diffraction of the initial powders and coatings was performed with the DRON-UM1 diffractometer in monochromatic  $CuK\alpha$ -radiation by step-by-step scanning (35 kV, 35 mA, time of exposure at a point ---

7 s, step --- 0.05°). Graphite single crystal installed on a diffracted beam was used as a monochromator. A sample during filming was rotated about a normal to the coating surface.

The conventional method for determination of phase composition and crystallinity of the HA coatings, consisting in analysis of the X-ray diffraction peaks located within the  $2\theta = 25\text{--}40^\circ$  angle ranges [4, 13], is unsuitable for the textured coatings. In this case, many X-ray diffraction peaks may be located also at the  $2\theta = 37\text{--}65^\circ$  angles. Therefore, the diffractometry data (assuming the presence of texture in the majority of coatings) were processed by using the «PowderCell 2.4» software programs to ensure a full-profile analysis of X-ray spectrum of a mixture of polycrystalline phase components.

The texture was studied by using the March–Dollas model, and profiles of the diffraction maxima were approximated by the pseudo-Hoight function. The content of AP was determined by using the GSAS software package. Morphology and chemical composition of the microplasma HA coatings were studied by depositing a thin carbon layer on their surface using the vacuum method. Examinations were conducted with the Cameca microscope «Camebax» SX-50. The effect of thickness of the HA coating on its phase composition and texture was evaluated by analysing coatings of different thicknesses, and by the method of layer-by-layer X-ray control (step --- 50  $\mu m$ ).

The MPS-004 system with the MP-03 plasmatron was employed to deposit the HA coatings [14, 15].

**Experimental design and regression analysis of the process of MPS of HA coatings.** The process of deposition of coatings by the thermal spraying method is categorised as a multifactorial one. The quantity of factors affecting properties of the coatings amounts to 60 or more. Therefore, at present the most suitable way of analysing numerous interferences between parameters of thermal spraying and properties of the coatings is use to statistical experimental design methods. The MPS experimental design was developed to evaluate the effect of different process parameters on key characteristics of the HA coatings (crystallinity, content of  $\beta$ -TCP and CaO, texture, etc.). The use

**Table 1.** Conditions of microplasma spraying

Experiment No.	$I, \text{ \AA}$	$V_{p,g}, \text{ l/min}$	$h, \text{ mm}$	$G_p, \text{ g/min}$
1	45	2	160	1.2
2	45	2	80	0.4
3	45	1	160	0.4
4	45	1	80	1.2
5	35	2	160	0.4
6	35	2	80	1.2
7	35	1	160	1.2
8	35	1	80	0.4
9	40	1.5	120	0.8

**Table 2.** Characteristics of microplasma HA coatings

Sample No. according to matrix	Phase composition*, wt. %			Texture coefficient $t$	Elementary cell parameters		
	HA	$\beta$ -TCP	AP		$\bar{a}$ , nm	$\bar{c}$ , nm	$V$ , nm <sup>3</sup>
Powder	100	0	0	1	0.9418	0.6881	0.5286
1	92	3	5	1	0.9403	0.6887	0.5273
2	98	2	0	0.53	0.9400	0.6876	0.5262
3	93	5	2	0.48	0.9386	0.6885	0.5252
4	96	4	0	0.61	0.9393	0.6884	0.5259
5	93	3	4	1	0.9400	0.6888	0.5271
6	94	3	3	1	0.9400	0.6881	0.5265
7	88	5	7	1	0.9394	0.6886	0.5262
8	98	2	0	0.69	0.9395	0.6883	0.5262
9	90	6	4	0.74	0.9395	0.6886	0.5263

\*All the samples contained no CaO.

was made of the method of factorial experiment with fractional replicas ( $2^{4-1}$ ). Current  $I$  (A), plasma gas flow rate  $V_{p.g}$  (l/min), spraying distance  $h$  (mm) and powder consumption  $G_p$  (g/min) were selected as the process variables. Conditions of the MPS experiment are given in Table 1.

The results of X-ray phase analysis of the composition, texture coefficient, lattice parameters ( $a$  and  $c$ ) and elementary cell volume  $V$  are given in Table 2.

One should note changes in lattice parameters of the coatings, compared with the initial powder. Parameter  $a$  decreases from 0.9418 to 0.9386–0.9403, parameter  $c$  increases from 0.6881 to 0.6883–0.6888, and volume of an elementary cell of the lattice decreases from 0.5286 to 0.5252–0.5273. These results

correspond to the data obtained in spraying of the HA coatings by the HVOF method [2], and indicate that the coatings contain no OA, the formation of which is characterised by a substantial decrease in parameter  $a$ .

Linear regression models were determined for all characteristics of the coatings (HA,  $\beta$ -TCP, AP, and  $t$ ). The following regression equations were derived to calculate all these characteristics:

$$\begin{aligned} \text{HA} &= 97.75 + 0.15I + 0.5V_{p.g} - 0.063h - 3.75G_p; \\ \beta\text{-TCP} &= 1.62 + 0.025I - 1.25V_{p.g} + 0.016h + 0.94G_p; \\ \text{AP} &= 0.625 - 0.18I + 0.75V_{p.g} + 0.047h + 2.81G_p; \\ t &= 0.73 - 0.022I + 0.232V_{p.g} + 0.026h + 0.34G_p. \end{aligned}$$

Comparison of the calculation and experimental results obtained with sample No. 9 has the following form (numerator --- experiment, and denominator --- calculation, respectively): HA, % --- 90/94;  $\beta$ -TCP, % --- 6/3.4; AP, % --- 4/2.6;  $t$  --- 0.74/0.76.

**Results and discussion.** Analysis of topography of the surface and microstructure of the coatings makes it possible to subdivide them into three groups in their characteristics and spraying conditions. In the case of morphology of the coating surface, this is the surface consisting of almost completely molten and deformed particles (experiments Nos. 3, 4, 9); the surface containing solidified spherical particles on the substrate of molten and deformed particles was found in experiments Nos. 1, 2, 5, 6 and 8; and surface consisting of conglomerates of solidified spherical particles was found in experiment No. 7. Microstructure and morphology of the coatings belonging to these groups are shown in Figure 1.

The first and second groups contain the similar amounts of HA (92–96 and 93–98 %, respectively). The contents of  $\beta$ -TCP and especially AP are different. The main difference is observed in the texture coefficient (the first group --- 0.48–0.61, and the second group --- mostly 1).

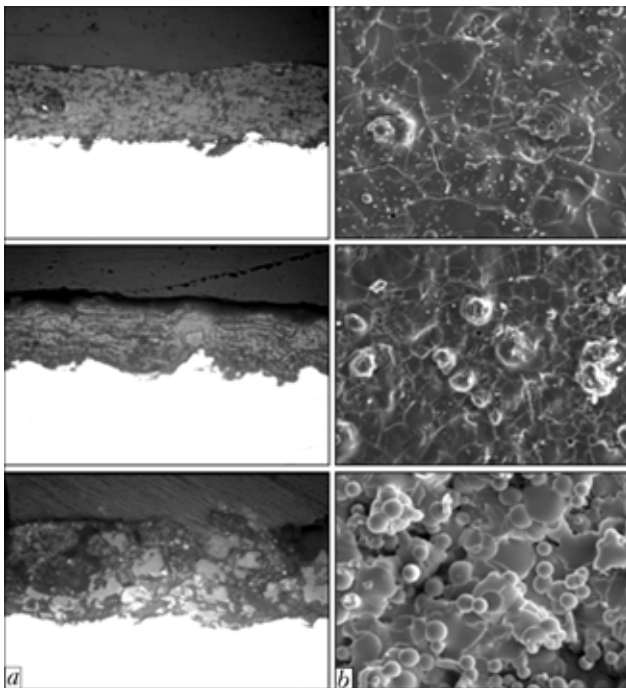


**Figure 1.** Microstructure ( $a$  ---  $\times 200$ ) and morphology ( $b$  ---  $\times 400$ ) of HA coatings belonging to different groups: downward --- samples Nos. 4, 2, 7



X-ray patterns of the coatings produced in conditions Nos. 2–4 show the presence of texture (peaks in the  $2\theta = 37\text{--}65^\circ$  angle ranges, Figure 2). This means that there is a difference in cooling of the deposited layers between these two groups. Owing to slowing down of the solidification process, decrease in the cooling rate leads to the formation of texture. Probably, the main cause of the formation of the latter in the microplasma HA coatings is a relatively low kinetic energy of the spraying particles (under the MPS conditions, the velocity of particles is 50–60 m/s), as well as the formation of thick splats of the HA particles. This is in agreement with the results obtained in high-frequency plasma spraying of the HA coatings, where the velocity of the particles was also insignificant, thus resulting in the formation of layers with orientation of the HA structure along axis  $c$  [11, 12].

The high degree of crystallinity and low content of  $\beta$ -TCP in the microplasma HA coatings are the results of special features of the thermal processes occurring under the above conditions. Decrease in thermal conductivity of the plasma gas, caused by utilisation of pure argon instead of the Ar + H<sub>2</sub> and Ar + He mixtures, provides decrease in temperature gradient in the HA particles in a period of their heating in plasma. This allows decreasing overheating of the upper layer of the particles and suppressing the process of loss of [OH<sup>-</sup>] and decomposition of HA.

Analysis of the regression equations made it possible to evaluate the effect of each of the parameters and determine their role in the formation of a combination of characteristics of the HA coatings. The effect was evaluated as a result of activity of a parameter under conditions of two different processes: heating and acceleration of particles during their flight in the plasma jet, and deformation and cooling of the particles on the substrate surface. The most active parameter is spraying distance  $h$ , the growth of which leads, on the one hand, to increase in the time of dwelling of the particles in the plasma jet and development of the process of decomposition of HA (HA decreases,  $\beta$ -TCP increases), and, on the other hand, to decrease in the substrate temperature and increase in the rate of cooling of the particles (AP and texture coefficient increase).

Growth of current  $I$  leads to a more intensive heating and melting of the particles, which results in partial decomposition of HA ( $\beta$ -TCP increases). However, then the hot particles and heat from the plasma jet increase the substrate temperature, thus decreasing the rate of cooling of the particles. As a result, the AP content and texture coefficient decrease, and HA increases (probably, as a result of crystallisation of AP [4]).

The plasma gas flow rate affects the temperature and velocity of the plasma jet. Therefore, increase in the plasma gas flow rate leads to decrease in temperature of the plasma jet and particles, reduction in the time of heating of the particles and suppression of the process of decomposition of HA (HA increases, and

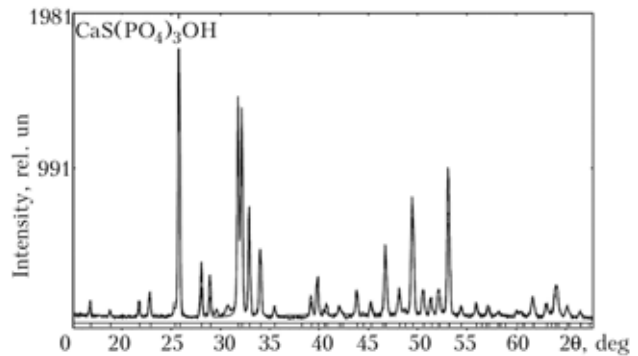


**Figure 2.** X-ray pattern of textured microplasma coating (experiment No. 2; HA/ $\beta$ -TCP/AP — 98/2/0;  $t = 0.53$ )

$\beta$ -TCP decreases). However, this leads to decrease in the substrate temperature, thus promoting amorphisation of the coating structure (AP and texture coefficient increase).

The powder consumption has a complex effect on the MPS process. Under conditions of the latter, density of the powder in a gas flow is higher than in traditional plasma spraying, as diameter of the plasma jet is 2–3 mm, and size of the spraying spot is 3–6 mm. This means that loading of the spraying spot with the HA particles is 4–10 g/(min·cm<sup>2</sup>), whereas for traditional plasma spraying this value is 2–3 g/(min·cm<sup>2</sup>). Volume concentration of the HA particles in the microplasma jet under these conditions amounts to  $10^{-3}$  –  $10^{-4}$  cm<sup>3</sup>/cm<sup>3</sup>, which may result in the probability of numerous collisions between the particles and, by decreasing their velocity, increase the time of their dwelling in the jet. This causes the similarity of the effect exerted by this parameter to the effect of the spraying distance (HA decreases, and  $\beta$ -TCP, AP and texture coefficient increase). However, this fact requires further investigation. As a whole, it should be noted that heating of a particle in MPS occurs under the conditions of decrease in temperature gradient of the HA particles. This allows decreasing overheating of the upper layer of the particles and suppressing the process of loss of [OH<sup>-</sup>] and decomposition of HA, thus providing the HA coatings with a high degree of crystallinity. Slow cooling of the particles in cooling on the substrate leads to the formation of texture in the deposited HA coatings.

**Effect of thickness of the deposited layer on phase composition and texture of microplasma HA coatings.** Diffractometry examinations of the HA coatings of different thicknesses (from 80 to 360  $\mu$ m) produced under the following process conditions:  $I = 45$  A,  $U = 28$  V,  $V_{p.g} = 2$  l/min,  $G_p = 1.2$  g/min,  $h = 100$  mm, as well as layer-by-layer diffractometry analysis of the coatings 360  $\mu$ m thick with subsequent grinding off of the layers were carried out. Analysis of the diffractometry results allows a conclusion that phase composition of the sprayed coatings and their texture depend upon the thickness of a deposited layer. Thus, coatings up to 100  $\mu$ m thick have either no texture at all, or an insignificant texture ( $t \sim 0.9$ ), the AP content being 7–9 wt.%. At a coating thickness of more than 100  $\mu$ m, the texture coefficient decreases

**Table 3.** Characteristics of phase composition and lattice parameters of HA coatings after heat treatment

Sample No. according to matrix	Temperature, °C	Phase composition, wt.%			Texture coefficient $t$	Elementary cell parameters		
		HA	$\beta$ -TCP	AP		$a$ , nm	$\bar{a}$ , nm	$V$ , nm <sup>3</sup>
Powder	---	99	0	0	1	0.9941	0.6875	0.5275
1	20	44	21	35	0.77	0.93803	0.6896	0.5254
1	600	89	7	4	0.77	0.9404	0.6893	0.5280
1	700	86	9	5	0.82	0.9404	0.6893	0.5280
2	20	95	5	0	0.45	0.9375	0.6899	0.5251
2	600	95	5	0	0.44	0.9393	0.6902	0.5274
2	700	95	5	0	0.45	0.9392	0.6901	0.5273
3	20	74	11	15	1	0.9379	0.6896	0.5254
3	600	96	4	0	0.92	0.9402	0.6898	0.5281
3	700	96	4	0	0.93	0.9404	0.6902	0.5286

to 0.7, and the AP content --- to 4–5 wt.%. In a coating 360  $\mu\text{m}$  thick, the degree of texture also increases ( $t = 0.34$ ), and the amount of AP decreases to 2 wt.%. The noted trend in the effect exerted by the coating thickness on texture and AP content is most apparent in layer-by-layer analysis of the coatings. For example, increase in thickness from 50 to 360  $\mu\text{m}$  demonstrates a stable growth of the degree of texture with decrease in the texture coefficient from 0.72 to 0.34 (Figure 3).

Characteristically, this dependence persists with an increase in thickness to 200  $\mu\text{m}$ . Further on, the degree of texture, AP content and phase composition remain at the same level.

**Effect of heat treatment on phase composition of microplasma HA coatings.** The effect of isothermal annealing on the process of transformation of  $\beta$ -TCP into HA and crystallisation of AP was studied. An-

nealing was conducted in argon atmosphere at a temperature of 600 and 700 °C for two hours. On the one hand, these temperatures relate to the range of stable existence of the HA phase, but, on the other hand, they include the temperature of beginning of crystallisation of the amorphous HA components (~630 °C).

Microplasma coatings of three compositions of HA were chosen for investigations: 1 --- with a high content of AP (about 35 wt.%) and  $\beta$ -TCP (about 21 wt.%) ; 2 --- without AP and with a small amount of  $\beta$ -TCP (approximately 5 wt.%) ; and 3 --- an intermediate variant --- with 18 wt.%  $\beta$ -TCP and 15 wt.% AP.

The texture coefficient of HA was 0.77, 0.445 and 1 for coatings 1–3 respectively. Analysis of the results given in Table 3 showed that because of isothermal annealing the content of AP and  $\beta$ -TCP decreased in samples Nos. 1 and 3, and the content of HA grew accordingly. AP in sample No. 3 (15 wt.% of the total composition) was completely transformed into crystalline HA, and the amount of  $\beta$ -TCP decreased to 4 wt.% (more than by a factor of 2.5). This process was accompanied by the formation of texture ( $t = 0.92$ ). In sample No. 1 with a high AP content (35 wt.%), the crystallisation process was not complete (the residual content of AP was about 5 wt.%), and the amount of the  $\beta$ -TCP phase decreased 2.5–3 times.

No changes were revealed in heat treatment of sample No. 2 with a high degree of texture ( $t = 0.45$ ), containing an insignificant amount of  $\beta$ -TCP (about 5 wt.%) and no AP. The lattice parameters and volume of an elementary cell increase after annealing. Therefore, the degree of texture persisted in textured coatings in transformation of  $\beta$ -TCP into HA. If the initial coating was not textured, annealing was accompanied by the formation of texture and transformation of  $\beta$ -TCP into HA.

It can be noted in conclusion that correlation between parameters of the regression equations makes it possible to find the ways to control structure and phase composition of HA under the MPS conditions through:

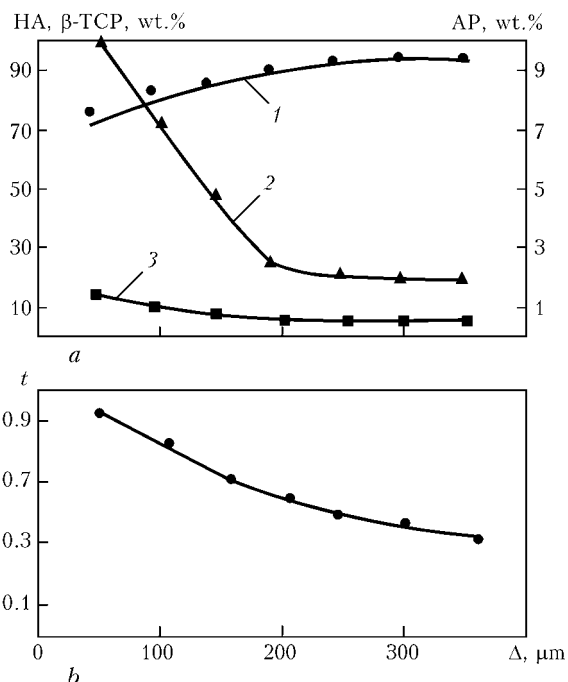


**Figure 3.** Variations in phase composition (a) and texture (b) through thickness  $\Delta$  of HA coating: 1 --- HA; 2 --- AP; 3 ---  $\beta$ -TCP



- increasing the current and spraying distance, which leads to growth of the crystalline phase of HA and decrease in the amorphisation degree;
- increasing the current, spraying distance, plasma gas flow rate and powder consumption, which promotes the formation of texture;
- increasing the plasma gas flow rate, decreasing the spraying distance and powder consumption, which promotes decrease in the  $\beta$ -TCP content of the coatings.

Investigations of the effect of thickness of the coatings on their phase composition and texture showed that the amounts of AP and  $\beta$ -TCP increased with decrease in thickness of the HA coatings below 200  $\mu\text{m}$ . In this case, the texture coefficient turned out to be more sensitive to the coating thickness, and permanently grew in a direction from the coating surface to the substrate, especially at a thickness of less than 200  $\mu\text{m}$ .

Heat treatment of the HA coatings at 600–700 °C leads to partial transformation of  $\beta$ -TCP and AP into HA, the texture coefficient remaining unchanged (being the same as in the as-sprayed coatings). At the same time, if texture was not formed in the initial coating, it would be formed in heat treatment.

- Xue, W., Tao, Sh., Liu, X. et al. (2004) In vivo evaluation of plasma sprayed hydroxyapatite coatings having different crystallinity. *Biomaterials*, **25**, 415–421.
- Fernandez, J., Guilemany, J.M., Gaona, M. (2005) High crystallinity degree hydroxyapatite coatings using HVOF spraying. In: *Thermal spray connects: explore its surfacing potential* (2–4 May, 2005). Basel: ASM Int., 1219–1224.
- Khor, K.A., Li, H., Cheang, P. (2004) Significance of melt-fraction in HVOF sprayed hydroxyapatite particles, splats and coatings. *Biomaterials*, **25**, 1177–1186.
- Sun, L., Berndt, C.C., Gross, K.A. (2005) Phase formation mechanisms in plasma sprayed hydroxyapatite coatings. In: *Thermal spray connects: explore its surfacing potential* (2–4 May, 2005). Basel: ASM Int., 563–568.
- Oh, K.T., Park, Y.S. (1998) Plasma-sprayed coating of hydroxyapatite on super austenitic stainless steels. *Surf. Coat. Technol.*, **110**, 4–12.
- Sun, L., Berndt, C.C., Lima, R.S. et al. (2000) Effects of spraying parameters on phase formation and distribution in plasma-sprayed hydroxyapatite coatings. In: *Thermal spray surface engineering via applied research* (8–11 May, 2000). Montreal: ASM Int., 803–811.
- Dyshlovenko, S., Pawlowski, L., Roussel, P. (2005) Experimental investigation of influence of plasma spraying operational parameters on properties of hydroxyapatite. In: *Thermal spray connects: explore its surfacing potential* (2–4 May, 2005). Basel: ASM Int., 726–731.
- Pawlowski, L. (1999) Thick laser coatings: A review. *Thermal Spray Technol.*, **8**(2), 279–295.
- Borisov, Yu.S., Korzhik, V.N. (1995) Amorphous thermal coatings. Theory and practice (Review). *Avtomatich. Svarka*, **4**, 3–11.
- Kanazawa, T. (1998) *Inorganic phosphate materials*. Kiev: Naukova Dumka.
- Inagasaki, M., Yokogawa, Y., Kameyama, T. (2003) Formation of highly oriented hydroxyapatite in hydroxyapatite/titanium composite coating by radiofrequency thermal plasma spraying. *J. Mater. Sci.: Mater. Med.*, **4**, 919–922.
- Bouyer, E., Gitzhofer, F., Boulos, M.I. (1995) Induction plasma spraying of hydroxyapatite. In: *Thermal spray & technology* (11–15 Sept., 1995). Houston: ASM Int., 339–344.
- Yushchenko, K., Borisov, Yu., Pereverzev, Yu. et al. (1998) Microplasma spraying. In: *Thermal spray: meeting the challenges of the 21st century* (25–29 May, 1998). Nice: ASM Int., 1461–1467.
- Borisov, Yu.S., Vojnarovich, S.G., Ulianchin, N.V. et al. (2002) Investigation of bioceramic coatings produced by microplasma spraying. *The Paton Welding J.*, **9**, 4–6.
- Lima, R.S., Khor, K.A., Li, H. et al. (2005) HVOF spraying of nanostructured hydroxyapatite for biomedical applications. *Mater. Sci. and Eng. A*, **96**, 181–187.

## ULTRASONIC DEVICE FOR MONITORING OF STRESSES

Residual welding stresses that may amount to high levels are among the main factors determining performance of welded structures. The E.O. Paton Electric Welding Institute in collaboration with the Research Institute «Kvant» (Kiev) developed and manufactured a small-size automated ultrasonic device to monitor stresses. Evaluation of stresses is based on the effect of acoustic elasticity. The processes of measurement and result processing are computerised. The measurement results are stored in the device memory, or they can be sent to PC. The distinctive feature of the device is in a new principle of reception and processing of ultrasonic oscillations, which allows automation of the measurement process and substantial increase in accuracy of determination of stresses.

**Purpose.** In-process non-destructive determination of value and sign of uni-, bi- and triaxial residual stresses in members of metal structures, monitoring of the field of residual stresses in postweld strengthening treatment during fabrication and operation of structures.

**Application.** Ship building, bridge construction, aircraft engineering.



General view of ultrasonic device for monitoring of stresses

Contacts: Prof. Kirian V.I.  
E-mail: office@paton.kiev.ua; kiryan@svitonline.com



# PHYSICAL AND TECHNOLOGICAL ASPECTS OF BRAZE-WELDING OF TITANIUM-ALUMINIUM JOINTS (Review)

A.S. MILENIN

E.O. Paton Electric Welding Institute, NASU, Kiev, Ukraine

Analysis of key problems arising in braze-welding of dissimilar joints of titanium and aluminium has been performed. Regularities of the processes determining the performance of dissimilar structures are shown. Recommendations on optimization of technological processes are given, which allow producing sound titanium-aluminium braze-welded components.

*Keywords:* braze-welding, titanium, aluminium, welded joints, intermetallic phases, constitutional diagrams, optimization of the joining process

At present the welded structural elements and components from dissimilar metals are becoming ever wider applied in different branches of industry.

Advantages of dissimilar welded parts compared to similar welded parts, are obvious. Application of light metals and alloys allows reducing the weight of individual elements, being particularly important in aerospace industry and car-making. Use of metals with a high corrosion resistance improves the service life of components contacting the aggressive media, for instance ships, off-shore structures and pipelines. Dissimilar welded components allow increasing the load-bearing rigidity of structural elements, lowering product cost by replacing an expensive alloy by a less costly analog [1-3].

However, producing dissimilar welded joints of a satisfactory quality involves certain difficulties, caused both by metallurgical incompatibility of the metals being welded, and technological features of welding [4-6].

Titanium-aluminium is one of the most promising pairs of structural materials in terms of a set of valuable service properties of the produced dissimilar welded joint. These metals are characterized by a high corrosion resistance in many aggressive media, good proportion of strength and ductility and comparatively low weight. In addition, titanium and alloys on its base have high strength characteristics. Some physical properties of these metals are given below (Table) [7, 8].

Physical characteristics	Titanium	Aluminium
Melting temperature, K	1941	933
Boiling temperature, K	3603	2767
Specific melting heat, kJ/kg	315.24	397
Specific boiling heat, kJ/kg	8559.5	10.777
Density, kg/m <sup>3</sup>	4505	2698

Heat conductivity, W/(m·K)	18.8	225.4
Specific heat capacity, kJ/(kg·K)	0.54	0.90
Young's modulus, GPa	112	72.5
Poisson's ratio	0.31	0.33
Linear expansion factor $\alpha \cdot 10^6$ , K <sup>-1</sup>	8.2	24.3
Tensile strength, MPa	262	150
Yield point, MPa	186	120
<i>Note.</i> Values of all physical characteristics, dependent on temperature, were taken at 20 °C.		

Thus, use of titanium-aluminium parts and components allows improvement of the mechanical and corrosion properties of structures, increasing their fatigue resistance, as well as extending their operating life [9, 10].

However, in order to produce sound titanium-aluminium welded joints at development and optimization of the respective welding cycle, it is necessary to take into account a number of difficulties, the inevitable appearance of which is due to the characteristic physico-chemical and metallurgical processes, as well as specifics of the selected welding technology.

An essential problem in welding of dissimilar joints of metals of a limited mutual solubility is the risk of formation in the contact area of different kinds of intermetallic phases, which may have an adverse effect on the welded structure quality.

As is seen from the constitutional diagram of the binary titanium-aluminium system (Figure 1), mutual solubility of these elements is low. While aluminium content in the titanium solid solution reaches 7 wt.%, thus allowing its effective application for alloying most of the titanium alloys, titanium is practically insoluble in aluminium, and TiAl<sub>3</sub> intermetallics precipitates in the solution already at its content above 0.03 wt.%. A considerable increase of the intermetallic phase content in the welded joint leads to an abrupt lowering of the structure mechanical properties, and makes its efficient operation impossible [11].

This fact does not allow applying for titanium-aluminium joints those welding processes, at which melt-



ing of both the metals occurs with subsequent mixing of their liquid phases. One of the possible solutions of this problem can be application of different processes of solid-phase welding (explosion welding, diffusion welding, etc.) [12, 13]. These technologies, however, introduce certain limitations on the joint geometry and considerable allowances for residual deformation of the joint, and in this connection are not always applicable.

A significant difference between the melting temperature of titanium and aluminium accounts for application of braze-welding as the most effective method of their joining.

The main idea of this process consists in that thermal impact of the welding source in the area of dissimilar contact results in melting of just the aluminium part of the item, whereas the titanium part remains solid. Wetting of solid titanium by molten aluminium and their surface interaction, result in formation of a braze-welded joint [2–4, 9–10, 14, 15]. The short-time duration of this interaction, as well as the relatively low temperatures in the area of dissimilar contact allows reducing the risk of formation of undesirable embrittling intermetallic layers, which in the considered case is attributable to the nature of the processes of reaction diffusion.

The process of the intermetallic layer formation at the dissimilar contact surface is conditionally divided into a number of successive stages [16]:

- relaxation of the peak of interphase energy on the liquid metal–solid metal boundary;
- formation of islets of the new phase in the sites of microdefect formation on the solid metal surface, growth of these islets along the contact surface and their coalescence into a continuous layer;
- normal diffusion growth of the intermetallic layer.

Thickness of the intermetallic layer formed during the first two stages, is small (less than 5  $\mu\text{m}$ ), which does not cause any essential lowering of the values of technological characteristics of the welded joint. Total duration of these stages determines the so-called latent period of intermetallic formation [10, 14]. It is exactly the presence of this period which allows avoiding the appearance in titanium and aluminium welded joints of brittle intermetallic layers of the thickness sufficient for a considerable deterioration of weldment performance.

Despite the fact that in the constitutional diagram of titanium–aluminium system (Figure 1) the presence of four stable intermetallic compounds is shown, in the case of titanium and aluminium braze-welding only a layer of  $\text{TiAl}_3$  stoichiometric compound can form, whereas the quantity of other intermetallic phases is either negligibly small, or they are absent completely. The author of [17] attributes that to the difference between the rate of formation of the intermetallic compound and rate of element penetration into the region of surface contact of liquid aluminium and solid titanium, where the chemical reaction proceeds. Du-

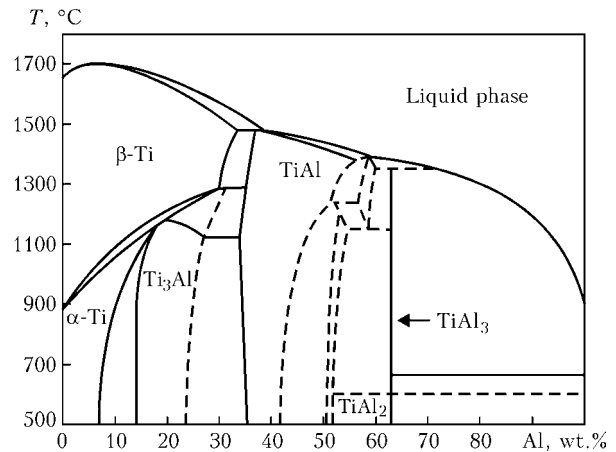


Figure 1. Constitutional diagram of binary titanium–aluminium system [9]

ration of the latent period, in its turn, is the function of temperature in the above region [4]. This temperature dependence derived experimentally is given in Figure 2.

Accordingly, optimization of a specific braze-welding process in order to eliminate long-term overheating in the area of titanium and aluminium contact allows lowering the risk of formation of intermetallic layers of a considerable thickness and avoiding degradation of service properties of a dissimilar welded structure.

The chemical reaction of formation of  $\text{TiAl}_3$  intermetallic is an exothermal one, so that local overheating in the field of dissimilar contact should be anticipated [7]. However, in view of a small thickness of the forming intermetallic layers, it is anticipated that the heat evolving as a result of this chemical reaction will not have any essential influence on the temperature field kinetics.

In addition, as the depth of interdiffusion penetration of titanium and aluminium atoms in the real processes of braze-welding is quite low, the risk of formation of pores and local deformations as a result of an essential difference in the partial coefficients of element diffusion (Kirkendall effect) is minimum [16].

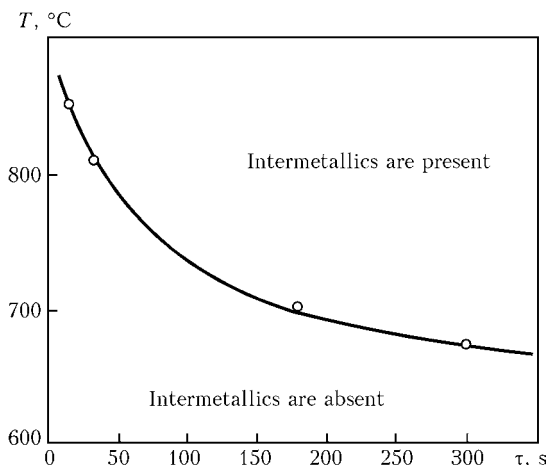


Figure 2. Temperature dependence of the duration of latent period of  $\text{TiAl}_3$  intermetallic formation in the field of surface contact of solid titanium with liquid aluminium [14]



On the whole, the level of risk of degradation of the performance of titanium-aluminium braze-welded joint is quite sensitive to variation of the technological parameters of welding. Therefore, one of the main tasks in development of the respective technology, is provision of stability of the welding process, which is achieved, for instance, by using the beam welding processes (laser, electron beam) [9].

In the case of braze-welding of extended items non-uniform wetting of titanium surface by liquid aluminium along the length is possible, as a result of, for instance, fluctuations of the thermal impact of the welding heat source. Preliminary aluminizing of the titanium edge is used to provide a uniform contact along the weld and a sound joint [10].

One of the features of titanium is its considerable affinity to oxygen and nitrogen, saturation by which leads to metal embrittlement and, consequently, to lowering of the welded structure performance. Therefore, in welding, it is necessary to envisage the presence of shielding gases (argon) or vacuum [18].

A characteristic process which may influence the quality of the brazed, braze-welded, as well as welded joints, is Rebinder effect [6]. Its presence promotes deformation and fracture of substances of a crystalline structure, as well as spontaneous development of structural changes as a result of reduction of their free surface energy at contact with substances capable of absorption on the interphase. In addition, if the metal, the surface of which is wetted by an adsorption-active substance, is exposed to tensile forces, this may lead to spontaneous development of surface defects and their growing into open cracks.

An essential lowering of the strength of one metal wetted by another metal, often occurs, if their interaction is described by a simple eutectic diagram with low solid-state solubility; a low positive energy of component mixing corresponds to it. However, this phenomenon is usually not observed in systems with a low intensity of component interaction (mutual insolubility), as well as at a very high mutual affinity, particularly, if the components come into the chemical reaction.

The Rebinder effect is characteristic, for instance, for welding stainless steels and copper [4]. As regards the dissimilar pair of titanium-aluminium, an essential difference in the crystalline structure of these metals leads to the conclusion of a weak influence of liquid aluminium on the surface energy of titanium. Therefore, lowering of the strength of the titanium part of the welded joint at its wetting by molten aluminium is improbable.

One of the main problems, arising at operation of dissimilar joints, is the corrosion susceptibility of such structural components in aggressive media [19].

Both titanium and aluminium are characterized by a considerable corrosion resistance because of formation of dense oxide films on their surfaces. However, in the field of dissimilar contact the corrosion fracture can be initiated by galvanic processes (galvanic or

contact corrosion). The degree of corrosion attack in this case depends on the difference of the stationary potentials of the metals forming the contact, and their corrosion characteristics under these conditions.

Experimental investigations of corrosion in synthetic sea water showed that, for instance, at contact with titanium the loss of weight of AMg61 aluminium alloy (Al--(5.5--6.5)Mg--(0.7--1.1)Mn) in stationary water in 245 days is equal to  $2.0 \text{ mg/cm}^2$  (without titanium ---  $0.6 \text{ mg/cm}^2$ ), at relative water velocity of  $10\text{--}12 \text{ m/s}$  ---  $17.5 \text{ mg/cm}^2$  (without titanium ---  $12.1 \text{ mg/cm}^2$ ) in 83 days [20]. The coefficient of acceleration of corrosion fracture of an aluminium alloy in the zone of contact with titanium is equal to 3.30 in the case of stationary sea water, and 1.38 in the case of flowing water. As is seen from these data, in the presence of titanium the corrosion attack in aluminium is markedly intensified, although not in such a pronounced manner.

An essential difference in the strength properties of titanium and aluminium may lead to formation of high tensile residual welding stresses in the zone of dissimilar contact. This, in its turn, leads to an increase of the corrosion phenomena (stress-corrosion) right up to the possible corrosion-induced development of surface crack-like defects [21].

One of the most effective methods of protection of structural elements from an adverse influence of the aggressive medium is deposition of various protective coatings on the surface of the dissimilar part [22]. In addition, in order to lower the level of residual welding stresses the welded joint can be subjected to the appropriate heat treatment.

As the braze-welding process is accompanied by melting of aluminium, at considerable plastic deformations at cooling in the temperature interval of brittleness, hot cracks may develop in the aluminium part of the dissimilar item. The respective optimization of the technological cycle of welding is required to lower the risk of appearance of this kind of undesirable defects. Selection of the aluminium alloy of the dissimilar item and filler material should be determined not only by the requirements to the mechanical and physico-chemical properties, but also maximum hot cracking resistance [23, 24].

One of the possible defects of braze-welded titanium-aluminium joints is presence of oxide films, which are brought into the weld metal from the molten aluminium surface by the convective flows in the liquid metal, and then solidify in the weld metal [25]. Presence of such non-metallic inclusions can have an adverse effect on the welded structure performance at their considerable geometrical dimensions. Therefore, in fusion welding of aluminium it is recommended to ensure an intensive stirring of the liquid metal pool with the purpose of mechanical destruction, refinement and uniform distribution of oxide films in the metal volume [26].

As is seen from the Table, the temperature coefficients of titanium and aluminium differ by several



times. In this case, in welding of extended thin-walled parts of these metals (in particular, sheets or thin plates), the appearance of relative displacement of their edges and additional bending deformations can be anticipated [2, 27]. The residual deformed state can be reduced either due to optimization of the welding process, allowing for the essential deformation of the structure, or due to subsequent thermal or mechanical treatment.

At operation of such welded joints at alternating temperatures (even in the case of uniform heating-cooling) additional stresses can develop in the vicinity of the dissimilar butt as a result of the different kinetics of the deformation field in the aluminium and titanium parts of the item. If the residual welding stresses in the joint are high, such additional load essentially lowers the safe operating life of the structure. In order to lower the influence of this effect on the structure performance, measures should be taken to lower the level of residual welding stresses, in particular, application of different kinds of heat treatment.

1. Wagner, F., Zerner, I., Kreimeyer, M. et al. (2001) Characterization and properties of dissimilar metal combinations of Fe-Al and Ti-Al sheet materials. In: *Proc. of ICALEO* (Orlando, Florida, Sept. 2001). Orlando: LIA, 365-374.
2. Schumacher, J. (2005) *Einfluss von Werkstoff- und Prozessparametern auf laserstrahlgefuegte Mischverbindungen aus Titan und Aluminium*: Diplomarbeit. Bremen: BIAS.
3. Mai, T.A., Spowage, A.C. (2004) Characterization of dissimilar joints in laser welding of steel-kovar, copper-steel and copper-aluminium. *Mater. Sci. and Eng. A.*, **374**, 224-233.
4. Rabkin, D.M., Ryabov, V.R., Gurevich, S.M. (1975) *Welding of dissimilar materials*. Kiev: Tekhnika.
5. Ryabov, V.R. (1983) *Welding of aluminium and its alloys with other metals*. Kiev: Naukova Dumka.
6. Likhtman, V.V., Shchukin, E.D., Rebinder, A.P. (1962) *Physical-chemical mechanics of metals*. Moscow: AN SSSR.
7. Tsvikker, U. (1979) *Titanium and its alloys*. Moscow: Metallurgiya.
8. (1989) *Aluminium: properties and metals science*. Ed. by J.E. Hatch. Moscow: Metallurgiya.
9. Kreimer, M., Vollertsen, F. (2005) Processing titanium-aluminium hybrid joints for aircraft applications. In: *Proc. of 3rd Int. WLT-Conf. on Lasers in Manufacturing* (Munich, June, 2005). Munich, 238-243.
10. Sabokar, V.K., Zamkov, V.N., Kireev, L.S. (1998) Specifics of argon-arc and diffusion welding of titanium to aluminium. *Avtomatich. Svarka*, **1**, 14-17.
11. Pretorius, T., Kreimeyer, M., Zerner, I. et al. (2002) Beeinflussung der Bildung intermetallischer Phasen beim Laserfuegen von Werkstoffkombinationen durch gezielte Nutzung kurzzeitmetallurgischer Effekte. In: *Kurzzeitmetallurgie*. Bremen: BIAS, 23-32.
12. Ziegelheim, J., Hiraki, S., Ohsawa, H. (2007) Diffusion bondability of similar/dissimilar light metal sheets. *J. Mater. Proc. Technol.*, **186**, 87-93.
13. Kahraman, N., Gulenc, B., Findik, F. (2007) Corrosion and mechanical-microstructural aspects of dissimilar joints of Ti-6Al-4V and Al plates. *Int. J. Impact Eng.*, **34**, 1423-1432.
14. (1986) *Metallurgy and technology of welding of titanium and its alloys*. Ed. by V.N. Zamkov. Kiev: Naukova Dumka.
15. Nesterov, A.F., Gordo, V.P., Plyshevsky, M.I. (1986) Specifics of performance of telescopic titanium-aluminium brazed-welded joints. *Svaroch. Proizvodstvo*, **12**, 10-11.
16. Larikov, L.P., Ryabov, V.R., Falchenko, V.M. (1975) *Diffusion processes in solid phase during welding*. Moscow: Mashinostroenie.
17. Dybkov, V.I. (2002) *Reaction diffusion and solid state chemical kinetics*. Kyiv: IPMS.
18. (1998) *Welding handbook: Materials and application*. Ed. by W.R. Oates, A.M. Saitta. Vol. 4, Part 2. Miami: AWS.
19. Verbrugge, M. (2006) Galvanic corrosion over a semi-infinite, planar surface. *Corros. Sci.*, **48**, 3489-3512.
20. (1977) *Titanium alloys in machine-building*. Ed. by G.I. Kapyrin. Leningrad: Mashinostroenie.
21. Joseph, A., Rai, S.K., Jayakumar, T. (2005) Evaluation of residual stresses in dissimilar weld joints. *Int. J. Pressure Vessels and Piping*, **82**, 700-705.
22. (2005) *BIAS Jahresbericht 2004*. Ed. by F. Vollersten, K. Partes. Bremen: BIAS.
23. Prokhorov, N.N. (1976) *Physical processes in metals during welding*. Vol. 2. Moscow: Metallurgiya.
24. Nakata, K., Matsuda, F. (1995) Evaluations of ductility characteristics and cracking susceptibility of Al alloys during welding. *Transact. of JWRI*, **1**, 83-94.
25. Poklyatsky, A.G., Lozovskaya, A.V., Grinyuk, A.A. (2002) Prevention of formation of oxide films in welds in welding Li-containing aluminium alloys. *The Paton Welding J.*, **12**, 39-42.
26. Poklyatsky, A.G. (2001) Peculiarities of formation of oxide film macroinclusions in weld metal of aluminium alloys (Review). *Ibid.*, **3**, 36-38.
27. Makhnenko, V.I., Milenin, A.S., Semyonov, A.P. (2007) Mathematical modeling of thermal-deformation processes in braze-welding of butt joints of titanium-aluminium type. *Ibid.*, **11**, 2.



# ESTIMATION OF VERTICAL DISPLACEMENT OF FLYER METAL PLATES BEFORE CONTACT POINT IN EXPLOSION WELDING

T.Sh. SILCHENKO, S.V. KUZMIN, V.I. LYSAK, A.S. GOROBTSOV and Yu.G. DOLGY

Volgograd State Technical University, Volgograd, Russia

A new methodology for experimental investigation of displacement of the flyer plate sections before contact point in vertical direction in the process of explosion welding is considered. Some results of this displacement evaluation are presented.

**Keywords:** explosion welding, cladding of large-size ingots, strength properties, contact point, detonation front, flyer plate displacement, procedure of displacement evaluation

One of the most efficient practical applications of explosion welding is cladding of large-size billets of different designation, because this method of welding theoretically does not impose any limitations on final dimensions of a billet. Nevertheless, in explosion cladding of large-size plates practically always change of the joint properties is observed over length of the billets being welded, which is manifested in increase of sizes of waves and amount of the molten metal that causes in a number of cases significant reduction of strength properties of a bimetal up to appearance of continuous laminations. In [1–8] judgments are made, which explain these abnormalities. One of the most probable factors, which stipulate manifestation of mentioned effect in the joint zone of long-size plates in explosion welding, is possible vertical displacement of the flyer plate sections, located in front of the contact point under the explosive charge, which still did not detonate. Displacement may take place due

to pressure of the shock-compressed air, located between the plates being welded [1], or action of inertia forces of the shock-wave origin [8, 9], due to which collision geometry of the elements being welded is violated. Both assumptions have right for existence, because they, undoubtedly, make their contribution into violation of the collision geometry. However, till nowadays remains unclear, which of mentioned assumptions is a prevailing one, because systematic experimental investigations of this problem were never carried out.

Purpose of this work is development of methodology for experimental registration and evaluation of vertical displacements of areas of plates before detonation front under conditions of explosion welding.

The developed methodology is based on registration of the instant of shorting of a special sensor-needle on surface of a metal (flyer or target) plate, installed at a certain distance  $\Delta$  from the latter, and it was implemented in the following way (Figure 1). In a selected for investigation section of a package being explosion welded (at a certain distance  $L$  from beginning of the flyer plate) above upper 3 and below lower 4 plates contact displacement sensors 6 were coaxially arranged (conically sharpened copper rods of 2 mm diameter). Distance between the sensors and surfaces of the plates  $\Delta$  was changed in the experiments from 2 to 5 mm. These sensors were switched through the rectangular pulse formation unit (a univibrator, built on logic elements AND–NOT) to inputs of oscilloscopes, starting of which was performed by first contact sensor 5, located at the beginning of the plate, actuated by passing above it detonation front. This allowed synchronizing sweep of oscilloscopes with displacement of the detonation front over surface of the flyer plate. Mean detonation speed  $D$  of the explosive charge 2 was determined by the electrocontact method [10, 11] using sensors 5 and frequency meters. So, knowing value  $D$  and time of actuation (shorting) of sensors 6 it is not difficult to determine for any instant of time position of the detonation front, and having compared by sweep of the oscilloscope time of shorting of sensors 6 — distance before the detonation front,

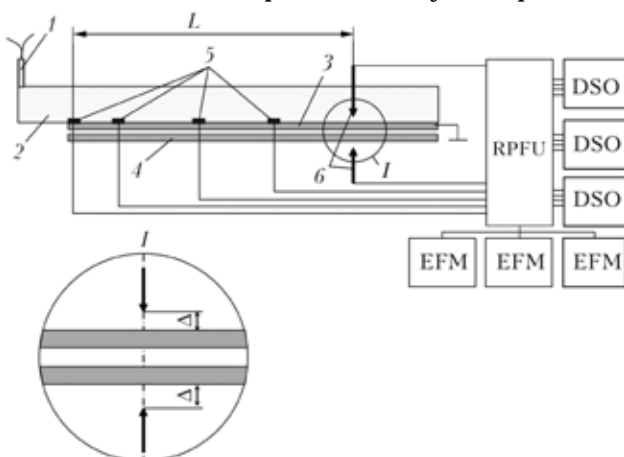


**Figure 1.** Principle scheme of measurement of vertical displacements of plates in explosion welding: 1 — electrical detonator; 2 — explosive charge; 3, 4 — flyer and target plates, respectively; 5 — electric contact sensors; 6 — contact sensors of displacement; RPFU — rectangular pulse formation unit; DSO — digital storing oscilloscope (C9-8, GFDD-820C); EFM — ChZ-63 electronic frequency meter



within which sections of the package plates being welded displace vertically (at value  $\Delta$ ).

For obviousness registration equipment was tuned in such way that shorting of the contact displacement sensors was imaged on the oscilloscope screens in the form of respective pulses, in case of actuation of the upper sensor  $\bar{I}$  -like signal in case of actuation of lower sensor  $\text{---}$  U-like signal appeared on the screen (Figure 2).

Position of the detonation front at the instance of actuation (shorting) of the vertical displacement sensors was determined by the oscillogram proceeding from the following reasons (Figure 3). During passage of the detonation front over explosive charge along the flyer plate contact sensors 1 and 1' are sequentially actuated, rectangular pulse of the first of which (Figure 3, 2) launches sweep of the oscilloscope and simultaneously the frequency meter, and pulse of the second (Figure 3, 2') stops the latter one, reflecting on it period of sequence of the pulses or, which is the same, time of passage by the detonation front of distance over the charge ( $x_2 - x_1$ ), necessary for determining speed of the explosive detonation  $D^*$ :

$$D = \frac{x_2 - x_1}{t_2 - t_1} \quad (1)$$

Then according to formula

$$x_D = x_2 + (t_p - t_2)D = x_2 + \frac{t_p - t_2}{t_2 - t_1} (x_2 - x_1) \quad (2)$$

position of the detonation front was found relative beginning of the flyer plate. If coordinate  $x_D$  was less than  $x_p$  (position of the sensor-needle installation), this proved that section of the plate (flyer or target one), located at a distance  $S$  before the detonation front, displaced in vertical direction at least at a fixed  $\Delta$  value (see Figure 1). Otherwise ( $x_D = x_p$ ) it was considered that vertical displacement of selected sections did not occur, and upper sensor-needle was actuated at ionization of the gap between the sensor and surface of the flyer plate in the detonation wave reaction zone.

For experimental optimization of the proposed methodology several experiments were performed, conditions of which are presented in the Table.

Experiments Nos. 2-6 were carried out according to parallel scheme of explosion welding and on their basis distances from the detonation front were determined, at which vertical displacement of sections of the flyer and target plates took place, according to formula

$$S = x_p - x_D. \quad (3)$$

In experiments Nos. 7-10 the target plate was absent, and sensors of vertical displacement were installed both above and below the flyer plate, that

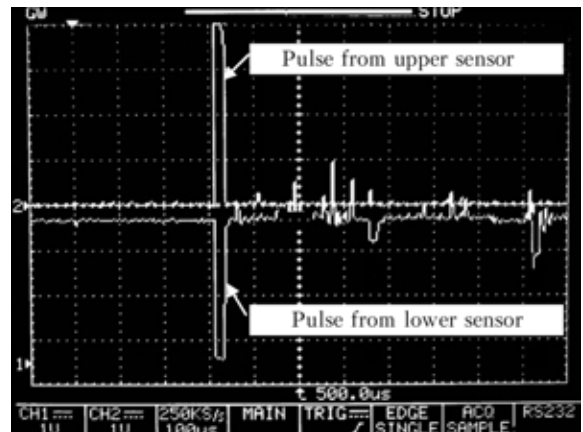


Figure 2. Typical oscillogram obtained in case of simultaneous shorting of upper and lower displacement sensors

allowed registering time of possible displacement of its fixed section not just vertically upwards, but also downwards. In addition, in experiments Nos. 3-6 and 9, 10 vertical distance between surface of the flyer pate and displacement sensors varied from 2 to 5 mm, and in experiments Nos. 3-6 and 10 two lines of sensors were installed  $\text{---}$  at distances 600 and 750 mm from beginning of the flyer plate.

It follows from analysis of the results, obtained in experiments Nos. 1 and 2, that by means of increase of the distance from the point of the explosive charge initiation (respectively 780 and 1010 mm) respective increase of distance  $S$  before the detonation front is observed, within which vertical displacement of sections of the colliding plates is registered. So, in experiment No. 1 distance  $S$  was 36 mm, and in experiment No. 2  $\text{---}$  83.

Similar changes of value  $S$  were noted in experiments Nos. 3 and 5 (see the Table). So, in experiment No. 5, where sufficiently thick and massive plates

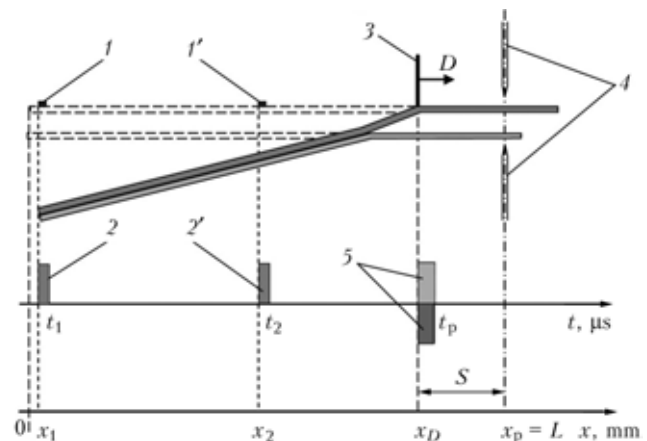


Figure 3. Scheme for determining position of detonation front at instant of actuation of displacement sensors (explosive charge is conditionally not shown): 1, 1'  $\text{---}$  contact sensors; 2, 2'  $\text{---}$  pulses corresponding to time of actuation of contact sensors; 3  $\text{---}$  detonation front; 4  $\text{---}$  displacement sensors; 5  $\text{---}$  pulses on oscillogram corresponding to time of «shorting» of displacement sensors (dash line  $\text{---}$  initial position of plates being welded)

\* At least 4 contact sensors were used in experiments for determining detonation speed mean value.



Conditions of explosive loading of long-size plates in experimental determination of vertical displacement of their sections before contact point

Experiment No.	Material being welded	Size of plates, mm	D, m/s	Setting parameters			S, mm
				h, mm	L, mm	Δ, mm	
1	Steel St.3 12Kh18N10T	2 × 910 × 250 3 × 850 × 200	2940	3	780	2	36
2		3 × 1110 × 150 3 × 1000 × 115	2860	4	1010	2	83
3	Steel St.3 Steel St.3	2 × 800 × 200 9 × 760 × 200	1510	3	600 / 750	2	236 / 386
4			3730			4	236 / 386
						5	236 / 386
5		1540	9 × 800 × 200 9 × 760 × 200			2	151 / 301
						4	151 / 301
6		3740	5			117 / 297	
7	Steel St.3 --	6 × 900 × 120 --	2150	--	880	1	26
8	Steel St.3 --	12 × 900 × 200 --	2180	--	880	1	12
9	Steel St.3 --	9 × 800 × 200 --	1470	--	600 / 750	2	341 / 201
10						Steel St.3 --	9 × 800 × 200 --
	5	51 / 201					
						2	3 / 0
						4	2 / 0
						5	0 / 0

Notes. 1. In numerator values for the flyer plate are given, in denominator --- for the target one. 2. S --- distance between section and detonation front at the instant of actuation of the upper sensor-needle. 3. h --- welding gap.

were used, which were welded at a rather low speed of the contact ( $v_c = D = 1540$  m/s), sensor of the first line ( $L = 600$  mm), installed at the distance  $\Delta = 2$  mm from surface of the flyer plate, registered the contact in  $263.5 \mu s$  after launch of the oscilloscope sweep (the instant of passing by the detonation front of sensor 1 (see Figure 4)), which after recalculation according to formulas (1)--(3) corresponds to  $S \approx$

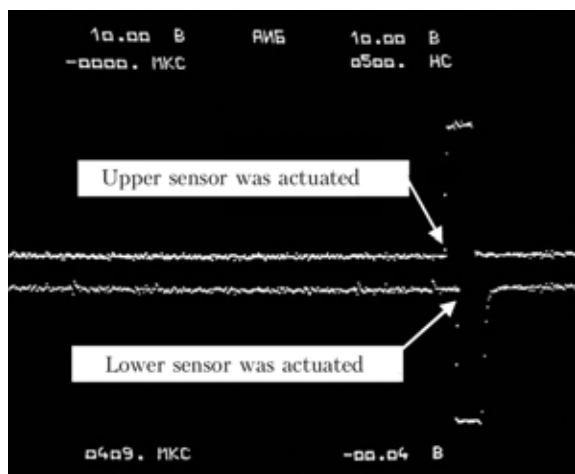


Figure 4. Oscillograms registered in experiment No. 7

$\approx 150$  mm. Sensors of the second line ( $L = 750$  mm), located most closely to surface of the flyer plate ( $\Delta = 2$  mm), registered the same time (in recalculation  $S \approx 300$  mm), which proves practically simultaneous beginning of motion in vertical direction of sections of the plates, located at distance 150 mm from each other.

In experiment No. 3 (see the Table) during throwing of a two-millimeter plate, time registered by sensors of displacement of both lines, reduced down to  $202 \mu s$ . Value  $S$  constituted respectively about 250 and 400 mm.

In case of increase of the detonation speed of a superimposed explosive charge up to  $3730$ -- $3740$  m/s (see the Table, experiments Nos. 4 and 6), vertical displacement of the selected sections of the plates before detonation front was not discovered, whereby time, registered by the displacement sensors, strictly corresponded to the time of the detonation front passage through the plane of their location. Similar situation was observed in case of absence in the experiments of immovable (lower) plate (see the Table, experiment No. 10).

Location of the displacement sensors at different distances  $\Delta$  from surface of the flyer plate (see the



Table, experiments Nos. 3–6, 9 and 10) allowed evaluating speed of displacement in vertical direction of selected sections of the flyer plate. Analysis of the obtained experimental data showed that mean speed of displacement changes depending upon conditions of performance of the experiments from dozens and hundreds meters per second in case of throwing of plates of 9 mm thickness (experiment No. 5) up to thousands meters per second in case of the plate thickness reduction down to 2 mm (experiment No. 3).

An interesting fact of synchronous displacement of sections of the flyer and target plates in opposite directions should be noted, which was registered on the double-beam oscilloscopes in the form of respective pulses (see Figure 2).

Absence in experiments Nos. 7–10 of the target element allowed also evaluating in first approximation period of oscillations of sections of a loaded by the detonation front plate, registered by means of coaxially arranged in relation to each other on its both sides sensors. Difference in time of actuation of the sensors, clearly seen in Figure 4, constituted 8–10  $\mu$ s.

## CONCLUSIONS

1. The developed experimental methodology allowed determining vertical displacement of sections of metal plates, located before the contact point, at their loading by the detonation wave under conditions of explosion welding and evaluating mean speed of this displacement and «delay» of the detonation front.

2. Violation of geometry of mutual arrangement of long-size elements before the detonation front is

one of main factors, which limits final dimensions of the explosion clad ingots.

*The work was fulfilled with support of Federal Agency for Science and Innovations of RF within the framework of state contract No. 02.513.11.3289.*

1. Kudinov, V.M., Koroteev, A.Ya. (1978) *Explosion welding in metallurgy*. Moscow: Metallurgiya.
2. Konon, Yu.A., Pevukhin, L.B., Chudnovsky, A.D. (1987) *Explosion welding*. Ed. by V.M. Kudinov. Moscow: Mashinostroenie.
3. Zakharenko, I.D. (1990) *Explosion welding of metals*. Minsk: Navuka i Tekhnika.
4. Vatnik, L.E., Kriventsov, A.N., Sedykh, V.S. (1974) Some peculiarities of joint formation in explosion welding of sheet bimetal. In: *Transact. on Explosion Welding and Properties of Welded Joints*. Issue 1. Volgograd: VolgPI, 35–45.
5. Gelman, A.S., Chudnovsky, A.D., Tsemakhovich, B.D. et al. (1978) *Explosion cladding of steel*. Moscow: Mashinostroenie.
6. Lysak, V.I., Kuzmin, S.V. (2005) *Explosion welding*. Moscow: Mashinostroenie.
7. Kuzmin, S.V., Lysak, V.I., Dolgy, Yu.G. (2002) Joint formation in explosion welding of large-sized metallic layered composites. *Svaroch. Proizvodstvo*, 5, 48–53.
8. Tarabrin, G.T., Trykov, Yu.P. (1997) Effect of elastic waves on character of plate movement under action of explosion products. In: *Transact. on Metals Science and Material Strength*. Volgograd: VolgPI, 5–13.
9. Gorobtsov, A.S., Silchenko, T.Sh., Kuzmin, S.V. et al. (2006) Mathematical model of interaction of flyer plate with pulsed load in conditions of explosion welding of metals. *Izvestiya Volgograd. Techn. Univ. Series Explosion welding and properties of welded joints*, 24(9), Issue 2, 93–101.
10. Kuzmin, G.E., Paj, V.V., Yakovlev, I.V. (2002) *Experimental-analytical methods in problems of dynamic loading of materials*. Novosibirsk: SO RAN.
11. (1975) *Explosion physics*. Ed. by K.P. Stanyukovich. 2nd ed. Moscow: Nauka.

## TECHNOLOGY OF A-TIG WELDING OF STEELS WITHOUT EDGE PREPARATION WITH A POSSIBLE APPLICATION OF SPECIAL AUTOPRESSING

The offered technology of the argon-arc non-consumable welding using activating fluxes allows producing welded joints of straight-linear and circumferential butts of pipes with a free formation at thickness of edges being welded up to 10 mm without their edge preparation. It guarantees the increase in productivity of welding jobs and high quality of joints of steels by the characteristics of strength, ductility and toughness.

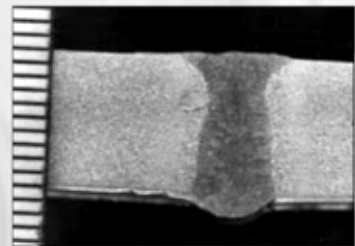
The action of the activating flux, added to the zone of welding, consists in arc contraction, increase in heat concentration and arc pressure on a weld pool, 2.5 times increase in arc penetrability and decrease in weld width as compared with traditional TIG welding at the same current.

Technology eliminates successfully drawbacks of formation of earlier weld without grooving its defective area.

One of the methods of producing weld reinforcement in A-TIG welding is the application of a special autopressing without use of a filler wire.

**Proposals for co-operation.** Development of technology of welding and activating fluxes depending on steel used and design of weldment; delivery of activating flux; rendering technical assistance in mastering the technology of manufacture and repair of separate products and experimental-industrial batches of welded products on the contract base.

Contacts: Prof. Savitsky M.M.  
E-mail: savitsky@paton.kiev.ua



# PREDICTION OF THE SIZE OF GRANULES AND EFFICIENCY OF THEIR PRODUCTION IN CENTRIFUGAL SPRAYING OF ALLOYS

V.I. MAKHNENKO, A.P. ZHUDRA, E.A. VELIKOIVANENKO, A.I. BELY and V.I. DZYKOVICH  
E.O. Paton Electric Welding Institute, NASU, Kiev, Ukraine

The calculation method based on generalisation of the experimental data and results of mathematical modelling is proposed for prediction of the size of granules and efficiency of their production depending upon the centrifugal granulation process parameters.

*Keywords:* boron-containing granules, deposited layer, centrifugal spraying, heat content of detaching droplet, prediction, process productivity, particle size distribution, distribution density

Technologies that provide the composite structure of a deposited layer by adding granules into the filler material, which are capable of imparting the surface layer a certain combination of functional properties, are gaining an increasingly wide acceptance in the last decades for surface cladding. In particular, it is proposed to use dispersed fillers characterised by refractoriness, creep resistance, etc., for the parts operating under conditions of high temperatures. These requirements are met by the granules made from tungsten carbides [1]. However, the shortage of tungsten leads to the necessity to replace it by some other element. For this purpose, study [2] was conducted to investigate a number of compositions based on boron-containing iron granules impregnated with nickel silver MNMTs 60-20-20, as well as alloys based on cobalt (VZK --- Stellite) and nickel (KhN80SR3 --- Colmonoy). Ingots of these alloys, compared with tungsten carbide ingots, have a spraying temperature equal to melting temperature  $T_{\text{melt}} + \text{overheating}$  by 100–150 °C, which is much lower than that of tungsten carbide. This substantially changes the energy parameters of the spraying process, compared with those used for production of tungsten carbide granules [3].

Table 1 gives melting temperatures of the spraying ingots of tungsten carbide (for production of tungsten carbide granules), nickel silver, Stellite (for production of VZK granules) and Colmonoy (for production

of granules containing chromium carbides, boron and silicon), as well as calculation data on the heat content in a unit volume of a detaching droplet,  $\dot{I}_d$ , obtained by using the following relationship:

$$\dot{I}_d = [(\dot{O}_{\text{melt}} + \Delta T_{\text{over}}) \bar{n} + q_l] \gamma, \quad (1)$$

where  $T_{\text{over}}$  is the overheating temperature;  $c$  is the heat capacity;  $q_l$  is the latent heat of melting; and  $\gamma$  is the density.

It can be seen from the data of Table 1 that the heat content of a detaching tungsten carbide droplet is approximately two times as high as that of other alloys. If we take into account the losses of heat in a radiant heat exchange with the environment at a stage of heating, it becomes apparent that the production of granules for cladding alloys Nos. 2–4 (Table 1) is more efficient than that of the tungsten carbide granules.

This circumstance motivates investigations to find alternative materials and technologies for the production of granules. In this case, it is very important to establish the regularities, which can be used as a basis for certain estimations. This study is dedicated to some results of such investigations.

Generalisation of the experimental data on the alloys indicated in Table 1 is based on the mathematical model of spraying taken from study [3], combined with the experimental data generated by using the unit for plasma remelting of a rotating ingot (Figure 1).

Thermal processes occurring in ingot 1 rotating at a high speed, in fixed graphite bushing 2 and pusher

**Table 1.** Thermal-physical properties of alloys investigated

No.	Alloy	$\dot{O}_{\text{melt}}$ , °N	$\gamma$ , g/cm <sup>3</sup>	$q_l$ , J/g	$\bar{n}$ at $\dot{O}_{\text{melt}}$ , J/(g·°N)	$\dot{I}_d$ , J/cm <sup>3</sup>
1	Tungsten carbide	2735	16.88	178.88	0.2621	15783
2	Nickel silver	1230	8.90	291.20	0.4114	7646
3	Stellite	1290	8.42	274.56	0.6864	10633
4	Colmonoy	1070	8.10	328.64	0.6822	9402

Note.  $\Delta T_{\text{over}} = 150$  °C for all variants of the alloys.

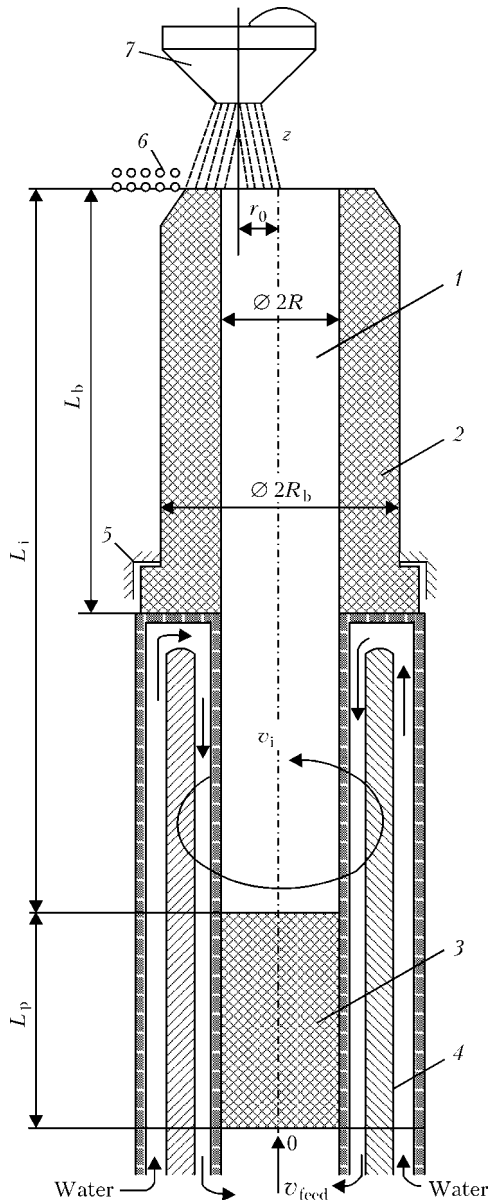


**Figure 1.** Schematic of the unit for production of spherical tungsten carbide particles: 1 — ingot; 2 — graphite bushing; 3 — graphite pusher; 4 — water-cooled ingot shaft; 5 — ingot support; 6 — droplets of spraying ingot; 7 — plasma torch;  $L_i$ ,  $L_b$  and  $L_p$  — lengths of ingot, bushing and pusher, respectively;  $2R_i$  and  $2R_b$  — diameters of ingot and bushing, respectively;  $v_{feed}$  — ingot feed speed

3 (Figure 1) in the system of coordinates  $r, z$ , assuming that contact between the bushing (pusher) and ingot is ideal, can be modelled by a traditional method within the framework of the theory of non-stationary heat conduction under corresponding initial ( $t = 0$ ) and boundary conditions [3].

The intensity of the heat flow from a plasma heat source with power input  $W = 24$  kW (Figure 1) was assumed to be as follows:

$$q(r, t) = \frac{W\eta_s}{K} \pi \exp(-K(r - r_0)^2), \quad (2)$$

where  $\eta_s = 0.55$  is the effective efficiency of heating for variants of alloys Nos. 2–4 (see Table 1) for the case of plasma welding of steel parts;  $K$  is the coeffi-

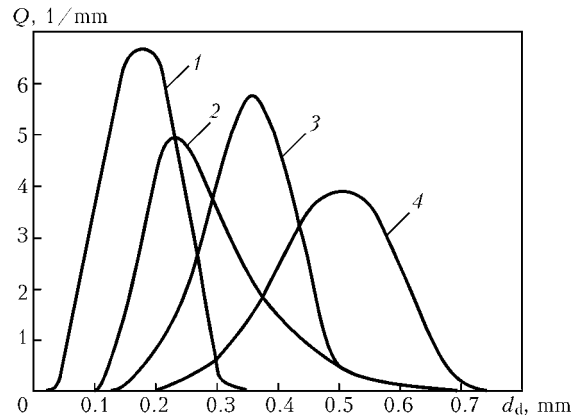


**Figure 2.** Granule distribution density versus ingot rotation speed of 8000 (1), 6000 (2), 4000 (3) and 2000 (4) rpm

cient of concentration of the heat source; and  $r_0$  is the coordinate of the heat source. Thermal-physical properties of the materials used in the calculations are given in Table 2.

The mathematical model used to describe formation and detachment of a droplet was similar to that presented in study [3]. This model is based on the statistical data on distribution density  $Q$  of diameter  $d_d$  of the formed granules (droplets) depending upon ingot rotation speed  $v_i$ .

The curves (Figure 2) were plotted on the basis of experimental data on the frequency of formation of droplets with diameter  $d_d$  and discreteness of  $50 \mu\text{m}$  (Table 3). In this Figure 2, the difference in the calculated values of  $Q$  for alloys given in Table 1 and 2 corresponds to the error of experimental measurements, which is caused by similarity of thermal-physical properties of the alloys.

Equivalent constant diameters  $d_{eq}$  of a group were calculated at the corresponding ingot rotation speeds (see Figure 2), on the basis of which the sizes of elementary volumes were selected for numerical modelling of thermal processes occurring in the zone of the ingot tip being melted. The following relationship was used for this case:

$$d_{eq} = \sqrt[3]{\int_0^{+\infty} d_d^3 \frac{Q(d_d)}{100} dd_d}. \quad (3)$$

The results obtained are given below:

$v_i$ , rpm	2000	4000	6000	8000
$d_{eq}$ , mm	0.48	0.37	0.33	0.19

The sizes of elementary volumes are  $h_r h_z h_\phi = \pi \frac{d_{eq}^3}{6}$ , or  $h_r = h_z = r h_\phi = d_{eq} \sqrt[3]{\pi/6} \approx 0.8d_{eq}$ .

While solving the thermal problem with the above elementary volumes, the readiness of a corresponding volume to the formation of a droplet was traced with time on the basis of temperatures of the volumes in tip layer of the ingot. As shown in study [3], under conditions where dependence of surface tension upon the temperature for the complex alloys considered is

**Table 2.** Thermal-physical properties of materials used for calculations

$\theta, ^\circ\text{N}$	Nickel silver		Stellite		Colmonoy		Graphite
	$\lambda, \text{W}/(\text{m}\cdot^\circ\text{N})$	$c\gamma\cdot 10^{-6}, \text{J}/(\text{m}^3\cdot^\circ\text{N})$	$\lambda, \text{W}/(\text{m}\cdot^\circ\text{N})$	$c\gamma\cdot 10^{-6}, \text{J}/(\text{m}^3\cdot^\circ\text{N})$	$\lambda, \text{W}/(\text{m}\cdot^\circ\text{N})$	$c\gamma\cdot 10^{-6}, \text{J}/(\text{m}^3\cdot^\circ\text{N})$	$c\gamma\cdot 10^{-6}, \text{J}/(\text{m}^3\cdot^\circ\text{N})$
20	23.3	3.5422	21.0	3.722	11.1	3.742	1.760
100	25.6	3.576	21.0	3.806	11.9	4.077	1.760
200	34.3	3.622	21.0	4.016	13.6	4.078	2.155
300	39.9	3.658	23.0	4.193	15.2	4.318	2.509
400	--	3.695	25.0	4.471	16.9	4.335	2.750
500	--	3.731	27.4	4.698	18.5	4.353	2.970
600	--	3.777	29.5	4.968	20.2	4.387	3.063
700	--	3.813	29.5	5.313	21.8	4.464	3.160
800	--	3.849	29.5	5.692	23.5	4.560	3.230
900	--	3.886	29.5	6.130	25.1	4.833	3.270
1000	--	3.922	29.5	6.433	25.3	5.100	3.300
1100	--	3.922	29.5	6.904	2530.0*	5.570	3.320
1200	--	3.922	29.5	6.740	2530.0*	5.570	3.370
1300	3990.0*	3.922	2950.0*	6.740	2530.0*	5.570	3.420

Notes.  $c\gamma$  --- volumetric heat capacity;  $\lambda$  --- thermal conductivity, for graphite  $\lambda = 125 \text{ W}/(\text{m}\cdot^\circ\text{C})$ ; \* --- data obtained by using the effective coefficient of thermal conductivity in direction  $r$ .

**Table 3.** Size distribution of spherical particles, %

$v_i, \text{rpm}$	Size of particles, $\mu\text{m}$											
	50-100	100-150	150-200	200-250	250-300	300-350	350-400	400-450	450-500	500-550	550-600	600-650
2000	--	--	--	2-4	4-8	7-10	16-18	19-25	22-35	28-32	19-22	12-14
4000	--	--	4-6	9-12	11-14	24-27	26-29	11-14	3-4	3-4	2-3	1-2
6000	--	5-8	7-11	23-27	17-19	14-18	9-12	5-7	3-6	2-4	1-2	--
8000	12-13	22-23	28-29	24-25	3-4	3-4	--	--	--	--	--	--

not known to a sufficient degree, the force condition of the formation and growth of a droplet [3] can be approximately replaced by the corresponding temperature one, i.e. it is possible to take the temperature in a surface volume equal to the temperature of detachment of the droplet,  $T_{\text{det}} = T_{\text{melt}} + 150^\circ\text{C}$ , as a condition of the droplet formation. The liquid metal droplet formed during formation time  $\Delta t_f$  shields the corresponding zone of the ingot tip from the heat source for certain delay time  $\Delta t_{\text{del}}$  of the droplet, while during this time the conditions necessary for detachment of the droplet are created, and then the process repeats, i.e. a new droplet is formed during time  $\Delta t_f$  after the removal of shielding, and so on. This tracing allows  $\Delta t_f$  to be determined by solving the boundary value problem, and  $\Delta t_{\text{del}}$  to be found by the iteration method from a condition of agreement between the calculation and experimental data on the process productivity

**Table 4.** Calculated parameters of centrifugal spraying of particles at different ingot rotation speeds

$v_i, \text{rpm}$	$N_d, \text{pcs}$	$d_{\text{eq}}, \text{mm}$	$\Delta t_{\text{del}}, \text{s}$	$\Delta t_f, \text{s}$
2000	10,616	0.48	0.28	0.40
4000	23,589	0.37	0.22	0.30
6000	33,326	0.33	0.16	0.24
8000	172,927	0.19	0.07	0.15

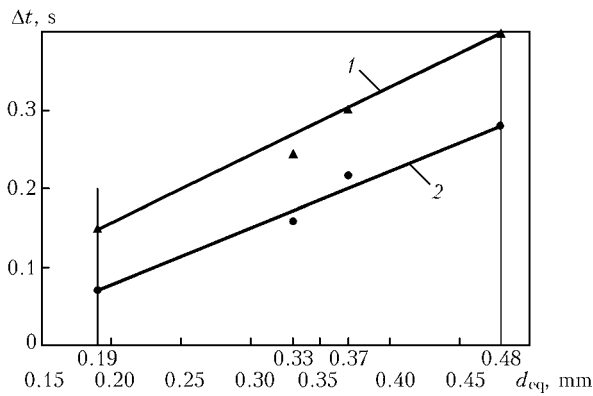
depending upon the speed of translational movement of the ingot along axis  $z$  (see Figure 1). It turned out that  $\Delta t_{\text{del}}$  was roughly equal to extra overheating of the droplet by  $\Delta T_{\text{det}} \approx 50^\circ\text{C}$ .

As a result, the values of  $\Delta t_f$  and  $\Delta t_{\text{del}}$  were determined, which hardly differed for the alloys under consideration (Table 4). Figure 3 shows the dependence of  $\Delta t_f$  and  $\Delta t_{\text{del}}$  upon  $d_{\text{eq}}$  at an experimental value of translational axial movement of the ingot at speed  $v_{\text{feed}} = 1 \text{ mm/s}$ .

The process productivity characterised by quantity  $N_d$  of the droplets formed during 1 s, depending upon the ingot rotation speed, was calculated from the certain parameters of the droplet formation (Table 4). Probability  $P$  of the fact that diameter  $d_d$  of the droplets would be larger than the preset one can be calculated from this quantity of the droplets formed during 1 s by using data shown in Figure 2. An example of this calculation is shown in Figure 4.

Temperature fields in the ingot-graphite bushing-pusher system (see Figure 1) depending upon the rotation speed for variants Nos. 2-4 (see Table 1) were determined as a result of modelling.

To illustrate, Figure 5 shows such data for the quasi-stationary state near the crater of the liquid pool, which were obtained at different speeds of rotation of the spraying ingot of material No. 4 (see



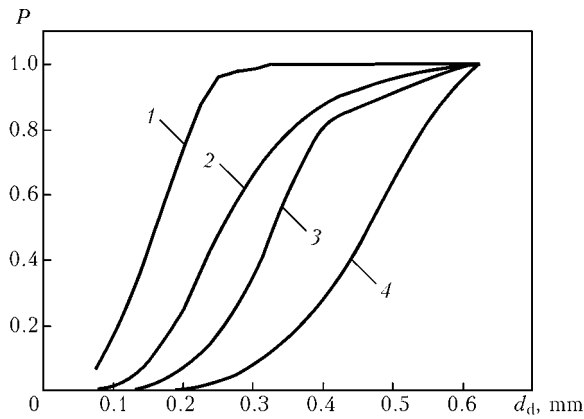
**Figure 3.**  $\Delta t_f$  (1) and  $\Delta t_{del}$  (2) versus  $d_{eq}$  for sprayed alloys Nos. 1–4 at  $W = 24$  kW

Table 1). As evidenced by the similar data for alloys Nos. 1–3 (see Table 1), the temperatures near the crater are approximately proportional to  $T_{melt}$ .

However, parameters of the droplet formation and, accordingly, productivity of this process differ but insignificantly, which is attributable to the sufficiently close values of density (see Table 1) and surface tension of the alloys investigated [4].

As follows from study [1], for the alloys under consideration of high interest is the rate of cooling of a detached droplet.

The corresponding calculation data obtained at a time averaged temperature of a droplet depending upon  $d_d$  are shown in Figure 6. Time reckoning was started from the moment of detachment of the droplet, i.e. allowing for its overheating by about 50 °C during time  $\Delta t_{del}$ . It can be seen from the Figure that different values of droplet formation temperature  $T_d$  and heat



**Figure 4.** Formed droplet diameter  $d_d$  versus ingot rotation speed  $v_i$ : 1–4 — see Figure 2

capacity  $c\gamma$  lead to quite different cycles of cooling of the identical droplets of the alloys considered. That is, the larger the diameter of a droplet, the slower is its cooling rate.

The above investigation results on the given process allow some predictive estimates to be made for the cases where the initial data differ from the considered ones. In particular, an important issue is prediction of the process productivity at a different thermal energy input of the heat source.

The possibility of theoretical prediction of the droplet formation process in the cases where the value of power input  $W$  of plasma heating is other than 24 kW was considered for alloys Nos. 2–4 (see Table 1). In particular, variants with  $W = 11.2, 6.7, 4.5$  and 2.25 kW were studied, the effective efficiency of heating being assumed to be constant ( $\eta_s \approx 0.55$ ), and

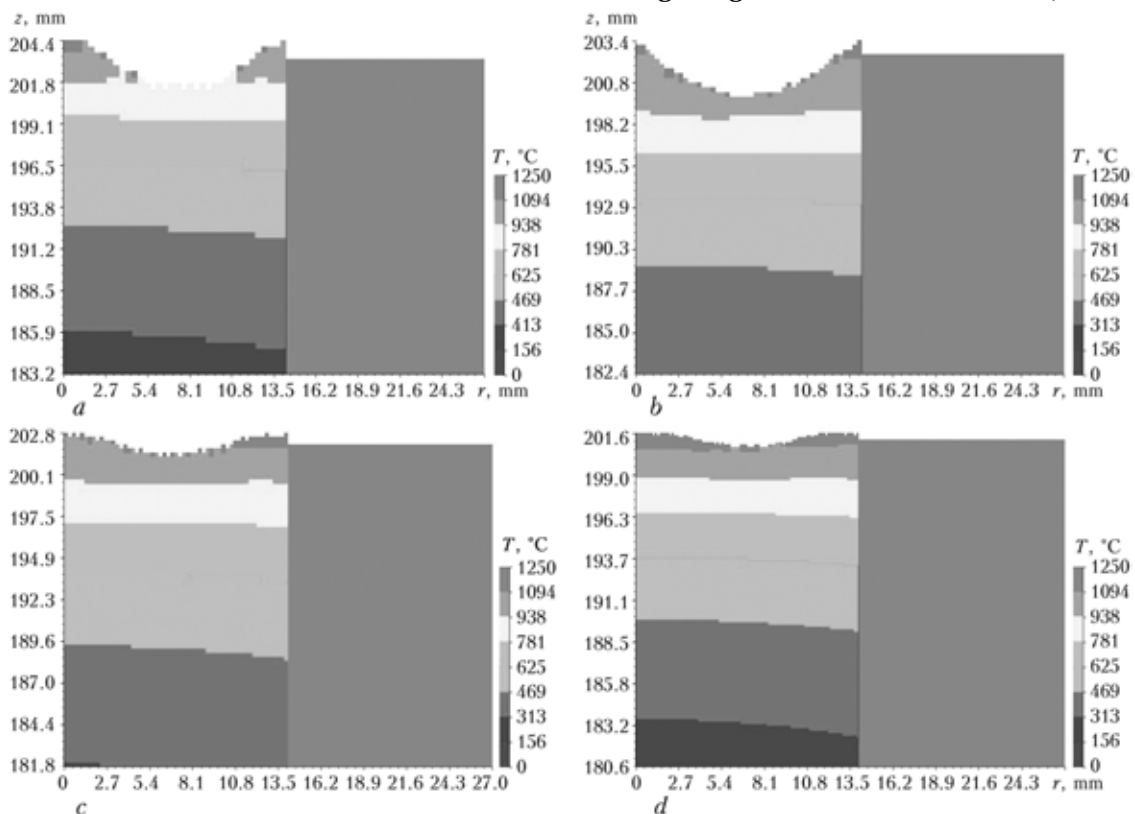


**Figure 5.** Distribution of temperatures and shape of crater of the quasi-stationary state at the spraying ingot tip (alloy No. 4, Table 1) at an ingot rotation speed of 2000 (a), 4000 (b), 6000 (c) and 8000 (d) rpm

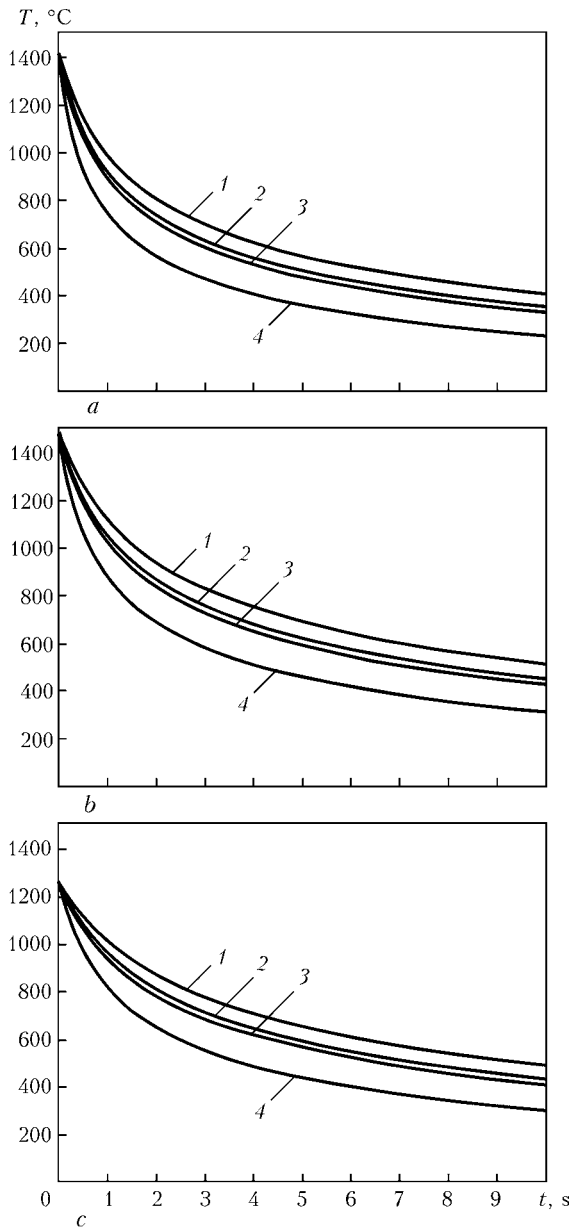


**Figure 6.** Curves of dependence of temperature upon the time of cooling of a droplet of alloy Nos. 2 (a), 3 (b) and 4 (c) (see Table 1): 1 —  $d_d = 0.48$ ; 2 —  $0.37$ ; 3 —  $0.44$ ; 4 —  $0.19$  mm

the coefficient of concentration of the plasma torch heat flow in relationship (2) being assumed to remain unchanged and equal to  $K = 0.015 \text{ l/mm}^2$ . Naturally,  $\eta_s$  and  $k$  may have other values as well, corresponding to the said power of plasma heating. They can be checked in each particular case on the basis of experimental data by using standard procedures common for welding [5]. In this study it is important to show the possibility of predicting the droplet formation process at other heating parameters, e.g. at other values of  $W$ , on the basis of the preset thermal characteristics of the process of plasma heating of a spraying ingot (see Figure 1), by using the data on parameters of the droplet formation at power input  $W = 24 \text{ kW}$ .

This prediction is based on the above-given conditions, such as that formation of a droplet occurs if the temperature of the corresponding surface volumes reaches a certain value and is equal to  $T_{\text{melt}} + \Delta T_f$ . In

a cycle of formation and removal of the droplet from a given surface region, the time of reaching this temperature after removal of a previous droplet is determined by a value of  $\Delta t_f$  obtained as a result of solving the corresponding thermal problem. In this case, it is taken into account that the time cycle of formation and removal of the droplet consists of  $\Delta t_f + \Delta t_{\text{del}}$ , where  $\Delta t_{\text{del}}$  determines the time during which the previous droplet shields a given surface volume from the heat flow. The time of this shielding determined at a known droplet formation process productivity ( $W = 24 \text{ kW}$ ), depending upon the equivalent diameter of the droplet, or quantity of rotations of the ingots, was evaluated by the iteration method (see Table 4 and Figure 3). Naturally, a change in the power input leads to a change in values of both  $\Delta t_f$  and  $\Delta t_{\text{del}}$ .

As found on the basis of solving the thermal problem,  $\Delta t_{\text{del}}$  corresponds approximately to the time of heating of an isolated droplet under the effect of a heat flow of the plasma source,  $q_p(r, t)$ , allowing for the radiant heat transfer into the environment, to a temperature of release of a droplet  $T_r = T_{\text{melt}} + \Delta T_f + \Delta T_r$ . For the variants of alloys Nos. 2–4 (see Table 1),  $\Delta T_r \approx 50\text{--}60 \text{ }^\circ\text{C}$ . The use of this condition allows the  $\Delta t_{\text{del}}$  time to be found very simply for any value of the power input for the ingot rotation, and makes it possible to achieve the appropriate process productivity, which shows up in a certain value of axial feed speed  $v_{\text{feed}}$  of the ingot for a steady-state droplet formation process.

Figure 7 shows the distribution of temperatures during the droplet formation process at an ingot rotation speed of 2000 rpm.

Similar results were obtained at other speeds of rotation of ingots of the Stellite and nickel silver based alloys. Characteristically, decrease in the power input (Figure 7) leads to a substantial increase in the volume of metal near the ingot tip having a temperature close to  $T_{\text{melt}}$ . However, this is accompanied by a marked decrease in the quantity of surface volumes, for which the droplet formation conditions are met, and the values of  $\Delta t_f$  and  $\Delta t_{\text{del}}$  grow, thus leading to a dramatic decrease in the process productivity.

Figure 8 gives an idea of  $\Delta t_f$  and  $\Delta t_{\text{del}}$  depending upon  $d_{\text{eq}}$  (the Colmonoy ingot rotation speed) at  $W = 11.2, 6.7$  and  $4.5 \text{ kW}$ . For a power input of  $2.25 \text{ kW}$ , such data were obtained at an ingot rotation speed of 2000 rpm ( $\Delta t_f \approx 6 \text{ s}$ ,  $\Delta t_{\text{del}} \approx 1.8 \text{ s}$ ,  $v_{\text{feed}} \approx 0.062 \text{ mm/s}$ ). These data are indicative of instability of the droplet formation process.

As a result, the calculation curve of variations in the droplet formation process productivity was plotted for the Colmonoy, Stellite and nickel silver based alloys depending upon power input  $W$  at an ingot rotation speed of 2000–8000 rpm, the curve proving stability of the  $v_{\text{feed}}$  values.

Note another interesting possibility of prediction by means of modelling. Based on the rate of cooling (thermal cycle of cooling) of the droplets sprayed (see Figure 6), it is possible to predict microstructure and some properties of the resulting granules.

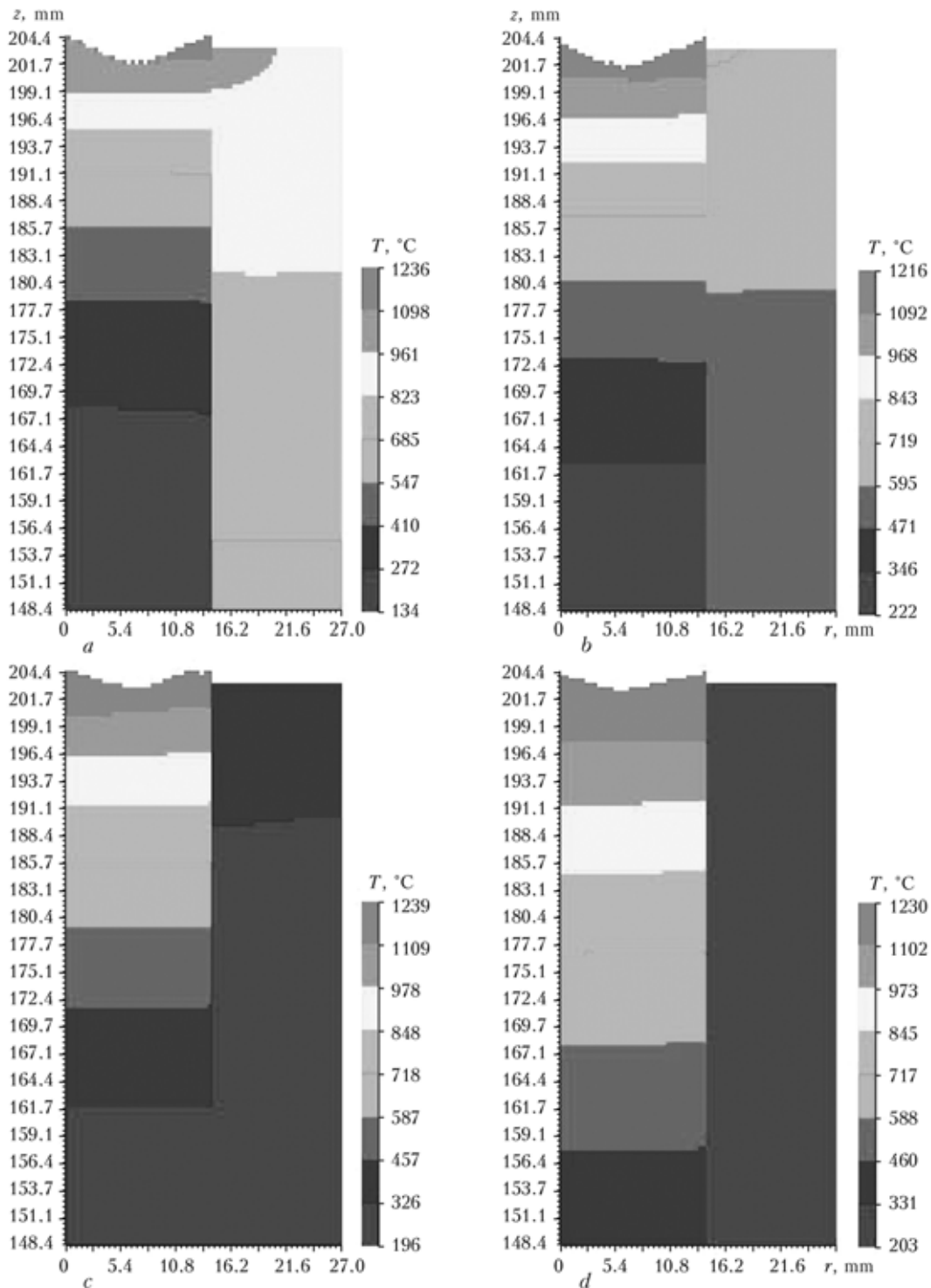


**Figure 7.** Distribution of temperature field in the Colmonoy ingot near the heated tip at  $v_i = 2000$  rpm: *a* —  $W = 11.2$ ; *b* —  $6.7$ ; *c* —  $4.5$ ; *d* —  $2.25$  kW

The procedure for this prediction is well known and based on comparison of the cooling cycle with the corresponding experimental cooling rate–microstructure–properties diagrams. Naturally, this problem is relevant for the case where the droplet metal is sufficiently sensitive to the cooling rate.

Proceeding from the literature data (e.g. [6]), among the three alloys investigated (Nos. 2–4) there is no one particularly sensitive to the cooling rate. Therefore, there is no need to consider this issue in the present study.

Note that on the basis of the curves shown in Figure 6, the initial speed of scattering of the droplets (approximately  $2.8$ – $11.2$  m/s at the above rotation speeds and diameter of the rotating ingot) and the free flight distance being known, it is possible to predict temperature of the droplets at the moment of their collision with a barrier. In particular, if collision occurs in  $0.5$ – $1.0$  s, the temperature of a droplet depending upon its diameter will vary over very wide ranges for the variants of the alloys considered (Table 5).

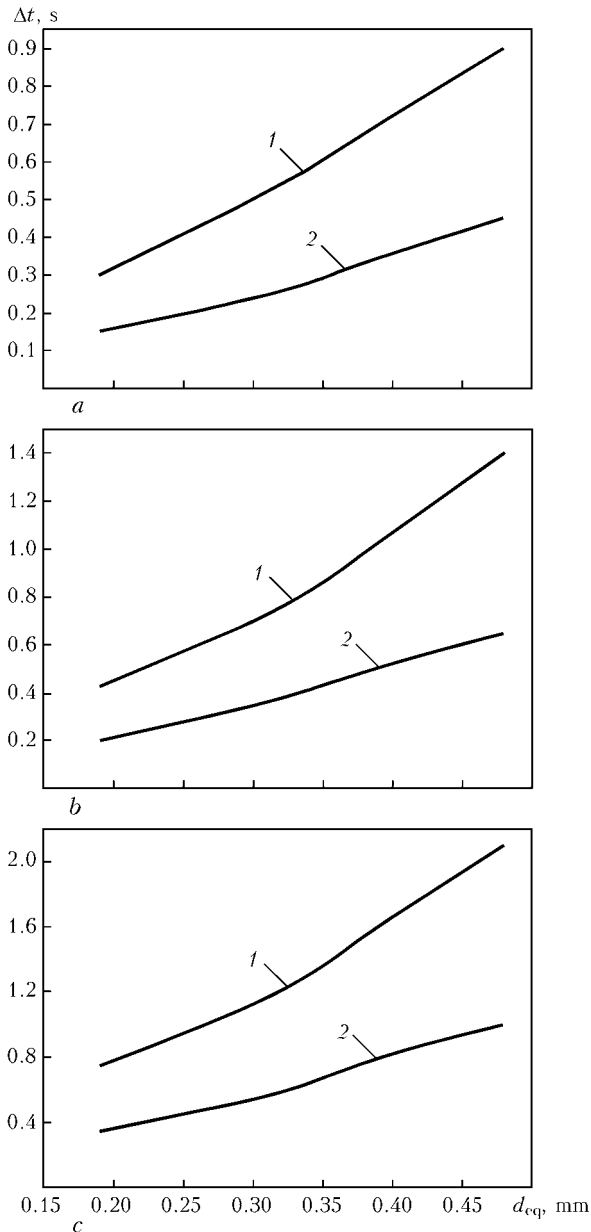


**Figure 8.** Calculated curves of dependence of  $\Delta t_r$  (1) and  $\Delta t_{del}$  (2) upon  $d_{eq}$ , plotted for Colmonoy at  $W = 11.2$  (a),  $6.7$  (b) and  $4.5$  (c) kW

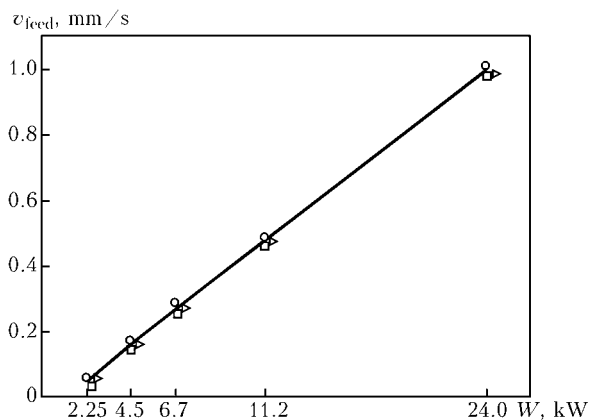


**Figure 9.** Droplet formation process productivity versus power input  $W$  for alloys Nos. 2-4 (see Table 1):  $\circ$  — Colmonoy;  $\square$  — Stellite;  $\Delta$  — nickel silver

**Table 5.** Temperature  $T$  ( $^{\circ}\text{C}$ ) of a droplet at its collision with a barrier after 0.5–1.0 s of the flight

Alloy	$d_d$ , mm			
	0.48	0.37	0.33	0.19
Nickel silver	1150–1000	1100–910	1080–900	910–740
Stellite	1250–1110	1200–1160	1190–1110	1050–890
Colmonoy	1120–1010	1100–960	1090–930	950–810

As follows from Table 5, it is very difficult to provide granules of an ideal spherical shape and large diameter ( $d_d = 0.48$  mm) at limited dimensions of the work chamber, despite a high deformation resistance of the investigated alloys at high temperatures.

Given that torque  $m(v^2/2)$  at the moment of collision of a droplet with a barrier is compensated for by the deformation energy in the droplet and barrier contact zone (here  $m$  is the mass of the droplet equal to  $\frac{\pi d_d^3}{6} \gamma/g$ , where  $g$  is the acceleration of gravity), the condition of elastic collision of the droplet with the barrier can be approximately written down in the following form:

$$\frac{mv^2}{2} < \sigma_{0.2}^d(T) U_d F_d,$$

where  $\sigma_{0.2}^d(T)$  is the yield strength of the droplet material;  $U_d$  is the average displacement on the droplet and barrier contact area; and  $F_d$  is the droplet and barrier contact area.

Deformed volume  $F_d U_d$  at plastic deformations occurring during collision of the droplets is as follows:

$$F_d U_d = \frac{v^2}{2\sigma_{0.2}(T)} \frac{\pi d_d^3}{6} \gamma/g.$$

Designate the relative volume of formation of a droplet as  $\xi = \frac{F_d U_d}{\pi d_d^3 / 6}$ . Then the condition of plastic deformation at collision with the barrier can be represented as follows:

$$v > \left[ \frac{2\xi\sigma_{0.2}(T)}{\gamma/g} \right]^{0.5}.$$

Consider the example where  $\sigma_{0.2}(T) \approx 100$  MPa and  $\gamma/g = 8.9$  [g/cm<sup>3</sup>]/9.8 [m/s<sup>2</sup>] =  $9.1 \cdot 10^{-10}$  [kg/mm<sup>2</sup>/s<sup>2</sup>], which corresponds to alloy No. 2 (see Table 1).

For the above data, this yields

$$v > \left( \frac{20 \cdot 10^{10} [\text{mm}^2]}{9.1 [\text{s}^2]} \right)^{0.5} = 1.48 \sqrt{\xi} \cdot 10^5 [\text{mm/s}].$$

If we assume that the relative volume of deformation of a droplet  $\xi$  is not in excess of 1 %, then  $\xi = 0.01$ , and the  $v$  values should not exceed 14.5 m/s.

It should be noted that the calculated speed of collision of a droplet with a barrier depends to a considerable degree not only upon the above speed of scattering of the droplets, but also upon the forces of gravity.



Assume that the speed of scattering of the droplets has a horizontal direction, and under the effect of the forces of gravity it acquires a vertical direction and is determined by the known relationship

$$v_{\text{vert}} = \sqrt{2gH},$$

(here  $H$  is the vertical path passed by a droplet at its free fall), then speed  $v_{\text{col}}$  of collision of the droplet with the barrier, the normal of which makes angle  $\alpha$  with a horizon, can be determined by the following relationship:

$$v_{\text{col}} = v_{\text{hor}} \sin \alpha + v_{\text{vert}} \cos \alpha.$$

In other words, if  $\alpha = 0$  is a vertical plane, the main role is played by  $v_{\text{hor}}$ , or the speed of scattering of the droplets. If  $\alpha = \pi/2$ , i.e. the collision plane is a horizontal bottom plate, the main role is played by height  $H$  of fall of the droplets. It can be seen from the example considered that for the vertical wall ( $\alpha = 0$ ) the speed of scattering of the droplets is 2.8–11.2 m/s, which is lower than the critical one (14.5 m/s). In the case of a horizontal bottom plate, the ultimate value of  $H$  is equal to  $14.52/2g = 10.7$ , which is quite realistic.

For the case where  $\alpha = \pi/4$

$$v_{\text{col}} = \frac{1}{\sqrt{2}} (v_{\text{hor}} + v_{\text{vert}}) = \frac{v_{\text{hor}}}{\sqrt{2}} + \sqrt{gH}.$$

Hence, the permissible height of fall of the droplet is

$$H = \left( 14.5 - \frac{v_{\text{hor}}}{\sqrt{2}} \right)^2 \frac{1}{g}.$$

The calculation results based on this relationship show the following ultimate values for the example considered:

$v_{\text{hor}}$ , m/s	2.8	5.6	8.4	11.2
$H$ , m	17.4	11.3	7.6	4.4
$t_{\text{flight}}$ , s	1.90	1.50	1.20	0.95

Apparently, decrease in  $\sigma_{0.2}(T)$  toughens the conditions under which there are no marked distortions of the shape of droplets in the case of collision. The value of  $\sigma_{0.2}(T)$  should be selected on the basis of temperature  $T_d$ , and  $T$ — on the basis of droplet flight time  $t_{\text{flight}}$  determined by  $H$ , i.e.

$$t_{\text{flight}} = \sqrt{\frac{2H}{g}}.$$

The above calculation dependence of flight for the given example shows that during the time of flight of a droplet the temperature at its collision with a barrier is lower than the given one (see Table 5), i.e. the

values of  $\sigma_{0.2}(T)$  selected on the basis of temperature determine very conservatively the droplet shape conservation condition.

It should be noted in conclusion that mathematical modelling of the process of formation of granules from alloys Nos. 2–4 (see Table 1), which differ from tungsten carbide in a much lower temperature of spraying of the corresponding ingots, made it possible to reveal the following:

- the melting process productivity can be markedly increased through reducing the time of formation and detachment of droplets at the same power of plasma heating;

- increase in the speed of rotation of a spraying ingot leads to increase in pressure in a liquid layer on the ingot tip, this causing a violation of equilibrium between the forces of surface tension and internal pressure in a droplet at smaller diameters of the latter;

- and as the density and forces of surface tension of the molten base of alloys Nos. 2–4 (see Table 1) differ but insignificantly, according to the experimental data the formed particles are also insignificantly different in their size compositions, which is in good agreement with conclusions of the present study.

According to the data of study [3], the density of tungsten carbide is approximately two times as high as that of alloys Nos. 2–4. However, the surface tension of molten tungsten at temperatures of about 3000 °C is also approximately two times higher than that of molten nickel, copper, manganese and cobalt [4]. Therefore, dependence of the distribution of sizes of the tungsten carbide droplets upon the speed of rotation of the spraying ingot is close to that of the alloys considered in the present study. This also confirms that the density of the granulated material and surface tension of the molten matrix of the spraying ingot determine sizes of the granules at a given speed of rotation of the ingot.

As the value of surface tension of molten metals can be regulated to a certain extent through adding corresponding impurities [4], this factor is worthy of notice for controlling the size distribution.

Based on the investigations performed, it is possible to predict the process of the formation of droplets in the case of limited experimental information.

1. Zhudra, A.P., Litvinenko, A.I. (1989) Some peculiarities of centrifugal granulation of refractory compounds using plasma remelting. *Spets. Elektrometallurgiya*, **67**, 104–105.
2. Spiridonova, N.M., Sukhovaya, E.V., Butenko, V.F. et al. (1993) Structure and properties of boron-containing iron granules for surfacing. *Poroshk. Metallurgiya*, **2**, 45–49.
3. Makhnenko, V.I., Zhudra, A.P., Velikoivanenko, E.A. et al. (2004) Mathematical modelling of the process of manufacture of spherical fused tungsten carbide granules. *The Paton Welding J.*, **2**, 2–8.
4. Nizhenko, V.I., Floka, L.I. (1981) *Surface tension of liquid metals and alloys*: Refer. Book. Moscow: Metallurgiya.
5. Rykalin, N.N. (1951) *Calculations of thermal processes in welding*. Moscow: Mashgiz.
6. (1998) *Welding handbook*. Vol. 4: Materials and applications. Part 2. Miami: AWS.

# EXPERIMENTAL ESTIMATION OF CARRYING CAPACITY OF BUTT WELDED JOINTS OF STRUCTURAL SHAPES IN ELEMENTS OF STRUCTURES SUBJECTED TO LOW-CYCLE LOAD

Yu.D. YAVORSKY<sup>1</sup>, S.I. KUCHUK-YATSENKO<sup>1</sup> and L.N. LOSEV<sup>2</sup>

<sup>1</sup>E.O. Paton Electric Welding Institute, NASU, Kiev, Ukraine

<sup>2</sup>Central Research and Scientific Institute of Construction, Moscow, Russia

Procedures and results of investigation of the carrying capacity of butt welded joints subjected to low-cycle loading, are presented. Recommendations are given on improvement of the carrying capacity of welded joints produced by resistance welding.

*Keywords:* cyclic loading, low-cycle load, carrying capacity, boundary of proportionality, relative deformation, resistance butt welding, flash

It is known [1–3] that serviceability of welded joints is to a great degree determined by their fatigue strength, parameters of which are affected not just by plastic properties of joints, but also by microstructure of the welds. In this connection shape of the welds in resistance welding should exert noticeable influence on fatigue strength of welded joints.

Designing of rolled-welded elements and development in cooperation with the Central R&S Institute of Construction of sheet pilings from them showed that rolled-welded production of steel structures for construction of port hydrotechnical structures, carried out under plant conditions on basis of state-of-the-art technological processes, ensures wide possibilities for development of elements of new shapes and more efficient design solutions of the structures. Such solutions may be found for different depth and foundation soil conditions and operation loads.

For deep water wharf structures long-size piles are used, elements of which it is advisable to weld by resistance flash-butt welding. Sheet pilings are subjected to a specific low-cycle operation load. Data on influence of low-cycle loading on their carrying capacity after a small number of loading cycles are practically absent.

For carrying out tests at PWI five specimens of butt-welded joints of the ShchDS structural shapes (TU 14-2-566–84) for the ShZP sheet piling were made, including:

- «st» and «kst» — standard butt joints made according to TU 35-1772–86;
- «stg» — a similar butt joint, but with unprocessed flash;
- «sm» — a butt joint made with the exceeding permitted standard shift (misalignment) of butted sections of the rolled stock by 2.5 mm;
- «np» — a butt joint with a non-penetrated lock.

Design of the specimens is presented in Figure 1. The butt joints were made by resistance flash-butt welding on the K-190 machine under the following conditions, used in welding of structural shapes with the same cross-section area: time of welding — 120 s; initial voltage — 7 V; flashing time at high voltage — 40 s; low voltage — 4 V; time of the voltage reduction — 30 s; flashing time at low voltage — 40 s; final voltage — 4.8 V; time of the speed increase — 6 s; flashing time at an increased speed — 1.5 s; final flashing speed — 1.5 mm/s; upset — 8 mm; flashing allowance — 28 mm; stick-out — 120 mm; specific pressure of upset — 40 MPa. Under such conditions of welding influence of deformation on impact toughness is manifested to a smaller degree. Moreover, significant influence on plastic properties exerts change of the metal structure in the joint line and adjacent to it areas. At the most unfavorable microstructure, when bend angle of the fibers is 40–60°, impact toughness reduces by 20–30 % [2]. At upset, equal 8 mm, bend angle of the fibers is less than 40°. Fatigue strength in resistance butt welding with these conditions constitutes 95 % in comparison with values for the whole rail [2]. Data on carrying capacity are practically absent.

Task of the tests consisted in estimating change of carrying capacity of the joints, which were preliminarily subjected to cycle loading by variable loads, whereby object of the investigation was tensile carrying capacity of the joints, and it was decided to reproduce cyclic loading that occurred due to fluctuation of the load on the wall from the ShZP sheet piling by loading of the specimens with a variable load according to the transversal bend scheme.

It was necessary to determine if carrying capacity of the joints, subjected to cyclic loading, reduces in comparison with its initial level and to understand influence of defects, existing in joints of the «stg», «sm» and «np» specimens.

For carrying out the tests it was necessary to set number of loading cycles and level of the load, characteristic of operation of sheet pilings in the wharf structures.

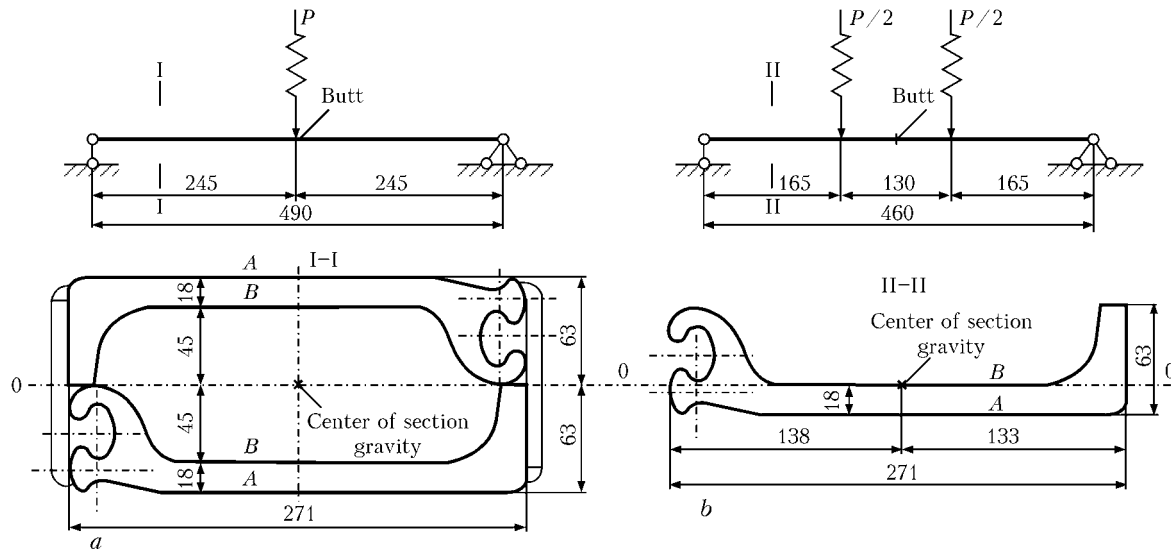


**Figure 1.** Design of specimens and scheme of loading with cyclic load in testing of paired «stg-np» (a) and «st-sm» (b) specimens

According to the norms of design of the wharf structures, sheet pilings are subjected to static load analysis; their endurance test it not performed.

Main loads, which determine stress-strain state of sheet pilings, are pressure of soil, caused by its own weight (a constant load), and weight of stored on the wharf loads and located on it technological equipment (a long-term temporary load). Periods of time, within which increases or reduces this load, is measured by days. A short-term load from ships acts on the structures with the same periodicity.

Wave load has a short period, but for wharf structures, erected as a rule in protected against heaving harbor area, it is significantly lower than constant and long-term temporary load, and its influence on stress-strain state of sheet pilings is insignificant.

Taking into account presented above characteristics of periodicity of variable loads, acting on sheet pilings, calculated duration of the main load change cycle may constitute 2–3 days. As far as near a wharf may be moored and carry out loading-unloading operations simultaneously two-three ships, and a load during handling of each of them is transmitted as well to adjacent areas of the moorage wall, we will in addition reduce thrice calculated duration of the cycle down to 0.6 day. Then within 35-year period of operation of the structure piling profiles in the moorage wall should be subjected up to 22 thou cycles of load changes.

Tested specimens of butt welded joints of the ShchDS profiles were subjected to 25 thou cycles of loading, whereby upper level of mean according to thickness of the shelf value of normal stresses in a joint in each cycle was assumed equal to 0.5 of the calculated by yield strength resistance of steel ( $R_y = 235$  MPa for structural shapes from the VSt3sp steel according to GOST 380–71), and lower one to 0.5 of the upper level. The «kst» specimen was preserved as a reference one, and it was not subjected to cyclic loading. Scheme of loading of the specimens by a cyclic load is presented in Figure 1. For cyclic loading

the specimens were connected pairwise — «stg-np» and «st-sm». Preliminarily standard tail projection of the ShchDS profile was shortened in the specimens down to 63 mm (size equal to height of the lock).

Each pair of the specimens was connected by strips (Figure 1, a) of  $100 \times 100 \times 10$  mm size, installed on ends of the specimens on their side edges and welded over the contour in such way that shear strength of 209 kN be applied to the welds, which corresponds to the load  $P = 686$  kN on a paired specimen. Box section of a paired specimen has the following characteristics: area  $F = 136.3$  cm<sup>2</sup>, central moment of inertia  $J_0 = 3089$  cm<sup>4</sup>, moment of resistance  $W = 490$  cm<sup>3</sup>.

Cyclic loading of welded specimens was performed on the «Shopper 200» (TsDM-200-Pu) test machine at pulsation frequency 300 cycle/min.

The «stg-np» paired specimen was subjected to 25 thou cycles of variable load with the «stg» specimen located in the stretched zone and the «np» specimen in the compressed zone of box section, and then to 25 thou cycles more after turn over of the specimen for the purpose of changing positions of «stg» and «np».

Limit changes of the load on the «stg-np» specimen and calculated normal stresses in the butts (see Figure 1) were as follows:  $P = 294$ –588 kN, level of normal stresses in joint A was 73–147 MPa; in joint B — 52–105. After termination of cyclic loading the «stg» and «np» specimens were disconnected by cutting of the strips.

In the «st-sm» paired specimen due to defect, shear of the fastening weld of one of the connection strips occurred at load on the specimen 619 kN, which caused residual deformation of the tail projection of the «sm» specimen and compelled to pass over for testing of the «st» and «sm» specimens by cyclic load to the scheme of their separate loading (see Figure 1, b). Characteristics of the trough section of a single specimen are as follows: area  $F = 68.15$  cm<sup>2</sup>, central moment of inertia  $J_0 = 165$  cm<sup>4</sup>, moment of resistance of the stretched zone  $W = 91.5$  cm<sup>3</sup>.

Cyclic loading of the «st» and «sm» single specimens was carried out on the «MUP-100» test machine at pulsation frequency 450 cycle/min.

To each specimen (see Figure 1) 25 thou cycles of variable load were applied with the following parameters of loading:  $P = 127\text{--}255$  kN; level of normal stresses in butt A equaled 115–230 MPa, in butt B it was constant — 0 MPa.

After testing by the cyclic load carrying capacity of the specimens was determined at tension in direction of the normal to the butt plane. The reference «kst» specimen was also subjected to tension test. The specimens were extended on the «Shopper 200» test machine applying slowly increasing load at speed of displacement of the movable holding device 0.002–0.005 mm/s, and «force–strain» diagrams were built. Deformations were measured in direction of the extension force, on the longitudinal axis line of the speci-

mens both on external surface of the shelf and on side of the trough using mechanical strain gages and indicators of displacement, installed on the 200 mm base symmetrically in relation to the butt weld. Registered by the strain measuring instrument real and conditional manifestation of yield of the steel in the butt zone was used as criterion of exhaustion by a specimen of its carrying capacity. Value of the load, corresponding to occurrence of this phase of stress-strain state of a specimen, was determined by the extension diagram.

Extension of the specimens was continued up to their failure. Obtained values of carrying capacity of the specimens that passed cyclic load tests were compared with carrying capacity of the reference «kst» specimen for the purpose of estimating aftereffects of a specific low-cycle loading. Influence of defects, present in the butt joints, as well as such peculiarities of

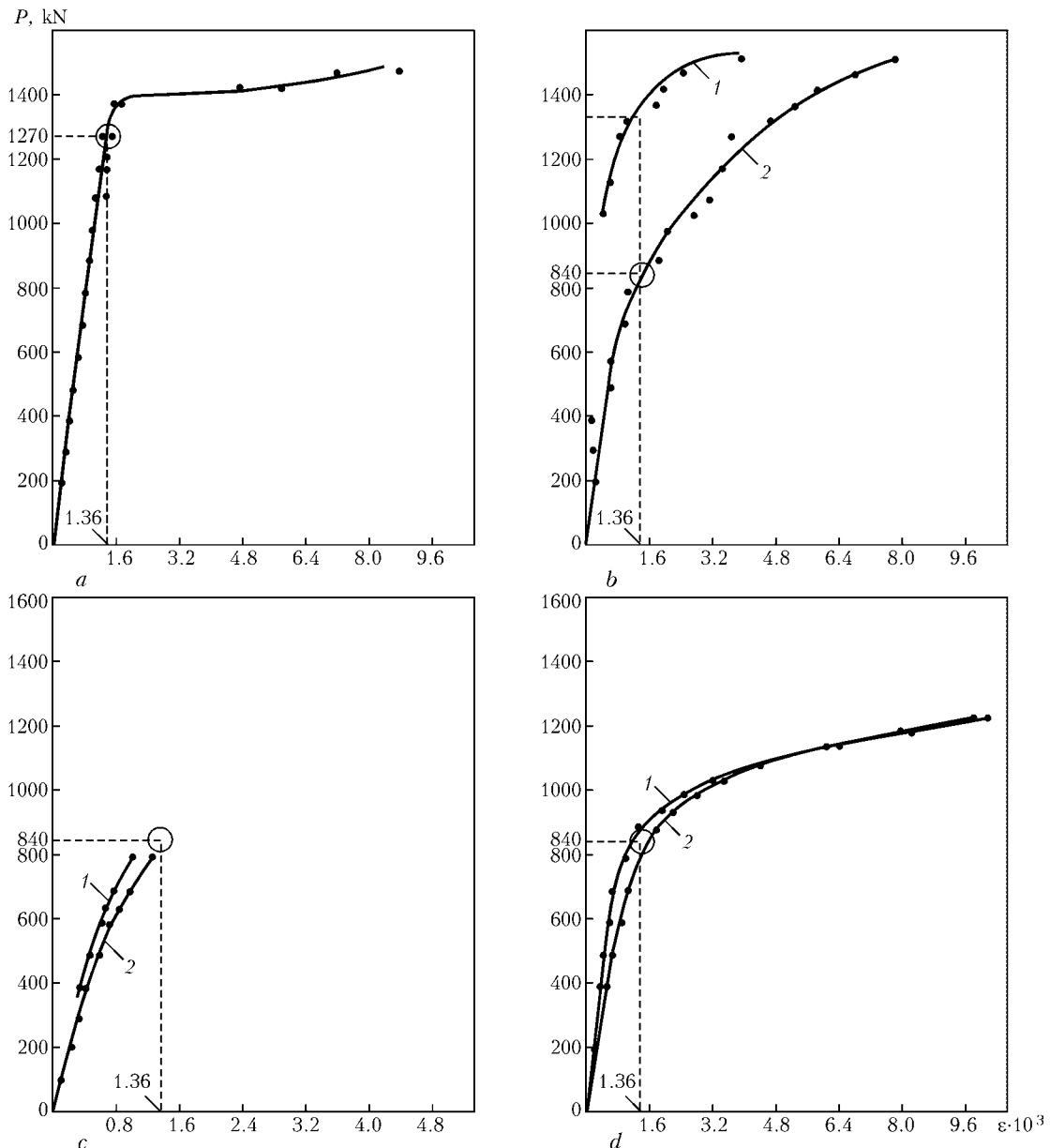


**Figure 2.** Diagram of extension of butt joint specimens: a — «kst»; b — «st»; c — «stg»; d — «np»; 1 — shelf surface on side of lock B; 2 — rear surface of shelf A. Base of strain measurement is 189 (a, b, d) and 200 (c) mm, means of measurement — indicator of displacements (1 div — 0.01 mm) (a, b, d) and mechanical strain gage (1 div — 0.001 mm) (c)

state of the specimens as form of the failure, formation of cracks, big plastic deformations, detected in the tests, are presented in Figures 2 and 3. Applied to a specimen limit load, at which it remained undistorted, was 1695 (for the «kst» specimen) and 1671 kN (for the «st» specimen). The «stg» specimen failed at the load 1499 kN (breakage of a portion of the shelf with the tail projection), the «np» specimen failed at the load 1519 kN (breakage of the specimen shelf near end-lap weld of the tail cover plate). By time of failure crack opening at its root achieved 15 mm. As one can see from dependences, presented in Figure 2, *b*, the load, at which relative deformation  $\varepsilon = 1.36$ , is 840 kN. At the same time on surface of the shelf on side of the lock at the same relative deformation the load constitutes, approximately, 1300 kN, i.e. corresponds to the data, obtained on the reference «kst» specimen. This proves that at a limited number of repeated loading cycles, which exceed elasticity limits, redistribution of stresses-strains may cause attenuation of the plastic deformation accumulation, i.e. adaptability [4].

For the purpose of ensuring uninterrupted operation of port hydraulic engineering structures over whole term of their service, preventing possible damages and deformations, determining volumes, terms, and methods of necessary repairs, and estimating working life of separate structural components constant technical supervision is carried out. For carrying out complex investigations it is necessary to collect maximal possible volume of information about the structure and familiarize oneself with results of full-scale investigations of separate specimens, carried out at least three years before the check, and results of observations over the structure from the time of its construction.

Maximal allowable displacement, determined by the data obtained on the «st» specimen ( $\varepsilon = 1.36$ ), corresponds to 1270 kN load. Limit loads, by which maximal static carrying capacity is determined, may correspond to maximal allowable displacements, failure, or exhaustion of carrying capacity of the section, when at small increase of the load sharply increases deformation, which may limit static carrying capacity. Limit loads are determined in this case by conditions of complete transition of the specimen section into plastic state. Calculation that takes into account exhaustion of static carrying capacity because of a strain is widely used for many construction structures. As one can see from Figure 2, *b*, for the «st» specimen two loads of 840 and 1300 kN correspond to maximal allowable displacement  $\varepsilon = 1.36$ . If maximal allowable values of deformation are higher than value of deformations, corresponding to achievement of yield strength, this means increase of carrying capacity due to elastic-plastic redistribution of stresses in the process of deformation (adaptability).

If it is difficult to establish, which limitation connected with displacement or failure, provides smaller

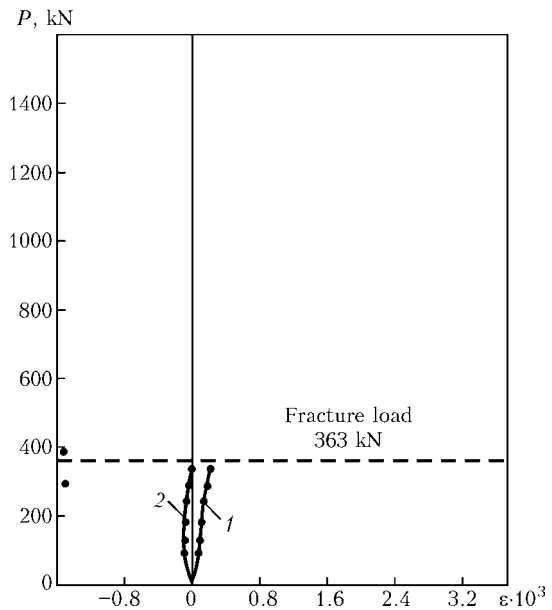


**Figure 3.** Diagram of «sm» specimen extension (brittle failure, after cyclic loading specimen got residual sag 30 mm). Base of strain measurement is 200 mm, means of measurement — mechanical strain gage; 1, 2 — the same as in Figure 2

safety margin, one has to determine two safety margins and chose for calculation the smaller one that corresponds to the load 840 kN. Ratio of the parameters 420/1270 kN, obtained on the «kst» and «st» specimens, constitutes approximately 30 %.

Data, obtained in tests of the «stg» specimen, prove that flash is initiator of the carrying capacity reduction, and it should be removed in welded joints, and degree of influence of the non-penetrated lock in the sheet piling (the «np» specimen) shows dependence of a crack initiation upon the place of its location. Such defect is initiator of an extended crack. If width of a crack is more than 1 mm, a mark is put for observing process of its development. The most serious defect in the resistance butt welding is deviation of alignment of the butts, which is proved by the data presented in Figure 3 (the «sm» specimen).

So, low-cycle load reduces carrying capacity of the Z sheet pilings, walls of which are welded by resistance flash-butt welding, by approximately 30 %. Flash in the joints, produced by resistance butt welding, may be initiator of their carrying capacity reduction, and it should be removed. Non-penetrated lock in chords of the Z sheet pilings stipulates development of extended cracks. Violation of alignment in resistance butt welding is inadmissible defect.

1. Asnis, A.E., Kuchuk-Yatsenko, S.I. (1960) Statistic and vibration strength of rolling large-section joints made by butt welding. *Avtomatich. Svarka*, **12**, 14–21.
2. Kuchuk-Yatsenko, S.I., Lebedev, V.K. (1975) *Continuous flash-butt welding*. Kiev: Naukova Dumka.
3. Trufiyakov, V.I. (1973) *Fatigue of welded joints*. Kiev: Naukova Dumka.
4. Makutov, N.A. (1971) *Statistic principles of low-cycle fracture*. Moscow: Strojizdat.

# HYPERBARIC DRY UNDERWATER WELDING (Review)

V. Ya. KONONENKO

SE «Ekotekhnologiya», Kiev, Ukraine

World experience in the field of technologies of underwater welding in a dry chamber is considered. Features of their application in assembly, manufacturing and repair of critical structures and constructions are shown.

*Keywords:* arc welding, dry underwater welding, habitable chambers, coated electrodes, flux-cored wires, mechanical properties of the joints

At present there are more than 4000 off-shore platforms in the open sea all over the world, which are used for oil and gas extraction from the sea bottom. Most of these metal structures are operating now and have been in service for more than 20 years. Oil and gas transportation to the consumption regions is usually performed along underwater pipelines, the length of which is equal to several tens of thousand kilometers. Wharfage with a large number of metal elements, which are in the water, has been constructed, and tens of thousands of ships and vessels are under construction. In the underwater part of these constructions defects can develop, which disturb their watertightness. Appearance of these defects can be caused by violation of the technology during mounting work performance, development of corrosion processes, damage under the impact of natural forces, combat damage, as well as possible errors in design and construction. High quality of welding operations is required for construction and restoration of the performance of these facilities.

Repair of the hulls of ships and vessels is usually performed in the dry docks or on slipways by optimized technologies. Difficulties are encountered, when it is impossible to move the metal structures into the dry dock, where the repair restoration work is performed, or in the absence of the docks in the regions. In these cases repair is performed with underwater welding application. Today there exist three main processes of performance of underwater welding operations:

- wet welding under the conditions of direct contact with the water is performed under the pressure, which depends on the depth of welding operations performance;
- hyperbaric welding inside a dry habitable chamber, mounted around the elements being welded, which is performed under pressure, the value of which depends on the depth;
- welding inside a caisson under dry conditions at atmospheric pressure using a metal structure immersed into the water, which is connected by a sealed joint to the element being repaired and inside which a welder works.

The current status and features of development of wet underwater welding in ex-USSR and CIS countries are described in sufficient detail in a number of publications [1–7]. Welding inside a caisson practically does not differ in any way from welding under the regular conditions on dry land. This paper deals with the world experience of application of hyperbaric underwater welding.

This welding process began developing in the world starting from 1960s, when with continuous widening of the production of hydrocarbon raw materials from the sea bottom and mounting of installations for their production, the designers started using materials with higher mechanical properties. Requirements to welded joint quality were increased, accordingly. In 1967 Taylor Diving and Salvage Company, USA, for the first time in the world applied for dry underwater welding a simple chamber with an open bottom, mounted in the site of the future pipe joint [8, 9]. The chamber was put on the pipeline using side cut-outs, which enclosed the pipeline and were sealed by special seals. Water was ousted from the welding chamber by inert gas and welder-diver performed welding, staying inside the gas bubble formed in the chamber. The main feature of application of this process consists in elimination of contact of the reaction zone of welding and metal being welded with the water, which provides essential advantages for producing an equivalent welded joint irrespective of the external conditions and depth of work performance. Positive results obtained using this technology, allowed upgrading the chamber, fitting it by hydraulic systems and other necessary equipment.

At present most of the work in dry chambers is performed at repair of underwater pipelines [9–12]. The chambers are custom designed and made. Such a chamber of 8 to 20 t weight usually is part of the ship diving complex. In addition to it, the complex also includes hydraulic hoists and centering skids, which are necessary for pipe displacement in the vertical and horizontal planes at their fixing and sealing in the chamber end faces. The chambers are fitted with a set of sealing elements for different pipe diameters, a set of equipment for pipe dressing, cutting and fitting, a sealed all-purpose arc power source for nonconsumable and consumable electrode welding, sealed containers for storage of the tools and devices, electric tools, equipment for post-weld dressing, control and heat-treatment of the welded joints. The chamber is also fitted with a system of smoke removal, fire extinguish-



ing, monitoring the gas mixture composition and hydraulic system of fixation and displacement of the repaired pipe to short distances in the case of its alignment at mounting. The chamber upper part has a man-hole, to which the diving-bell is abutted. The welders-divers can move from the bell directly into the chamber. During mounting, when the chamber is filled with water, the work is performed in the diving suit. After completion of the mounting work, the welder is working without the diver's gear. If required, he puts on the breathing mask connected to a system of gas supply to the diving-bell. Technology of underwater pipeline repair optimized on hundreds of objects [10–12], can be divided into the following stages:

- washout and cleaning of pipeline surface to the distance of 5–10 m on both sides of the defective area;
- mounting hydraulic hoisters and pipeline lifting into a position allowing the chamber to be mounted on it;
- mounting onto the repaired section and sealing the pipe inlets into the chamber;
- water ousting by feeding the gas mixture, the composition of which is selected depending on the depth;
- cutting out a defective section with formation of two edges;
- mounting the sealing elements in the pipe;
- final cleaning of the pipeline inner and outer surfaces;
- fitting the repaired section to the dimensions of the welded-in coil;
- mounting the welded-in coil on the repaired section and its tack-welding;
- making the root welds;
- groove filling by multipass weld;
- heat treatment of welded joints by the present cycle;
- nondestructive testing of welded joints;
- hydraulic insulation of the repaired section;
- dismantling the chamber and the hoisting devices;
- washing the repaired pipeline section.

It should be noted that all the underwater operations are conducted under the supervision of specially trained engineers and technicians. They are constantly following the physical condition of divers-welders and humidity of the gas mixture, and also monitor all the electric parameters of the arc process. Welding operations under the water are performed by specialists who have been trained for many months.

Dry underwater welding of metal structures with a developed surface involves considerable difficulties [8, 12]. Its implementation requires designing and manufacturing the chamber to be used for repair of just one element, which requires considerable labour consumption. Modern computer technologies and meal-working equipment allow manufacturing a specialized chamber in three to four work days. Such a chamber, as a rule, has minimum internal fitting. Used together with it is an all-purpose immersible power source allowing performance of coated-electrode, TIG

and MIG/MAG welding, as well as welded joint heat treatment by the specified program. The power source is placed outside the chamber. Welding consumables and equipment for work performance are supplied inside the chamber in sealed boxes. The chamber upper part can accommodate a transition compartment for its abutting to the diving-bell. Operating conditions of the welder-diver in such chambers are worse than in chambers used for pipeline welding. The technology of repair work performance depends on the depth, design of the repaired component, technological capabilities of the company, remoteness of the repaired object from the sites, where such chambers are manufactured, and customer requirements to the terms of work performance.

Preparation of the repaired surface (cleaning from biofouling) is performed with application of mechanical brushes or by a high-pressure water jets. Preparation of the tubular elements in the water is performed with application of oxy-arc or exothermal cutting. Surface preparation for welding (edge preparation) is performed by a metal cutting tool with a hydraulic or electric drive. Sealing the tubular elements, similar to pipeline welding, is performed by sealants mounted inside the pipes.

In order to perform repair work on flat structures such as the board of a ship or floating dock, specialized chambers are developed, into which all the object section to be repaired is placed [8]. Mounting and sealing of such a chamber requires considerable labour consumption. Repair technology is the same as when specialized put-on chambers are used.

Investigations in the field of technologies of hyperbaric welding conducted in the leading institutes and research centers [13], are aimed at increasing the effectiveness of the technologies of coated electrode, MIG/MAG and TIG welding using solid and flux-cored wires, assessment of the influence of pressure, gas medium composition and shielding gas flow rate on transfer, oxidation of alloying elements, structure and mechanical properties of the weld metal in welding. In view of the fact that the new oil and gas fields in the Mexican Bay and other regions are located at more than 500 m depth, the work on development of remotely controlled automatic welding systems was expedited. Automatic systems developed so far, allow ensuring the required mechanical properties of the joints with a high repeatability of technical characteristics when using TIG and MIG/MAG technologies at down to 450 m depth [14–16].

Carbon and low-alloyed steels with aluminium, titanium, boron and other microalloying are applied for construction of off-shore platforms and underwater pipelines. Such steels are prone to formation of hardening structures in the HAZ metal under the conditions of hyperbaric welding, when a considerable heat removal into the environment of the chamber filled with helium-oxygen mixture is observed. In order to lower the probability of cold cracking in the HAZ metal the welded structures are heated up to the temperature of 120 °C.



At hyperbaric welding it is necessary to distinguish between two types of environments — welding chamber environment and environment (gas mixture) fed to the welder for breathing. In connection with the fact that the welding process results in contamination of the environment (chamber atmosphere) the welder must wear a mask and have an independent breathing environment. This is also important considering that realization of the welding process requires performance of preparatory work. In addition, there is also the risk of the welder accidentally inhaling the gas atmosphere of the chamber, so that it should be suitable for breathing [12].

In the composition of gases filling the chamber, the content of nitrogen is strictly controlled, as nitrogen penetration in to the arcing zone leads to formation of nitrogen oxides, as well as the content of argon, as both the gases have a strong narcotic effect on the human body. In this respect helium (even though it is very expensive) is a gas acceptable for breathing of the welder-diver at different depths. The welder needs oxygen for breathing, the concentration of which in the chamber atmosphere is specified proceeding from the biological need and fire safety requirements [11, 12].

At penetration of the gas breathed out by the welder into the chamber, the concentration of oxygen and other gases can exceed the admissible limits. The gas mixture, exhaled by the welder, is either taken out of the chamber, or a system of atmosphere regeneration is installed in the chamber, which controls the concentration of oxygen and other gases.

The welding process is characterized by evolution of a whole number of compounds into the atmosphere, such as  $\text{NO}_2$ ,  $\text{O}_3$ ,  $\text{CO}$ ,  $\text{CO}_2$ , and different kinds of aerosols. The concentration of these compounds in the chamber atmosphere should not exceed the admissible value threshold. In addition to the atmosphere composition, such parameters as humidity and temperature are controlled inside the chamber. Increased humidity of the chamber atmosphere may lead to development of problems related to saturation of the consumable materials with moisture and moisture penetration into the arcing zone. Temperature control inside the chamber also has an essential influence on the welder's health in view of the fact that during breathing at higher pressure helium removes much more heat from the human body than nitrogen does.

Essential problems in welding under the hyperbaric conditions result from increased pressure and high heat-conductivity of the gas medium. It is established that irrespective of the used technologies the arc process becomes destabilized at increase of the depth of work performance [17, 18]. The point of intersection of the inherent characteristic of the welding arc power source and characteristic curve of the arc under the hyperbaric conditions changes its position relative to its position under the normal conditions. The arc under these conditions is characterized by a high voltage drop gradient and high degree of constriction and arc excitation becomes more difficult.

Increased pressure has an essential influence on the deposited metal composition [19]. As was noted above, under the conditions of increased pressure the arc column is constricted, the area of the anode and cathode spots becomes smaller, which, in its turn, increases their temperature. Arc constriction and increase of its temperature influences the geometry and other characteristics of the weld pool (with pressure increase the penetration depth and reinforcement height increase, weld width decreases, molten metal surface tension and its mobility change, and the degree of gas adsorption also increases). Arc temperature increase promotes an intensive loss of the alloying elements from the weld metal. Silicon and manganese concentration in the weld decreases and the quantity of their oxides in the slag crust increases.

In TIG and MIG/MAG technologies different gas combinations ( $\text{He}$ ,  $\text{He}/\text{CO}_2$ ,  $\text{He}/\text{O}_2$  in different proportions, etc.) are used for arcing zone protection. The optimum quantity of gas fed for the arcing zone protection in welding under the hyperbaric conditions is equal to approximately 10 l/min [13]. The nature of outflow of the shielding gas from the torch nozzle has an essential influence on the impact toughness of the welded joint metal. The turbulent gas flow, similar to welding in air, lowers the impact toughness of the weld metal.

*Technology of coated-electrode welding* under the hyperbaric conditions is applied for welding the root welds, and in a number of cases also for groove filling. Coated electrodes with a basic-type coating are usually applied, the use of which gives rise to a whole number of technical and technological difficulties. As was noted above, with increase of pressure the weld pool fluidity decreases and disturbances due to magnetic blow, increase, the welds become more convex with a steeper weld transition to the base metal, which makes slag removal more complicated. The diver-welder has to use smaller-diameter electrodes compared to electrodes applied under similar conditions in welding in air. The greatest difficulties arise when making multipass fillet welds and the last groove-filling weld. Welding is to be performed by a very short arc. Certain problems arise because of the high hygroscopicity of the electrode basic coating under the conditions of welding in helium-oxygen atmosphere. At 90–98 % humidity in the chamber the time of electrode saturation by water vapours up to the concentration of 0.2 % is 2 to 3 min. Therefore, the electrodes in the chamber are placed into portable furnaces (heated containers) or vacuum packing, this lowering the probability of their moisturizing. Violation of the conditions of electrode storage in the chamber before welding leads to formation of cold cracks in the HAZ metal and porosity in the weld metal [12].

It is established that during performance of welding operations an increase of carbon and oxygen content in the weld metal, and a greater loss of manganese and silicon are observed with increase of the depth.

With pressure rise, an increase of hydrogen content in the welded joint is observed, which is related to pressure impact on the electric arc. This may have an essential influence on the joint resistance to cold crack-



ing in welding steels with a high carbon equivalent and plate metal structures. Mechanical properties of welded joints produced under the hyperbaric conditions with application of coated electrodes, are on the level of base metal strength properties.

*Technology of manual TIG welding* under the hyperbaric conditions is, as a rule, applied during performance of the root weld of cylindrical butt joints, when it is necessary to ensure reverse bead formation. Further groove filling is performed by a coated electrode or mechanized MAG process using solid or flux-cored wires.

It is established that pressure increase leads to an increase of arcing voltage. The latter promotes a greater influence of the magnetic blow on the arc process stability, particularly at the pressure above 0.8 MPa. The arc becomes unstable. In a number of cases the high-frequency component is used for its stabilization. One more path is application of an external magnetic field for controlling the arc [20–22], which is induced by a coil wound around a nonconsumable electrode, to which direct current of approximately 3 A is applied. Use of an external magnetic field allowed TIG welding to be performed at the pressure of 2.1 MPa at the current of 100 A. Further experiments allowed establishing that positive results are achieved also in the variable magnetic field, the parameters of which changed by the specified program.

With pressure increase the depth of base metal penetration increases, while the weld width practically does not change. Experiments conducted by numerous researchers show that in the case of TIG welding application increase of the depth of work performance has an only small influence on the welded joint mechanical properties.

*Technology of solid wire MIG welding* has its advantages compared to coated-electrode welding, namely the high efficiency owing to continuous wire feed into the arcing zone, arc process self-regulation and absence of slag in the reaction zone [23]. Under the hyperbaric conditions this technology is usually used in short-arc welding. The same wires are used as a consumable electrode as in welding in air. In reversed polarity current welding the arc process is destabilized with pressure increase, penetration depth and spatter become greater, and the content of iron, silicon and manganese oxides in the gas phase rises (red fume appears). In straight polarity welding the arc is more stable, thus allowing welding to be performed at greater depths.

*Technology of flux-cored wire MAG welding* has the same advantages as the technologies of gas-shielded underwater welding by solid wires. Addition of stabilizing ingredients and master alloys to the core allows welding to be performed at more than 200 m depth, presence of the slag phase improves weld formation, protects the molten metal from interaction with the environment and provides a higher degree of repeatability of the results. Hydrogen content in the welded joint metal decreases. Application of seamless flux-cored wires, specially developed for welding under the hyperbaric conditions, allows welding to be performed in higher modes. This yields a positive re-

sult compared to coated electrode application, the use of which requires lowering the current with greater depth. Welding performance in higher modes allows eliminating preheating from the technological cycle in a number of cases.

Investigations were conducted to determine the influence of partial pressure of oxygen contained in the composition of the shielding gas mixtures (He/CO<sub>2</sub>, He/O<sub>2</sub>) on oxygen content in the weld metal in welding by flux-cored wires alloyed by manganese and nickel [13]. Investigations were conducted at different partial pressures of oxygen (0.002–0.15 MPa) and carbon gas (0.0015–0.2 MPa) at down to 100 m depth. Welding was performed by a group of welders-divers with different experience of underwater operations. As was anticipated, increase of partial pressure of oxygen in He/CO<sub>2</sub>, He/O<sub>2</sub> mixtures increased oxygen concentration in the weld metal. Investigation of impact toughness of the metal of welds made at the pressure of 0.6–1.0 MPa (testing temperature of –20 °C), showed high values of absorbed impact energy (52–107 J), depending on the used shielding mixture. These values are quite high and meet the standard requirements, envisaged for structures built in the open sea.

For more than 15 years now research has been conducted for development of automated systems allowing shortening the time of the welder-diver staying under the hyperbaric conditions [14–16]. The most often used technology is TIG welding combined with orbital systems tried out at down to 230 m depth. Complexes are being developed, which allow performance of completely automatic welding under the hyperbaric conditions with remote control of all the processes from the sea surface.

The produced oil and natural gas contain a considerable amount of H<sub>2</sub>S and CO<sub>2</sub>, which promote development of corrosion defects in pipelines. In this connection research is currently being conducted on development of the technologies and equipment for welding at great depths of materials of an increased corrosion resistance [24–26]. Such materials include clad steels and duplex stainless steels. Possibility of application of TIG and plasma-arc MIG welding technologies for joining these steels is being verified. Experimental work is now limited to 30 m depth. Welding is performed in the horizontal position.

In practical repair of underwater transitions in ex-USSR dry welding was almost not applied, except for repair of Aleksandrovsk–Anzhero–Sudzhensk oil pipeline in the point of its transition across the Ob river (674 km). The author directly performed this work (part of the information was given in [27]). Both the defects of the pipe of 1020 mm diameter of 18G2AF steel with the wall thickness of 16 mm were located close to each other in the area of navigation path, where the water current speed was 0.7–0.9 m/s. In this connection, the work could only be performed in winter from ice. The work was performed in two stages.

At the first stage in February–March, 1979, a crack in a circumferential weld 250 mm long was welded up in a dry chamber at 6 m depth. After washout of the soil, removal of the lining and hydraulic insulation



a chamber was mounted on the defective pipe section. The chamber was made of part of steel tank of 1800 × 1500 × 2200 mm size. Chamber dimensions did not allow free manipulation of the welding equipment, as the distance from the pipe outer surface to the chamber wall in the lower part was not more than 60 cm. The chamber was put onto the pipeline using side cut-outs, which enclosed the pipelines and were sealed by two flanges. The water was ousted by compressed air fed from the surface by a compressor. Diver going in and out, supplying the necessary tools and devices, cables and hoses was performed through its lower part. The defective area (400 × 650 mm) was cut out using oxy-gas cutting. An abrasive tool was used for edge preparation for welding. A patch with a backing was installed in the formed hole. After its fixation on the pipeline inner surface with application of wet mechanized welding the root weld was made. Then, the groove was filled using coated metal electrodes in an air environment. Pipe preheating was performed before welding. The electrodes were fed into the work zone in a sealed container. Welding was performed in SVU type gear. AVM-1M breathing apparatus was used for breathing, this limiting the duration of the welder staying under the water to 50 min. During a work day the welder usually performed two, seldom three descents. In the dried space the welder-diver stayed in the diving gear and breathing apparatus. Total duration of work performance, including chamber manufacturing, its mounting and performance of underwater welding operations (approximately 35 h), was more than 75 days. Ultrasonic and hydraulic testing of the pipeline showed that the pipe has one more defect.

The second stage of repair work performance was conducted in February–March, 1980. Considering the experience of the previous expedition, the work was organized so that soil wash-out was conducted in the summer-autumn time. In this case pipe cleaning and caisson mounting were conducted in 10 work days. Underwater work was organized so that the welder was able to stay in the caisson for a longer time. ShAP-62 device was used. Air was supplied to the diver from a transportation cylinder. The visible part of the defective section of the field joint was 200 mm. Similar to the first case, the crack was located in 13.00 to 14.30 position. The technology of welding operation performance was the same as in repair of the previous butt. Smaller weight and dimensions of the diver gear, as well as the possibility of working for 3–5 h under the water without going up to the surface, allowed welding operations to be performed in 10 h, allowing for the time of pipe heating and weld dressing.

It is obvious that the technology of welding in a dry chamber, into which both the welder and the welded component fit, will be used in the future for assembly and repair of critical hydraulic facilities, such as high-pressure pipelines, and individual elements of off-shore platforms, as well as low clarity and high speeds of the water current.

An increase of the scope of repair work performance using the technologies of wet welding by coated electrodes with improved welding technological properties and mechanized processes is anticipated. With a

small scope of welding operations electrode application is preferable when achieving the strength properties adequate to those of the mechanized process. The quality of work performance is largely dependent on the level of specialist training. Technological solutions developed and tested in practice allow a fast and efficient repair of the ship hulls and other hydraulic facilities with minimum labour consumption.

1. Paton, B.E., Savich, I.M. (1987) On the 100th anniversary of underwater welding. *Avtomatich. Svarka*, **12**, 1–2.
2. Kononenko, V.Ya., Rybchenkov, A.G. (1994) Experience of wet mechanized welding with self-shielded flux-cored wires in underwater repair of gas- and oil pipelines. *Ibid.*, **9/10**, 29–32.
3. Kononenko, V.Ya., Gritsaj, P.M., Semekin, V.I. (1994) Application of wet mechanized welding in repair of ship hulls. *Ibid.*, **12**, 35–38.
4. Kononenko, V.Ya., Lomakin, N.N. (1996) Application of underwater mechanized welding with self-shielded flux-cored wires in repair of ships and hydraulic facilities. *Ibid.*, **4**, 36–39.
5. Kononenko, V.Ya. (2004) *Technologies of underwater welding and cutting*. Kiev: Ekotekhnologiya.
6. Kononenko, V.Ya. (2006) *Technologies of underwater wet welding and cutting*. Kiev: PWI.
7. Kononenko, V.Ya. (2005) Technology of wet mechanized welding in construction of IRSSP «Prirozlommaya». *The Paton Welding J.*, **9**, 33–35.
8. Evans, N.H. (1974) Welding in offshore constructions. *Metal Construction and British J.*, **5**, 153–157.
9. Coriatt, G. (1980) Hyperbaric welding in the repair of offshore pipelines and structures. *3R International*, **3**, 156–162.
10. Bursaux, G.A., Harrison, J.M. (1979) Hyperbaric welding with dry transfer from a dynamically positioned. In: *Proc. of 11th Ann. Offshore Technol. Conf.* (Houston, 1979), 1537–1544.
11. Delaue, P.T., Weber, J.D. (1979) Hyperbaric underwater welding. The state of the art. Part 1. *Welding J.*, **8**, 17–25.
12. Delaue, P.T., Weber, J.D. (1979) Hyperbaric underwater welding. Part 2. *Ibid.*, **9**, 28–35.
13. Lezzi, F. (2007) Principali problemi nella soldatura subacquea. *Riv. Ital. Saldat.*, **1**.
14. Rougier, R. (1991) Automatic hyperbaric welding with thor-2. In: *Proc. of 10th Int. Offshore Mechanics and Arctic Eng. Conf.*, Vol. III, 159–162.
15. Hutt, G., Pachniuk, L. (1993) Progress in controlled hyperbaric pipeline tie-ins. In: *Proc. of 12th Int. Conf. on Offshore Mechanics and Arctic Eng. A*, Vol. III, 167–174.
16. Berge, J.O., Harbrekke, T., Knagenhjelm, H.O. (1991) Automation in underwater hyperbaric pipeline welding. In: *Proc. of 10th Int. Offshore Mechanics and Arctic Eng. Conf. A*, Vol. III, 163–167.
17. Dick, O., den Ouden, G. (1993) The effect of pressure on the TIG welding process. In: *Proc. of Int. Offshore Conf. of IIW* (Trodheim, 27–28 June, 1993), 155–162.
18. Allume, C.J. (1993) Effect of pressure on arcs. In: *Ibid.*, 171–178.
19. Bailey, N. (1991) Welding under water — a metallurgical appraisal. In: *Proc. of 1st Int. Offshore and Polar Eng. Conf.* (Edinburgh, 11–16 Aug., 1991), 331–338.
20. Richardson, I. (1993) Deflection of a hyperbaric plasma arc in a transverse magnetic field. In: *Proc. of 12th Int. Conf. on Offshore Mechanics and Arctic Eng. A*, Vol. III, 155–166.
21. Hoffmeister, H., Epler, U., Ludwig, J. (1991) Effect of electromagnetic fields on convection and penetration in hyperbaric TIG welding of X6CrNiTi 18 10. In: *Proc. of 10th Int. Offshore Mechanics and Arctic Eng. Conf. A*, Vol. III, 155–158.
22. Suga, Y. (1991) The effect of magnetic field on stabilization of TIG arc welding under hyperbaric helium atmosphere. In: *Proc. of 1st Int. Offshore and Polar Engineering Conf.* (Edinburgh, 11–16 Aug., 1991), 325–330.
23. Drangelates, U., Bouaifi, B., Bartzch, J. (1997) Schutzwasserschweißen fuer die unterwasserfertigung. *Schweissen und Schneiden*, **12**, 909–914.
24. Olsen, J.M., dos Santos, J.F., Richardson, I.M. (1994) Effect of process parameters on metal transfer of hyperbaric GMAW of duplex steels. In: *Proc. of 4th Int. Offshore and Polar Eng. Conf.* (Osaka, 1994), 107–111.
25. Ware, N., dos Santos, J.F., Richardson, I.M. (1994) Effect of shielding gas composition on the properties of hyperbaric GMA welds in duplex steel. In: *Proc. of 13th Int. Offshore Mechanics and Arctic Eng. Conf.*, Vol. III, 369–377.
26. dos Santos, J.F., Richardson, I.M. (1994) Process related aspect of hyperbaric GMAW of duplex steels. In: *Proc. of 4th Int. Conf. on Duplex Stainless Steels* (Glasgow, 13–16 Nov., 1994).
27. Galyuk, V.Kh., Zabela, K.A., Kononenko, V.Ya. et al. (1981) Repair of an oil pipeline using the underwater welding. *Transport i Khranenie Nefti i Nefteproduktov*, **12**, 22–24.



# CALIBRATION OF AN OPTICAL SYSTEM FOR EVALUATION OF TEMPERATURE FIELD DISTRIBUTION IN THE WELDING ZONE

V.A. KOLYADA and E.V. SHAPOVALOV  
E.O. Paton Electric Welding Institute, NASU, Kiev, Ukraine

A procedure is proposed for calibration of an optical system designed for evaluation of temperature field distribution in the welding zone. Calibration allows compensation of all the inherent and setting errors of sensor block components.

*Keywords:* arc welding, automation, temperature field, welding zone, multispectrum pyrometry, video cameras calibration, standard, conjugated points

The use of sensors, recording the process of welded joint formation, is an important and promising direction in the field of arc welding process automation. Measurement of temperature field distribution in the zone of welded joint formation arouses particular interest. Use of the devices securing contactless temperature measuring --- optical pyrometers is the most suitable for solving this task. The pyrometry methods, in comparison with contact methods of temperature measuring, differ by the following advantages:

- fast response that is determined by the type of radiation receiver and schematic of signal processing;
- possibility of measurement of the temperature of dynamic objects and equipment elements live with high-voltage potential;
- possibility of measurement of high temperatures, at which application of measuring contact means either impossible or the time of their work is very short.

A distinction is made between single- and multi-spectrum pyrometers. Single-spectrum pyrometers receive radiation in one spectrum range that can be rather wide. Further on the temperature is determined by the value of measured radiation power. Multispectrum pyrometers that are also known as spectral ratio and color pyrometers, receive radiation in two and more spectrum ranges. The object temperature is determined comparing the radiation power in different ranges.

Application of single-spectrum optical pyrometers for measuring temperature characteristics in the welding zone is not rational, as in this case it is necessary to know a priori the value of radiation coefficient of the object surface. Metal surface, by its nature, can not possess constant radiation coefficient in welding zone. The molten metal surface forms a smooth mirror, the radiation ability of which can be less than 0.1, and radiation ability of the slag, floating on the surface, can reach values of 0.90–0.95. Moreover, single-spectrum pyrometers are subjected to the dust and contaminant impact to considerable degree.

As distinct from single-spectrum pyrometers, multispectrum ones do not depend on the radiation coefficient, and mechanical disturbances in the measuring zone do not practically influence their functioning, that is why they give the best fit for measuring temperature distribution in the weld pool and HAZ. At the same time multispectrum pyrometers represent rather complicated and expensive devices, which cost is commensurable with the price of specialized welding complex. Hence, the necessity of development of more simple and affordable devices designed for evaluation of temperature field distribution in the welding zone.

Chinese scientists [1] suggested the design of a so-called two-color (two-spectrum) sensor, which consists of one video-camera and two light filters with different length of the transmission wave located on a rotating cylinder in front of the lens. Two images, shot through different light filters, are compared in the device controller, and temperatures distribution in welding zone is determined on this basis. Such an optical system, in addition to a complicity of its design and problems connected with synchronizing of video-camera shutter with the cylinder rotation, has one more essential drawback --- delay of the time of cylinder half-turn. Stated working cycle of such a sensor is 0.5 s that essentially limits the sphere of its possible application.

The work on creating an optical system for evaluation of temperature field distribution with application of two color pyrometry, the diagram of which is given in Figure 1, is also carried out at PWI. The sensor block, as to its design, consists of two video cameras, set at an angle of 90° relative to each other, and narrow-band light filters with different transmission wave length, set before objectives. Light-dividing box that divides radiation from the heated object in two flows, one of which passes through the box without changes and the second is refracted at right angles, is located between the video cameras. In such a way video cameras «see» one and the same section of the object through different light filters. The images of the studied object are simultaneously transmitted to the optic system controller, where evaluation of temperature distribution is done on their basis. Working cycle of the system corresponds to the period of frame

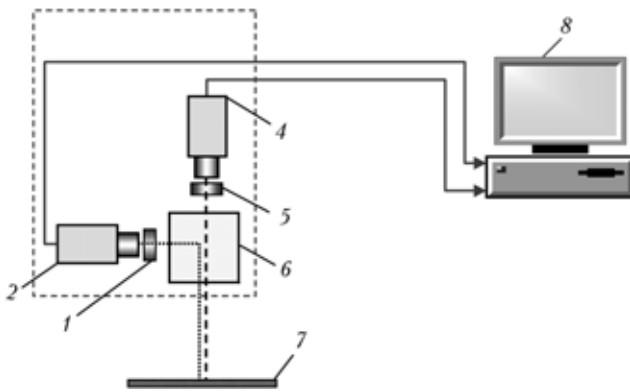


**Figure 1.** System diagram for distribution of temperature field in welding zone: 1, 5 — light filters; 2, 4 — video cameras; 3 — sensor block; 6 — image divider box; 7 — object of measurement; 8 — controller

updating of the standard television signal and is equal to 40 ms.

In an ideal case, it is necessary to compare the points in images with the same coordinates for calculation of temperatures distribution in welding zone. However the coordinates of one and the same section of the measured object in the images can essentially differ in practice. This is connected with the fact that at assembly of the sensor block, minor angular or linear errors of component mounting can arise, which in total leads to an essential error of mutual orientation of video cameras sighting axes. Besides, inner parameters of manufactured products, such as video cameras and lenses, can incompletely meet the certificate data that also leads to essential errors at video signal analysis and treatment. Hence, the necessity for sensor block calibration.

The calibration problem can be divided into the following sub-tasks in the given case:

- formation of a mathematical model, which includes video camera and standard models;
- definition of coordinates of characteristic points on standard images for two video channels;
- searching for parameters of video camera models, at which the deviation between the measured characteristic points of the standards and their models will be minimal;
- matrix formation for point conjugation in images, obtained from two video cameras.

Calibration procedure with utilization of a flat template as a standard is used for determination of the spatial position of video cameras that is considered in greater detail in [2]. Uniform grid with known cell

dimensions is marked on the template surface. The mathematical model of the optical system includes description of the position of video cameras relatively to the standard and conversion from the video camera coordinate systems into the coordinate systems of the respective images. The positions of video cameras relative to the standard coordinate system are determined unambiguously by the matrices of spatial conversions  $\mathbf{A}_{c1}$   $\mathbf{A}_{c2}$  which include rotation angles  $\alpha$ ,  $\beta$ ,  $\gamma$  and linear shifting  $dx$ ,  $dy$ ,  $dz$  of video cameras relative to the point of origin of reference coordinate system that coincides with the central grid point on standard surface. The transition from camera coordinate systems to images is done by perspective view transformation. Thus, if a point position in the reference coordinate system is set by vector  $\mathbf{r}_0$ , then the vectors defining the given point coordinates in the image coordinate systems of the first and the second video cameras  $\mathbf{r}_{i1}$ ,  $\mathbf{r}_{i2}$  can be found from the following relationships

$$\mathbf{r}_{i1} = \mathbf{P} [\mathbf{r}_0 \mathbf{A}_{c1}^{-1}] \text{ and } \mathbf{r}_{i2} = \mathbf{P} [\mathbf{r}_0 \mathbf{A}_{c2}^{-1}],$$

where  $\mathbf{P}$  is the function of perspective view transformation. Inverse transformations are also true.

Grid node points are used as characteristic points on the standard image. Procedures of image identification on digital images described in study [3], are used for automatic determination of node points of coordinates. The result of node point localizing on images, obtained from sensor block video cameras, is shown in Figure 2. The images of the standard grid have different orientation because of inherent and setting errors of sensor block components.

Interactive measurement of the parameters of video camera models up to finding minimal mean-root-square deviations between measured node points and node points of modeled grid is done for determination of the video camera parameters, at which graphic models of the grid correspond to the actual images of the standard grid. At the initial stage the change of angular and linear parameters is performed with a considerable step. If the mean-root-square deviation over two successive iterations does not change, then the step decreases. The interactive process is finished, if the change of the step does not lead to decrease of mean-root-square deviation. The results of grid model superposition onto the measured points and the corresponding numerical results of calibration for each video camera are shown in Figure 3.

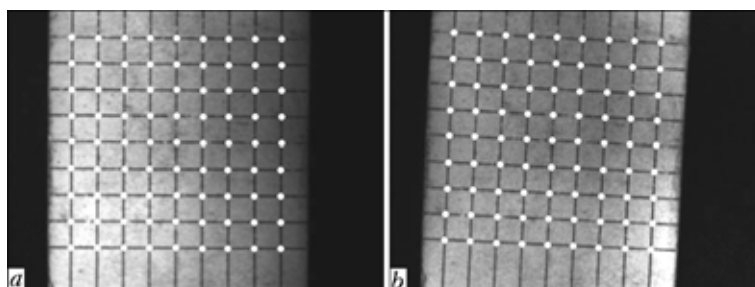


**Figure 2.** Result of finding grid points in two images (a and b)

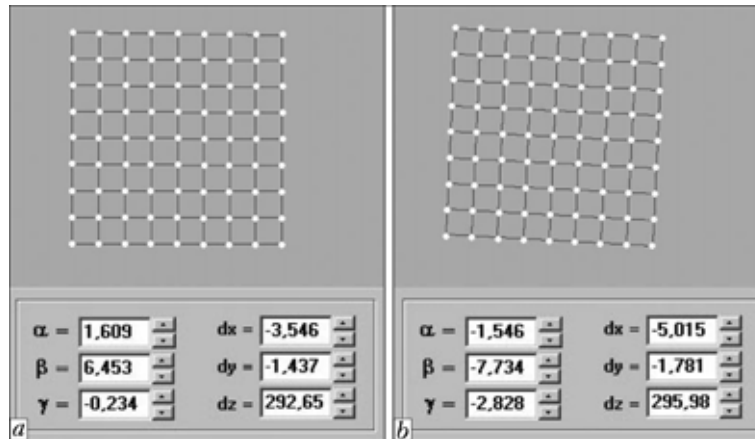


Figure 3. Results of video camera calibration 2, 4 (a and b)

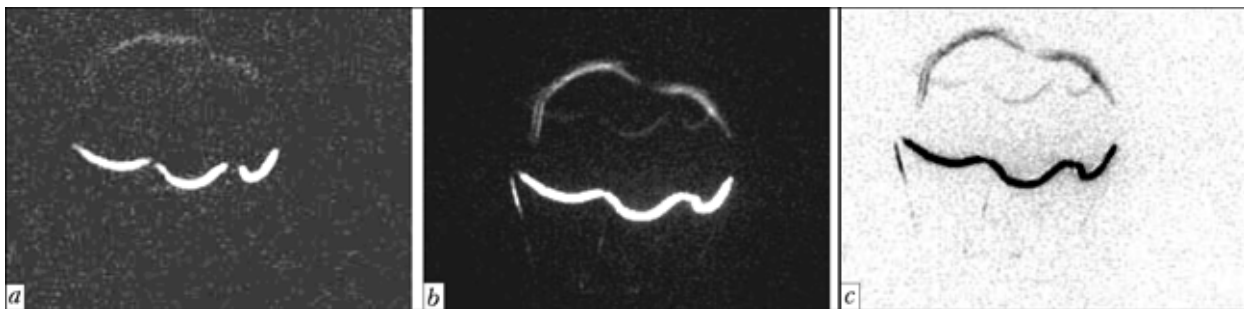


Figure 4. Visual evaluation of calibration: a, b --- initial images; c --- inverted superposition

With the help of matrix  $\mathbf{A}_{c1}$  and inverse perspective transformation for any point on the first image, it is possible to calculate its shift relative to the datum point of the optical system. At the same time with the help of matrix  $\mathbf{A}_{c1}^{-1}$  and direct perspective transformation it is easy to find the position of the point in the second image, which corresponds to the point on the surface of the standard with earlier found shifts. In such a way it is possible to find for each point in the first image the conjugated point in the second image.

The mechanism of semi-transparent image superposition is used for visual evaluation of correctness of the results of sensor block calibration. The corresponding conjugated points from the second image are placed over the points from the first image. Two initial images of the filament lamp and an inverted result of superposition, using the conjugated points, are shown in Figure 4. The initial images of the filament lamp have different orientation, but a practically complete coincidence of fragments is observed at their superposition. In addition to visual evaluation, it is also possible to numerically calculate and compare the coordinates of conjugated points in the reference system of coordinates. At numerical analysis the deviations between the coordinates of the conjugated points do not exceed  $\pm 1$  pixel.

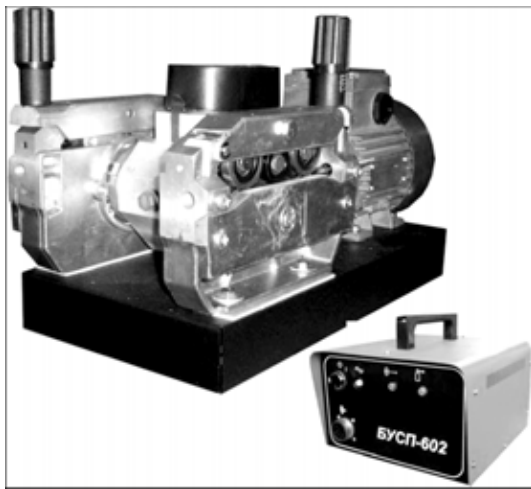
A matrix of point conjugation is formed, if a positive result is obtained during checking of the sensor block calibration results. Matrix indexes correspond to point coordinates in the image from the first video camera. Each matrix element contains two integer values that are the conjugated point coordinates in the image of the second video camera. Further on this matrix is used when comparing images of the objects, obtained with the help of two video cameras of the video block.

Evaluation of the temperature field distribution in welding zone, using one video camera and a rotating disk with light filters, in general case is reasonable, as image points with similar coordinates are compared. However, video filming of the two images, by which the temperature field evaluation is performed, is done at different moments of time and in different points, which at considerable welding speeds leads to essential measurement errors. Developed calibration procedure, where two video cameras are used and welding zone images obtained practically simultaneously are compared, gives a higher quality evaluation of temperature distribution in real time.

1. Zhang, H., Pan, J. (1999) Real-time measurement of welding temperature field and closed loop control of penetration. *China Welding*, 8(2), 127–134.
2. Kiselevsky, F.N., Kolyada, V.A. (2005) Calibration of triangular optical sensors. *The Paton Welding J.*, 5, 48–49.
3. For, A. (1989) *Perception et reconnaissance d'images*. Ed. by G.P. Katys. Moscow: Mashinostroenie.



## NEWS

**«SELMA» COMPANY OFFERS****WIRE FEED MECHANISM OF THE MP-602-2 TYPE (TWIN-WIRE)  
FOR MECHANISED SURFACING AND WELDING**

Wire feed mechanism MP-602-2 is designed for mechanised DC gas-shielded twin-wire surfacing and welding in a set with power units for automatic welding.

The electrode wire feed speed is adjusted by replacing gears. It is fitted with a power and control unit operating at a mains voltage of  $3 \times 380$  V.

MP-602-2 is intended for long-time operation under severe industrial conditions at increased welding and surfacing parameters.

**Specifications**

Engine supply voltage, V .....	$3 \times 36$
Rated welding current, A .....	600
Quantity of rollers (at each wire), pcs .....	4
Diameter of electrode wire, mm	
steel .....	1.2–2.0
flux-cored .....	1.2–3.2
Adjustment of wire feed speed .....	stepwise
Quantity of wire feed speed adjustment steps .....	30
Electrode wire feed speed, m/h .....	104–980
Power of wire feed drive engine, W .....	180
Weight of MP-602-2, kg .....	26
Weight of control unit, kg .....	5.5
Dimensions of MP-602-2 (length $\times$ width $\times$ height), mm .....	$550 \times 350 \times 340$
Dimensions of control unit, mm .....	$315 \times 250 \times 230$

**ARC WELDING SIMULATOR**

Arc welding simulator DTS-02 is designed for training and initial education of electric welders in methods of tungsten-electrode argon-arc welding (TIG mode) with contact ignition of the arc.

The simulator provides acquirement of practical skills in ignition and maintenance of a certain length

of the arc gap, maintenance of spatial position of the hand tool (torch) simulating device relative to the surface of a piece being welded, and maintenance of thermal parameters of the weld pool (welding speed).

The simulator allows simulation of the welding process by using a low-amperage welding arc; entering of initial parameters of the welding process (length of the arc gap, heat input, and electrode inclination angle) into the personal computer; PC fixation of the information on a training session by length of the arc gap, electrode inclination angle and heat input (welding speed); formation of the acoustic feedback signals when parameters being monitored exceed their boundary values; changing of complexity of the training tasks by individual parameters; statistical processing and evaluation of the results of a training session; and documentation of the training results in the form of tabular and graphical data on a paper carrier.

The simulator is controlled by PC of a class not lower than «Pentium» with the Windows 9x, ME, NT or XP operating system, and is connected via a serial port (RS-232 COM1–COM4).





## EXPLOSION TREATMENT OF TANK STRUCTURES

Residual tensile stresses act as an energy basis for corrosion cracking of metals in alkalis. The presence of these stresses causes cracking of the welds, leading to formation of substantial leaks and a serious hazard of major accidents. Relieving of residual stresses in large-size metal structures by heat treatment is a labour-consuming, expensive and low-efficiency technology. The E.O. Paton Electric Welding Institute developed the technology for relieving residual stresses by explosion treatment, which was successfully applied in construction of new alumina plants and expansion of production of the existing ones in the former Soviet Union, Ukraine and Yugoslavia.

Substantial increase of production capacities by the world leading producers of aluminium generates the need to commercially apply this technology.

In 2007, Joint Stock Company «RUSAL» completed construction of 15 decomposers and 2 mixers at the Nikolaev Alumina Plant by using the explosion treatment technology to relieve residual stresses in the welds. Diameter of the above devices was 12 and 14 m, respectively, and their height varied from 15 to 34 m, thickness of the metal welded (steel St3sp (killed)) ranging from 8 to 40 mm.

The work on explosion treatment was performed by specialists of the Research-Engineering Centre «Explosion Treatment of Metals» of the E.O. Paton Electric Welding Institute. Successful interaction with erection organisations allowed the explosion

treatment technology to be naturally integrated into the schedule of construction of tanks, and the work to be completed without any delay of assembly-welding operations.



Peculiarity of explosion treatment is that the technology is realised by using overlaid explosive charges, which are placed on the internal surface of a tank along the welds. Walls of the tank serve for protection from the harmful effect of an explosion. Depending upon the conditions of explosion operations and thickness of the metal treated, from 20 to 180 running metres of the welds can be treated per detonation.

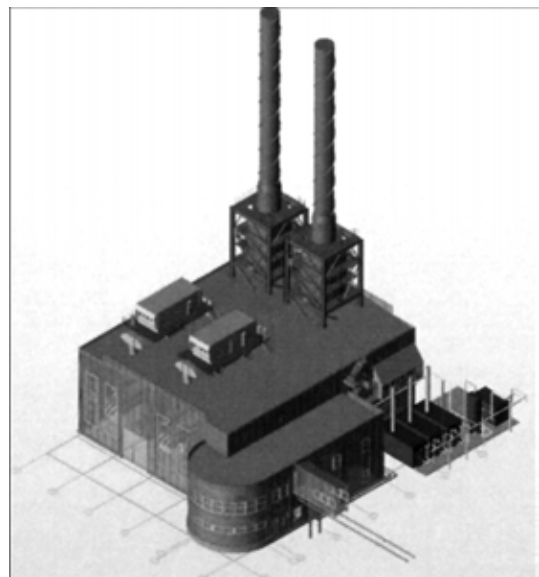
Advantages of explosion treatment include also the absence of the necessity to use special equipment and power supplies.

## SYSTEM FOR DISPOSAL OF DOMESTIC WASTES

The E.O. Paton Electric Welding Institute, Closed Joint Stock Company «Pilot Plant for Welding Equipment of the E.O. Paton Electric Welding Institute» and Institute of Gas «Teplotekhnologiya» Ltd. developed design of the system for disposal of domestic wastes by the high-temperature pyrolysis technology using the energy potential of the process.

The high-quality and ingenious equipment combined with the environmentally clean incineration technology allows the production to be placed within the precincts of a city, which reduces the costs for transportation of wastes. The high-temperature complete incineration system provides emission of the flue gases with a decreased content of harmful substances, in compliance with the existing standards. This improves the ecological situation in a region. Pollution sources are eliminated, and loads on the environment are decreased.

The flow diagram of the system is as follows: wastes are loaded into a bin with a feed conveyer,



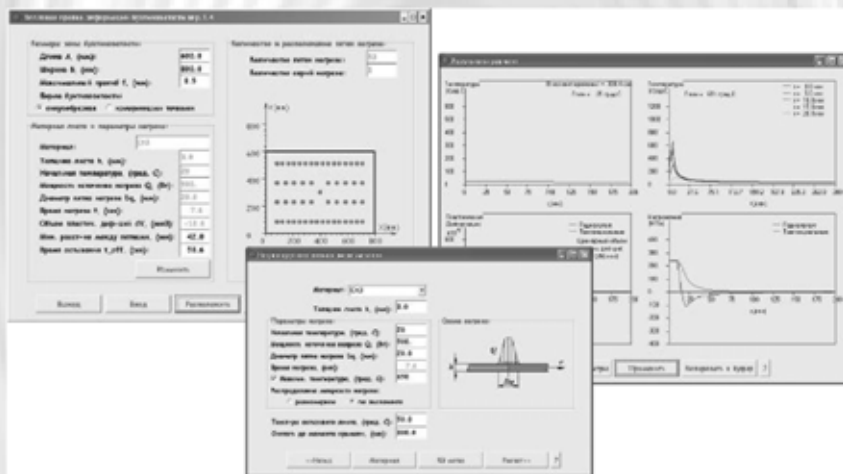


which feeds the wastes to the sorting conveyer, where the wastes are sorted to extract valuable components for their further processing and utilisation, after which the raw stock is fed to the dump conveyer and loaded into the loading bin. The raw stock is fed in portions by using a feeder to the multifunctional burner, where it is burnt to generate a substantial amount of heat. Gases with a temperature of 1200–1600 °C, formed as a result of combustion of a fuel, wash water-wall pipes of the steam boiler, and then the steam drum. After emission from the boiler, the gases still have a sufficiently high temperature (350–450 °C). Water economiser is installed to use energy of these gases. To ensure good burning of the fuel, the air fed to the firebox is heated in the air heater, and then pumped with a fan into the burner and firebox. Upon passing through the ash collector, recuperator, dry sorption cleaning reactors and ceramic filter, the flue gases are

sucked off by the smoke sucker, which emits them into the flue funnel. The formed steam in water-wall pipes of the steam boiler is fed to the steam drum, and then from the latter to the steam turbine, where the electric current generator is installed on the same shaft with the turbine. The generated electric power is fed to the transformer, where the electric current voltage is thus increased. And then the electric current is supplied to the distribution device, which comprises composite shields, to which all the generated electric power is supplied. Upon completing the work in the turbine, the steam is fed to the condenser, from which the condensate is directed by a pump via the regeneration heater to the deaerator (feed water storage tank). To condensate the steam, water from a water supply line (river, lake, or pond) is fed to the condenser, and the circulation pump is used to feed the water.

## COMPUTER PROGRAM «THERMAL STRAIGHTENING OF BUCKLING DISTORTIONS»

Software «Thermal Straightening of Buckling Distortions» allows determination of parameters of a round heat spot for a definite material and thickness of metal sheet, optimum from the point of view of producing maximum residual plastic shrinkage deformations and prevention of a local buckling of the sheet during heating. The software allows also in-process estimation and arrangement of necessary amounts of such heat spots at the area of buckling zone depending on definite sizes of the zone and value of deformation. The software has been developed to automate the process of thermal straightening of thin-sheet structures with buckling distortions and contains appropriate interface for input of data by sizes of the zone and value of deformation with an automatic system of measurement. To control the process of a manual shock-free thermal straightening, the program envisages the feasibility of a quick input of data to preset the length and width of a rectangular zone of buckling distortion and value of maximum buckling in the zone center. Software gives the opportunity of selection of interface support and reference in two languages (Russian, English).



**Purpose.** Control of process of manual or automatic thermal straightening of buckling deformations of thin-sheet structures.

**Application.** Manufacture of welded thin-sheet structures in ship-, railway car building and other branches.

Cost of license for a permanent use of the program is 4900 UAH.

Contacts: Prof. Lobanov L.M.  
E-mail: office@paton.kiev.ua

## COATED METALLIC ELECTRODES FOR MANUAL ARC WELDING OF CORROSION-RESISTANT STEELS

Coated metallic electrodes of ANV-72 grade are designed for manual arc welding of products from corrosion-resistant steels of 08Kh18N10, 12Kh18N10T, 10Kh17N13M3T grades and their analogues. Electrodes allow welding performance in all spatial positions at direct and alternating ( $U_{o-c} > 65$  V) current, that is important in repair-restoration works. Electrodes possess good welding-technological properties, provide high technological strength, resistance to intercrystalline corrosion, good weld metal formation, stable burning of arc. In this case the following mechanical properties are attained:  $\sigma_t > 550$  MPa,  $\sigma_{0.2} > 290$  MPa,  $\delta > 30$  %,  $\dot{a}_n > 100$  J/cm<sup>2</sup>.

**Purpose and application.** Electrodes ANV-72 are designed for welding products of steels of 12Kh18N10T, 10Kh17N13M3T types and used in chemical industry.

**Status and level of development.** Experimental-industrial batches of electrodes are manufactured, technical conditions are specified.

**Proposals for co-operation.** Signing of contract, agreement for delivery of electrodes of this grade.

**Main developers and performers:** Prof. Yushchenko K.A., Dr. Kakhovsky Yu.N., Dr. Bulat A.V., Group Head Samojlenko V.I.

## COATED METALLIC ELECTRODES FOR MANUAL ARC WELDING OF CORROSION-RESISTANT STEELS

Coated metallic electrodes of ANV-29 grade are designed for manual arc welding of products from corrosion-resistant steels of 08Kh18N10, 08Kh18N10T, 12Kh18N10T grades and their analogues. Electrodes possess good welding-technological properties, provide high technological strength, a good weld metal formation, stable burning of arc, easy removal of slag crust, negligible spattering and easy repeated ignition of arc. In this case the following mechanical properties are attained:  $\sigma_t > 550$  MPa,  $\sigma_{0.2} > 250$  MPa,  $\delta > 30$  %,  $\dot{a}_n > 100$  J/cm<sup>2</sup>.

**Purpose and application.** Electrodes ANV-29 are designed for welding products of steel 08Kh18N10T, 12Kh18N10T and similar grades in food, chemical industry, fuel-power complex and others.

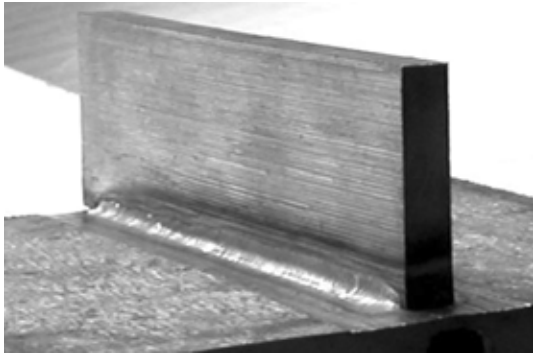
**Status and level of development.** Industrial batches of electrodes are manufactured, technical specifications are specified.

**Proposals for co-operation.** Signing of contract, agreement for delivery of electrodes of this grade.

**Main developers and performers:** Prof. Yushchenko K.A., Dr. Kakhovsky Yu.N., Group Head Samojlenko V.I.

## COATED METALLIC ELECTRODES FOR MANUAL ARC WELDING OF COMBINED JOINTS OF AUSTENITIC STEELS WITH PEARLITIC STEELS

Coated metallic electrodes of ANV-66 grade are designed for manual arc welding of products of manganese steels in all spatial positions at direct and alternating ( $U_{o-c} > 65$  V) current, that is important in repair-restoration works. Electrodes provide high technological strength, a good weld formation, stable arc burning, and also the following mechanical properties:  $\sigma_t > 550$  MPa,  $\sigma_{0.2} > 250$  MPa,  $\delta > 30$  %,  $\dot{a}_n > 90$  J/cm<sup>2</sup>.



**Purpose and application.** Electrodes ANV-66 are designed for welding products of manganese steels of 110G13L type used in mining, chemical industry, machine building and railway transport.

**Status and level of development.** Experimental-industrial batches of electrodes are manufactured, technical specifications are specified.

**Proposals for co-operation.** Signing of contract, agreements for delivery of electrodes of this grade.

**Main developers and performers:** Prof. Yushchenko K.A., Dr. Kakhovsky Yu.N., Group Head Samojlenko V.I.

## AEROSOL ACTIVATING FLUXES FOR TIG WELDING OF STEELS AND ALLOYS

The activating fluxes (activators) have been developed for TIG welding (arc welding with tungsten electrode in inert gases) of different steels, nickel and titanium alloys for one pass without edge preparation and filler wire. The specifics of this process of TIG welding over the layer of activator (so-called A-TIG) consists in a preliminary deposition of the activator of a required composition on edges of butt being welded (in welding) or defective weld area (in remedy/ repair of defects of type of non-fusion, pores, cracks, etc.) with a subsequent performance of conventional TIG welding. The presence of activator in the zone of arc and welding pool allows increasing significantly the penetrability of arc, depth of penetration with a simultaneous decrease in weld width.

Application of activators for A-TIG welding as compared with conventional TIG welding makes it possible to:

- 2–3 times increase the penetration depth up to 12–15 mm for one pass without edge preparation and application of filler wire;
- suppress or eliminate the effect on weld formation (depth of penetration and width of weld) of steel grade of different purity of melting (in variation of chemical composition content of one of residual elements);
- decrease distortions in welding;
- 2–7 times increase the welding efficiency depending on thicknesses being welded;
- 2–5 times decrease the cost of welding works by reducing the expenses for electric power, welding consumables (shielding gas, wire), elimination of operation for metal removal and reduction in time of welding.

A-TIG welds do not differ both from conventional TIG welds and also from parent metal by a complex of properties and service characteristics.

**Purpose.** The main purpose of aerosol activators is the improvement of penetrability of arc, efficiency and effectiveness of TIG welding of structures of steels, nickel and titanium alloys of medium thicknesses from 4 up to 25 mm (Figure).

**Application.** They are used for sheet and hull structures, vessels and containers, pipes, tube sheets in chemical, petrochemical industry, power engineering for nuclear and heat electric stations, for aerospace engineering, in shipbuilding, reinforcement manufacturing, etc.



TIG:  $I_w = 100$  A,  $v_w = 12$  m/h; A-TIG:  $I_w = 50$  A,  $v_w = 12$  m/h

**Status and level of development.** Industrial production of aerosol activators has been mastered.

**Proposals for co-operation.** Delivery of aerosol activators, carrying out research works and development of new types of activators and technologies of A-TIG welding of new materials, joints and structures.

**Main developers and performers:** Prof. Yushchenko K.A., Res. Ass. Kovalenko D.V.

## **DOCUMENTATION ON WELDING, HEAT TREATMENT AND QUALITY CONTROL OF WELDED JOINTS, TECHNOLOGICAL EQUIPMENT OF HEAT ELECTRIC STATIONS, HEATING BOILER ROOMS, HEATING AND DISTRIBUTION SYSTEMS**

Enterprises of heat power engineering refer to the category of objects of an increased hazard. Almost all the heat-engineering equipment of heat electric stations, heating units, heating boiler rooms, heating and distribution systems, the most part of auxiliary equipment should meet the requirements of State standard documents, guaranteeing the safe conditions of service of power units. These standard documents include DNAOP 0.00-1.11-88, DNAOP 0.00-1.08-94, DNAOP 0.00-1.07-94, DNAOP 0.00-1.20-98, GID 34.03.101-96, RD 34 15.027-89, a number of SniPs, GOSTs, OSTs, DSTU, etc. Volumes and complexity of welding jobs in manufacture, erection and repair of technological equipment of heat- and power units are rather wide. This is stipulated by a large assortment of used steels, billets, parts, units, complexity of works to be fulfilled (spatial position of butts being welded), need in guarantee of high quality of welding and validity of quality control of welded joints, application of several types of welding, preheating and heat treatment of welded joints.

The E.O. Paton Electric Welding Institute in collaboration with OJSC «Energomontazhproekt» and JSC «Kievenergo» has developed the system of technological instructions with technological charts (29 descriptions) and process charts (3 descriptions) for preparation for welding, assembly, heat treatment and quality control of welded joints of definite assemblies of power units operating at temperature up to 450 and 575 °C: steam pipings, pipelines, pipes of heating surfaces, collectors, economizers, drums, boilers, etc. A number of instructions refers to the repair of definite units of power blocks.

**Purpose and application.** The developed instructions and process charts are designed to increase the quality of works being fulfilled in manufacture, assembly and repair of technological equipment of heat- and power blocks of heat electric stations, factory power blocks, heating boiler rooms, heating and distribution systems, to provide an appropriate level of service reliability of the equipment.

**Status and level of development.** Instructions and charts have been developed at the level of requirements of State standard documents in heat power engineering, subjected to expertise, coordinated with bodies of Gosnadzorokhrantrud of Ukraine and transferred to a number of heat electric stations.

**Proposals for co-operation.** Instruction can be transferred to Customers by agreement.

**Main developers and performers:** Prof. Yushchenko K.A., Dr. Chekotilo L.V., Dr. Tsaryuk A.K., Eng. Ivanenko V.D.

Prof. Yushchenko K.A.  
E-mail: office@paton.kiev.ua

## SUBSCRIPTION FOR «THE PATON WELDING JOURNAL»

If You are interested in making subscription directly via Editorial Board, fill, please, the coupon and send application by fax or e-mail.

The cost of annual subscription via Editorial Board is \$324.

Telephones and faxes of Editorial Board of «The Paton Welding Journal»:

Tel.: (38044) 287 6302, 271 2403, 529 2623

Fax: (38044) 528 3484, 528 0486, 529 2623.

«The Paton Welding Journal» can be also subscribed worldwide from catalogues of subscription agency EBSO.

<b>SUBSCRIPTION COUPON</b>			
Address for journal delivery	_____		
Term of subscription since	200	till	200
Name, initials	_____		
Affiliation	_____		
Position	_____		
Tel., Fax, E-mail	_____		



## ADVERTISEMENT IN «THE PATON WELDING JOURNAL»

### External cover, fully-colored:

First page of cover (190×190 mm) – \$500  
 Second page of cover (200×290 mm) – \$350  
 Third page of cover (200×290 mm) – \$350  
 Fourth page of cover (200×290 mm) – \$400

### Internal cover, fully-colored:

First page of cover (200×290 mm) – \$350  
 Second page of cover (200×290 mm) – \$350  
 Third page of cover (200×290 mm) – \$350  
 Fourth page of cover (200×290 mm) – \$350

### Internal insert:

Fully-colored (200×290 mm) – \$300  
 Fully-colored (double page A3) (400×290 mm) – \$500  
 Fully-colored (200×145 mm) – \$150  
 Black-and-white (170×250 mm) – \$80  
 Black-and-white (170×125 mm) – \$50  
 Black-and-white (80×80 mm) – \$15

- Article in the form of advertising is 50 % of the cost of advertising area
- When the sum of advertising contracts exceeds \$1000, a flexible system of discounts is envisaged

### Technical requirement for the advertising materials:

- Size of journal after cutting is 200×290 mm
- In advertising layouts, the texts, logotypes and other elements should be located 5 mm from the module edge to prevent the loss of a part of information

### All files in format IBM PC:

- Corell Draw, version up to 10.0
- Adobe Photoshop, version up to 7.0
- Quark, version up to 5.0
- Representations in format TIFF, color model CMYK, resolution 300 dpi
- Files should be added with a printed copy (makeups in WORD for are not accepted)